Development & Evaluation of Multiple Optical Trapping of Colloidal Particles Using Computer Generated Structured Light Fields

A thesis submitted in fulfilment of the requirements for the degree of Master of Applied Science

Jason L. Walsh
B. App.Sci (App. Physics) (Hons)

School of Applied Sciences
College of Science, Engineering and Health
RMIT University
August 2009

Declaration

I certify that except where due acknowledgement has been made, the work is that of the author alone; the work has not been submitted previously, in whole or in part, to qualify for any other academic award; the content of the thesis is the result of work which has been carried out since the official commencement date of the approved research program; any editorial work, paid or unpaid, carried out by a third party is acknowledged; and, ethics procedures and guidelines have been followed.

Jason L. Walsh

/ /2009

Acknowledgements

Firstly I would like to thank my family (especially my parents) and friends for their continued support over the years, despite the constant "*when are you going to finish?"* questions, I don't think I would have made it without their support. Now I am going to make you all read this thesis so you know what I was up to these past years.

Special thanks go to Emily, Hailey, Steve, Keith and Kristina for the numerous Vault and Order sessions. I have now discovered the joys of coffee and overpriced scotch. It was great to chat with people from the other side of the 'street' (i.e. chemistry).

Mr Joe Harland for allowing me to take first year and service Physics labs. They were a great counter to project work and I thoroughly enjoyed my experiences. Thankyou to Mr Nick Besley for allowing me to take part in and, eventually run the Science Peer Tutor program at RMIT. I met a lot of great people as a result and the experiences have inspired me to become a physics teacher. To all my colleagues, (especially Ben and Vincent) who have shared the office with me, thanks for all the discussions. Thanks must go to Lachlan Hennessy for his assistance last year as part of his final year project.

Special thanks to Assoc. Prof Gale Spring for assisting me with the photographic component of this project. His help and assistance was greatly appreciated as was his enthusiasm for the project.

Thank you must go to my second supervisor; Assoc. Prof Gary Bryant for all his help, insightful comments and assistance concerning the colloidal aspects of this project. At one stage it looked like I wouldn't need him but thankfully, I did.

Finally, I reserve for greatest praise for my supervisor; Assoc. Prof Phil Wilksch for his untiring dedication to this project and for his comments and suggestions concerning this thesis. He was always available for consultation and assistance when I needed him so a huge 'Thank you!' must go to him.

Table of Contents:

List of Figures:

List of Tables

List of Movies

List of Acronyms

CGH: Computer Generated Hologram

DFT: Discrete Fourier Transform

DOE: Diffractive Optical Element

FFT: Fast Fourier Transform

HCP: Hexagonal Close Packed

HOE: Holographic Optical Element

HOT: Holographic Optical Trapping

IFT: Iterative Fourier Transform

LCD: Liquid Crystal Display

NA: Numerical Aperture

PMMA: Poly(methyl)methacrylate macroparticles

SLM: Spatial Light Modulator

SLR: Single Lens Reflex

Summary

Colloidal particles are small particles ranging in size from nanometres to micrometres suspended in a fluid. Amongst many scientific and biological applications, they have been used to model crystallisation, vitrification, and particle interactions. One of the main areas of interest has been the use of colloidal model systems for the study of the fundamental nature of the fluid-crystal and fluid-glass phase transitions**.** It has been shown that colloidal particles can be trapped and manipulated using strongly-focused light beams known as optical tweezers, and this has paved the way for research into the area of micromanipulation using optical trapping. Holographic elements can replace multiple lenses in creating large numbers of optical tweezers and this is known as holographic optical trapping (HOT). A computer generated hologram can be designed to create large structured light fields, consisting of multiple foci, to enable trapping of multiple particles in arbitrary configurations.

The overall aim of this project was to design, develop and test the suitability of a simple, inexpensive optical trapping arrangement suitable for multiple optical trapping using a theoretically accurate coding scheme for the creation of the holographic diffraction pattern, and photographic film for hologram reproduction. To achieve this, a theoretically-exact expression for the wavefront of a single point source was implemented in the coding scheme, allowing for the fast creation of multiple point sources suitable for holographic optical trapping experiments. Compensation for the spherical aberration present in the focusing optics was implemented into the coding scheme.

Kodalith photographic film was chosen as the holographic recording medium for its high contrast and availability. The film has proven to be a successful medium, when used to record photographically-reduced images of high-quality printouts of the computed diffraction pattern, as it was able to successfully reproduce complex light fields. It is believed that this will be the first time that this film has been implemented for optical trapping purposes. The main limitations concerning the performance of the holograms recorded on Kodalith were the phase nonuniformities caused by unevenness in the film thickness which resulted in a failure to separately resolve light traps separated by less than about 5 μm. Index matching of the film between sheets of flat glass helped to compensate for these limitations.

Holographic optical trapping was successfully observed using a variety of different initial beam powers, holographic aperture settings and light field configurations. Trapping experiments on of two types of particles (PMMA and polystyrene) were successfully conducted, with as little as ~150 μW per trap being required for multiple polystyrene trapping. However, particles were weakly trapped and were easily dislodged at these powers, and a higher power per trap of around 1 mW is preferred. The use of a relatively low numerical aperture (NA) 50 mm SLR lens for focusing the holographic optical traps was successful, proving that optical trapping can be conducted without the use of high NA microscope-objective lenses commonly used in other set ups.

Holographic trapping of colloidal particles was successfully conducted at RMIT University for the first time proving the validity of the coding scheme, the recording method and the trapping arrangement. Further progress in colloidal trapping research will largely depend on improvements in the quality of the holographic recording medium.

1) Introduction

Colloids are small microscopic particles suspended in a fluid. These particles can range in size from nanometres to micrometres. Such particles are widely used in research as models for studying fundamental physics processes, such as crystallisation, vitrification, hydrodynamics and particle interactions.

The study of colloids has many useful applications, such as the study and creation of photonic crystals [1, 2], as well as biological applications and creating new materials to name but a few. However, one of the main areas of interest has been the use of colloidal model systems for the study of the fundamental nature of the fluid-crystal and fluid-glass phase transitions. The use of light allows for the interaction with, and manipulation of colloidal particles without damaging them, allowing for ever more subtle experimental investigations into both fundamental and applied problems. Using strongly-focused light, these particles can be manipulated into crystal structures. This process is often referred to as optical trapping and the focused light referred to as optical tweezers. Trapping the particles allows for measurements of individual particle response to forces acting on a particle due to applied fields (electrical, shear) or the direct interactions with neighbouring particles. These, as well as applications in biology, have made this a very active field of research [3-5].

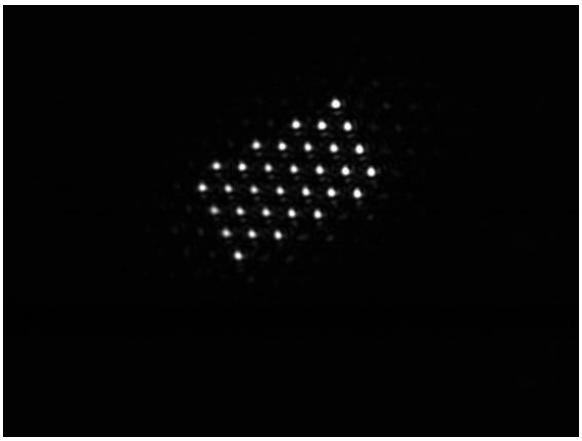

(**Fig. 1** Holographic structured light field consisting of 32 point sources)

1) Introduction

A computer generated transmission hologram can be designed to diffract a single laser beam into a large number of individually focused points of light arranged in a crystal configuration, which will then act as a multiple optical trap when focused on a colloidal suspension. Holographic optical trapping (HOT) is an exciting and emerging field in the area of colloidal research [6, 7], as it has the ability to generate multiple tweezers in a variety of configurations. A holographic structured light field consisting of multiple traps in a crystal configuration is shown in Fig. 1.

While creation of large, two-dimensional structured light fields for colloidal trapping along with some three-dimensional trapping has previously been undertaken [5], the systems are limited by their relatively small trapping volume, and also the corresponding set-ups are quite complex and expensive which restricts their widespread use. The aim of this work was to investigate some alternative approaches to the calculation, fabrication and implementation of computer generated holograms for colloidal trapping applications.

Calculation

Most of the coding schemes currently being used make use of either Fraunhofer or Fresnel approximations which are not a theoretically-exact model of the diffraction integral. Also many of these schemes are optimized for phase-only devices such as spatial light modulators (SLMs) and performance can suffer from the lack of resolution in these devices.

A theoretically-exact point source coding method was trialled in calculating the diffraction patterns of the structured light fields. As the coding scheme incorporates the exact diffraction integral it should theoretically give better performance for near-field diffraction compared to Fourier-based methods. The simplicity and flexibility of this method allowed for the calculation of large numbers of point sources in arbitrary configurations. To ease the demands on the resolution of the hologram; the trapping arrangement made use of a 50 mm SLR camera lens to focus the hologram; to which compensation for the spherical aberration present in this lens was incorporated into the coding scheme.

1) Introduction

Fabrication

As a substitute to recording the holographic diffraction patterns via diffractive optical elements or spatial light modulators, high contrast photographic film (Kodalith) was trialled instead as it is inexpensive, readily available and the development process is well known. To achieve the required resolution, computer generated patterns were printed out in a large scale and then photographically-reduced to the required size.

Implementation

A trapping set-up has been developed which is rather simple, compact and inexpensive in comparison to other arrangements but still suitable for trapping experiments. The proposed arrangement has the advantage of not requiring a sophisticated set-up as it makes use of off-the-shelf optical components. Other methods commonly use SLMs connected to a computer as the diffractive element, with a combination of telescopic and large-aperture microscope objective lenses. One of the main innovations in this work is the substitution of the high NA microscope objective with a standard 50 mm SLR camera lens, which has the benefit of greater working distance. It was beneficial to investigate the amount of laser power located in the structured light fields by investigating power loss throughout the trapping arrangement and also by direct estimation of power in each trap using a digital camera. This lead to determination of the order of magnitude of the minimum amount of power per trap required to trap particles.

In summary, the overall aim of this project was to design, develop and test the suitability of a simple, inexpensive optical trapping arrangement suitable for multiple optical trapping using a theoretically-exact coding scheme and photographic film for hologram reproduction.

2) Holography

2.1) Overview of Holography

Holography is a technique for recording and viewing a three-dimensional image with true depth of field and perfect parallax. The study of holography can trace its origins back to 1948 when Denis Gabor proposed a method of removing aberrations from electron microscope images. This method was further adapted to presenting three-dimensional images of objects. The technique of holography records the pattern of interference between the light reflected or transmitted from an object, and a reference beam. The object beam is then reconstructed by diffraction when a copy of the original reference wave is passed through the hologram. The advent of the laser as a coherent light source resulted in increased interest in holography. The two main types of optical holograms are transmission and reflection holograms. In a typical transmission hologram setup, a laser beam is split up into two components and expanded and one of the beams is used to illuminate a desired object, which is placed *in front* of a suitable recording medium (e.g. holographic plate). The portion of the beam reflected off the object then illuminates the recording medium. The other beam, a reference beam, also illuminates the recording medium directly. During exposure, the interference pattern caused by these two beams is recorded. This type of hologram is referred to a transmission hologram because when it is viewed, the reilluminating beam passes through the hologram and the diffracted beam passes out the far side. The image can be viewed from the far side, looking back into the hologram. Figure 2.1 shows a typical optical transmission hologram recording and viewing configuration showing both primary and conjugate image formation.

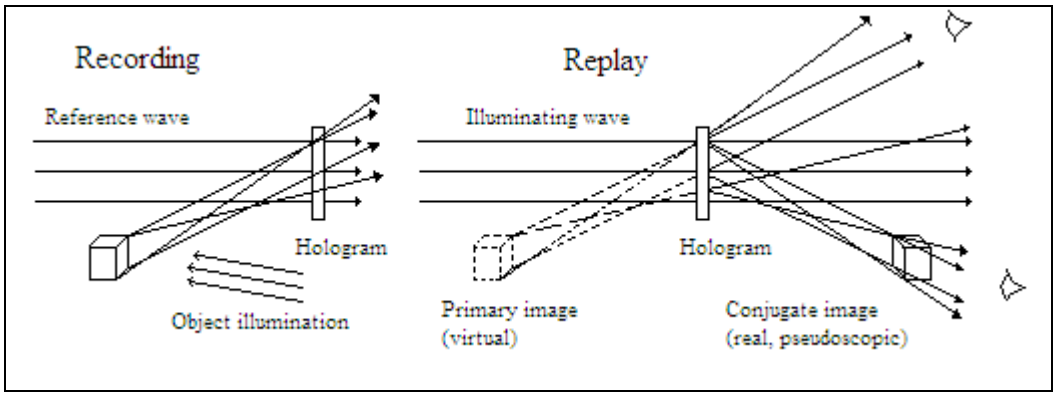

(**Fig. 2.1** Transmission hologram recording and replay configuration)

Reflection holograms employ a similar setup for recording except the object is placed on the opposite side of the recording medium to the reference beam. During reconstruction, the image can be viewed from the same side as the illuminating source. In addition, they can be viewed using white light sources (such as incandescent lamps) which make them more suitable for display purposes. Figure 2.2 demonstrates a typical reflection hologram recording and viewing configuration.

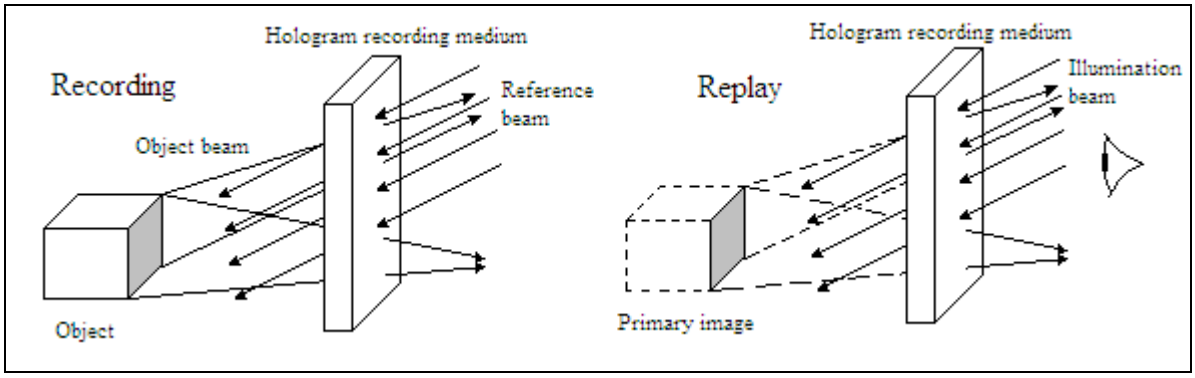

(Fig. 2.2 Reflection hologram recording and replay configuration)

There are many different types of optical holograms that can be created and a full treatment on the subject of optical holography can be found in a book by Hariharan [8].

The interference pattern produced at the holographic plane can be derived mathematically by using appropriate diffraction theories. The total diffraction pattern on the holographic plane, which is often called the complex amplitude, can be calculated by a computer. Computer generated holograms (CGHs) allow the construction of holographic images that do not physically exist and thus have numerous applications, modelling being one of them. The two main types of diffraction considered are Fraunhofer and Fresnel diffraction. To represent a true 3D image, Fresnel (or 'near-field') diffraction must be used; however, if the object is assumed to be far away from the holographic plane (i.e., at infinity) then the calculations can be simplified to Fraunhofer (Fourier or 'far-field') diffraction. The resultant image will only be two-dimensional. The diffraction pattern at a particular point on the holographic plane is made up of contributions from every point from the object and thus, for large objects, calculations can become extensive. The development of faster computers along with the research into the development of diffractive optical elements (DOEs) has significantly aided in the construction and widespread availability of computer generated holograms for

commercial and research purposes. The next sections will go into more detail concerning holographic diffraction theory.

2.2 Diffraction Theory

The diffraction pattern at a point ***P*** on the holographic plane is made up of contributions from every point ***p*** located in the object plane, described by the Huygens–Fresnel Principle. The object plane is divided up into many small elementary areas *da*, each of which gives rise to a point source. In Fig. 2.3, each point in the object plane gives rise to a spherical wavelet:

$$CA(x,y)K(\theta)\frac{1}{R}\exp[i(kR-\omega t)]da \qquad \textbf{Eq.2.1}$$

where R is the distance from ***p*** to ***P***, *k* is the wave number, *K(θ)* is the inclination factor which is equal to $\frac{1}{2}(1+\cos\theta)$, θ is the angle of the secondary spherical wavelets relative to the direction of the primary wavefront, and *A(x,y)* describes the complex amplitude and phase of the electric field at **p**. *C* is a constant equal to 1/iλ, where $i=\sqrt{-1}$, and ω*t* describes the phase of the wavelet with angular frequency ω an time *t*..

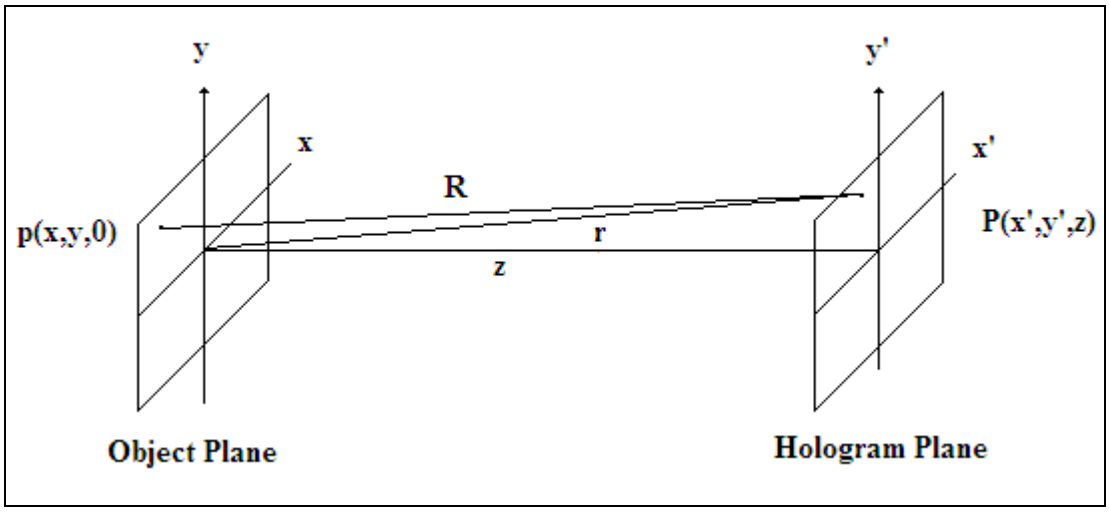

(**Fig. 2.3** Hologram geometry)

The total field arriving at point ***P****(x', y', z)* in the hologram plane is found by adding up the contributions from points ***p****(x, y)* in the object plane, assuming the spherical wavelets are coherent and all polarised in the same direction. This gives rise to the Kirchoff Diffraction Integral which is given by:

$$E_h(x',y') = \frac{1}{i\lambda}\exp(-i\omega t)\iint \frac{A(x,y)K(\theta)\exp(ikR)}{R}dxdy \qquad \textbf{Eq.2.2}$$

The factor $exp^{-i\omega t}$ can be set to 1 since the field will be calculated at an instantaneous time. The Diffraction Integral can now be written as:

$$E_h(x',y') = \frac{1}{i\lambda}\iint A(x,y)\frac{1}{R}\exp(ikR)K(\theta)dxdy \qquad \textbf{Eq.2.3}$$

If the distance between the object and hologram plane is z, then R is:

$$R = \sqrt{(x'-x)^2 + (y'-y)^2 + z^2} \qquad \textbf{Eq.2.4}$$

A change in R of only a fraction of a wavelength will make a big change to the factor exp^{ikR}. When the distance z between the object and hologram plane is small, the diffraction pattern varies radically for small changes in z. When z is large, the diffraction pattern tends to have a stable distribution and will only spread out in size when z is increased. These results give rise to two types of diffraction; Fraunhofer (far-field) and Fresnel (near-field).

The Diffraction Integral is usually unwieldy and approximations can be made. If the dimensions x, x', y, y' are small compared to z, then rays emitted from the object will be within a small solid angle of the optical axis. Thus, the inclination factor $K(\theta)$ can be set to 1. Since $R \approx z$, therefore, $1/R = 1/z$. However this approximation is too coarse for the exponential function, so the approximation is taken further by expanding R (Eq. 2.4) in a power series, giving:

$$R \approx z - \frac{(x'x + y'y)}{z} + \frac{(x'^2 + y'^2)}{2z} + \frac{(x^2 + y^2)}{2z} \qquad \textbf{Eq.2.5}$$

These approximations lead to the Fresnel Approximation:

$$E_h(x',y') = \frac{\exp(ikz)}{i\lambda z}\exp[\frac{i\pi}{\lambda z}(x'^2 + y'^2)]\iint A(x,y)\exp\left[\frac{i\pi(x^2+y^2)}{\lambda z}\right]\exp\left[\frac{-2i\pi(x'x+y'y)}{\lambda z}\right]dxdy$$

Eq.2.6

The electric field in the hologram plane, where z = constant, is given by a Fourier transform of the complex amplitude $A(x, y)$ of the object plane after multiplication with a quadratic phase factor, then multiplied with a phase curvature factor.

If the object is located at large z, then the approximation $1/r \approx 1/R \approx 1/z$ can be made provided x, x', y and y' are all $<< r$. If the Fraunhofer Condition is met:

$$\lambda r >> x^2;\ \lambda r >> y^2$$

then the quadratic phase factor, $\exp\left[\frac{i\pi(x^2 + y^2)}{\lambda z}\right]$, can be set ≈ 1.

Also, in the Fraunhofer case, R can be expanded around r in a Taylor series expansion and the second order terms neglected giving:

$$R \approx r - \frac{(x'x + y'y)}{r} \qquad \textbf{Eq.2.7}$$

Thus, the phase curvature factor is dropped from the integral, giving the Fraunhofer approximation:

$$E_h(x', y') = \frac{\exp(ikR)}{i\lambda R}\iint A(x, y)\exp\left[\frac{-2i\pi(x'x + y'y)}{\lambda z}\right]dxdy \qquad \textbf{Eq.2.8}$$

This can be interpreted as a spherical wave multiplied by the Fourier transform of the complex amplitude $A(x, y)$.

To obtain a hologram, every E_h point must be calculated, and then added with a suitable reference beam. The magnitude of the resultant is squared to get the power density of the hologram. This power density is the diffraction pattern of the hologram. The above equations for Fresnel and Fraunhofer diffraction can be evaluated by breaking the object into a series of planes along the z-axis. Therefore, to represent a 3D object, changes in z will have to be made. Thus, a 3D hologram will be a collection of 2D intensity distributions in different z planes. If the planes are tilted, then the inclination factor $K(\theta)$ can't be ignored and the relationship between r, R and z will change. Several papers have been published that investigate the calculation of diffraction patterns for Fraunhofer diffraction [9-12] and Fresnel diffraction [9, 13-15]. The construction of holograms of large objects using Fresnel

diffraction has been investigated, either by introducing an alternative co-ordinate system [16] or by the elimination of vertical parallax to lessen memory requirements and calculation time [17].

The 2D Fast Fourier Transform (FFT) algorithm is the most widely used algorithm for creating computer generated holograms of the Fourier and Fresnel type. The FFT is an efficient algorithm for computing the discrete Fourier Transform (DFT) of an array of discrete samples of a function. If an object plane consists of $M \times N$ pixels with j planes in the z-direction, then there will be $j \times M \times N$ data elements, with each element requiring its own memory address. Thus the memory requirements and calculation time can become quite large when creating 3D holograms. The FFT algorithm makes no distinction as to whether a pixel in the object plane contains part of the object or not as far as memory storage is concerned. The FFT generates a transform array which is the same size as the object array. The difference between the FFT and a true Fourier transform is that the 2D FFT performs a double summation over an array of samples of the object function while the 2D Fourier transform performs a double integral over a continuous function. See Brigham [1974] for a full treatment on the Fast Fourier Transform. FFTs form an integral part of coding schemes such as Iterative FFTs [18], and the Gerchberg-Saxon algorithm [19] which is used to generate phase-only holograms, also known as *kinoforms*. These types of algorithms are used widely in the field of Holographic Optical Trapping. Figure 2.3 shows a reconstruction from a phase CGH implemented with a 2D FFT, composed of triangular objects focused at different depths [20]. The bottom triangle is in focus. The hologram was originally coded as an amplitude type and recorded using holographic film. After developing, the film was placed in a bleach bath which has the effect of converting the hologram into a phase type.

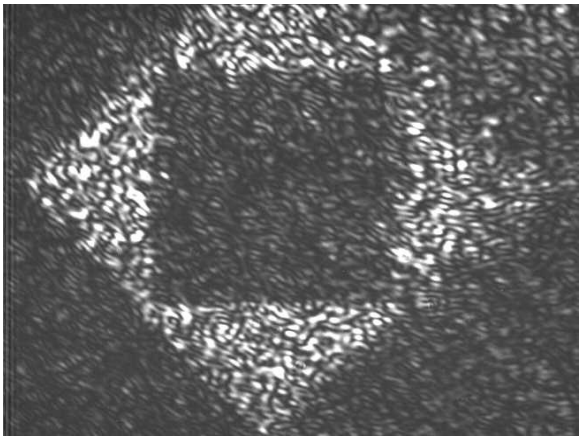

(**Fig. 2.4** Image reconstructed from FFT based amplitude CGH of triangular objects at different focal depths.)

2.2.1 Amplitude Vs Phase Holograms

Holograms can be classified as either amplitude or phase, depending on the value of the amplitude transmission coefficient τ, which is the complex factor by which light passing through the hologram medium is multiplied. In the case of optical holography, τ is determined by, and ideally proportional to, the power density during exposure. If τ is a real number, there is no phase variation in the recorded medium and the hologram modifies only the amplitude of light passing through it by partially absorbing some of it. An example of this is recording using silver halide emulsion which is then developed and fixed using normal methods. Unfortunately, the efficiency of amplitude holograms is quite low (<10%).

On the other hand, if τ is complex, the phase of the reilluminating beam is also affected and not just its amplitude. A faithful holographic image is still reconstructed provided that τ is linearly proportional to the power density at the recording stage. If the magnitude of τ is close to 1, very little light is absorbed, thus phase holograms tend to be more efficient. The medium on which the hologram is recorded needs to be relatively thick, as phase variations across the medium are needed to produce a phase change in the holographic image. An example of this is silver halide film bleaching, in which the bleach converts the silver grains into silver salts (conventional bleaching) or removes them (reversal bleaching). In both cases, refractive index modulation results.

The *kinoform* [21] is a hologram made with a phase-only coding method where the object can be reconstructed using a hologram with only phase variations. First, the computer calculates

the discrete Fourier transform of the object. The phases of the complex samples of the Fourier transform are determined and the amplitude of the transform is set to 1. Thus the complex transmittance of the cell is only determined by the phase. To simplify recording, multiples of 2π are subtracted from the computed phase so that the phase only varies from 0 to 2π over the entire hologram. In some cases, especially when using spatial light modulators, the phase variation is between 0 and π. The advantage with kinoforms is that they can theoretically diffract the entire incident light into the final image. Care has to be taken when creating kinoforms as any error in the recorded phase shifts can result in light being directed to the zero order (direct beam) spot, thus spoiling the image.

One of the earliest computer generated holograms was the binary-amplitude type [22]. In this type of hologram, the amplitude transmittance is set to 0 or 1 simulating an amplitude hologram with severe clipping. The method still produces a good holographic image but higher-order 'ghost' images are present as well. A better approximation of an amplitude hologram can be produced with the use of grey levels, 256 being a common number of levels. Also, grey levels can be approximated using a half-tone technique similar to that which is used in newspaper pictures. Another coding scheme commonly used is the point orientated coding method in which the complex amplitude at each point of the object is assumed to be known. While the 2D FFT and associated Fresnel transforms are certainly useful in constructing CGHs, other methods can be used, such as recurrence formulas using ray tracing methods [23].

Also, direct coding of point source objects using the diffraction integral (Eq. 2.2) is possible, and is useful in generating large light fields comprised of individual point sources. The complex amplitudes due to each point source are calculated and then added together. A phase factor simulating a well corrected spherical lens may be applied to focus the sources at a desired distance. The resultant complex distribution gives rise to an amplitude hologram. This coding method will be implemented in this thesis.

2.3 CGH Production & Applications

There are many different types of output devices that can be used to make holograms, the most simple and inexpensive being a printer, either ink jet or laser. Photo-reduction involves photographing the diffraction patterns using a camera with holographic film set at a specific distance to achieve the desired image reduction. A small reduction will result in a large hologram area, but with poor angular diffracting power, while a large reduction results in a small hologram area, but with good diffracting power (refer to Appendix A for theory concerning size vs. resolution). The holographic film is then developed and thus, the hologram can be viewed. To improve the efficiency of the hologram, film bleaching can be implemented which effectively transforms the hologram from an amplitude type to a phase type. The image reconstruction is the same as for optical reconstruction, illuminating the holographic film using a laser with the same wavelength as used in the calculations.

The first computer generated holograms used drum plotters to print out the diffraction patterns which were then photo-reduced in a similar fashion to the method described above. Now, drum and laser-scanning devices, which immediately create exposure patterns on photosensitive materials, are used to create holograms with large space bandwidth products, and structural detail on the order of the wavelength used for reconstruction. The introduction of Spatial Light Modulators (SLMs) [24], along with faster computers have allowed for the generation of dynamic holograms with near real time capabilities. New techniques favour electron beam lithography and ion exchange techniques to fabricate the holograms due to the higher resolution offered by these techniques [25]. However, when dealing with dimensions approaching the wavelength of light, the approximations made in the coding schemes become unacceptable. Therefore, new coding schemes will have to be developed for the micron and sub-micron scale [26].

The uses of computer generated holograms are numerous and include optical data storage, optical data processing, image processing, and interferometry, creation of optical filters, imaging displays, mapping, and diffraction gratings for scattering and security devices. Recent advances in digital holography can be found in books by Poon [2007] and Schnars & Jueptner [2005]. The creation of 3D holograms for modelling purposes would significantly help industries such as the auto and aerospace industries. Progress has been made using CGHs

for head up displays for aircraft and creating virtual machine controls where it is advantageous for workers not to touch the controls. One of the biggest application areas is the creation of holographic optical elements (HOEs), which can be used to simulate devices such as lenses and filters in interferometry, wavefront synthesis, wave polarisation, diffraction pattern sampling, Fresnel region CGH and volume holograms. Another area of interest is in optical computing, with applications in data processing, memory allocation and security devices. While somewhat dated now, the review articles by Lee [27], Tricoles [28], Bryngdahl and Wyrowski [26] as well as more recent works [29] contain detailed sections on the development and applications of computer generated holograms.

CGHs can enable the generation of arbitrary patterns of light, for instance, large numbers of focused points of light arranged in a large structured light field. It is this ability which has made CGHs an attractive alternative in the field of optical trapping.

3) Optical Trapping

The idea that light can exert a mechanical force on an object is not a new one. It is well known in astrophysics that radiation pressure can have a significant influence on matter. However, it wasn't until the early 1970's that studies into the effects of optical forces on microscopic particles began in earnest. Ashkin and co-workers [30] showed that particles could be manipulated by a mildly-focused Gaussian beam. They observed that small latex spheres would be drawn to the region of greatest intensity (i.e. along the beam axis) and would be propelled forward in the direction of the light propagation. With the addition of a second beam propagating in the opposite direction, it was reasoned that the sphere would remain in stable equilibrium (i.e. 'trapped') in a stable optical well. These experiments led to the development of optical levitation traps [31-33] in which the scattering force acting on a particle balanced with gravity, thus trapping the particle. Most of the early studies concentrated on trapping in the Rayleigh regime, where the diameter of the particle is quite small ($<< \lambda$ of incident light), and were focused on atomic trapping and atomic cooling [34-37]. In the Rayleigh regime, neutral particles act as a simple dipole. The forces acting on the dipole can be separated into a gradient force, which is the component acting in the direction of the intensity gradient, and the scattering force acting in the direction of the light propagation. These studies lead to the development of the single beam optical trap [38] in which a collimated beam was tightly-focused using a high numerical aperture lens. It was discovered that particles could be trapped at the focal point of the lens thus eliminating the need for multiple laser and optical levitation traps mentioned previously. Another important discovery was that macroscopic particles were also successfully trapped thus opening up the range of particle sizes available for trapping by this method. Further developments in the field of atomic trapping and cooling lead to the award of the Nobel prize for physics in 1997 [39] as well as investigations into Bose-Einstein condensates [40].

The other regime associated with optical trapping is the Mie regime where particle sizes are quite large ($>>\lambda$) compared to the wavelength of light. The trapping forces acting on a sphere in the Mie regime can be described via a ray optics approach [41-46]. As the colloidal spheres studied in this thesis were between 2–10 μm in diameter, a ray-optics approach will be used to describe the nature of trapping.

3.1) Optical trapping – Theory

Trapping arises from forces resulting from the momentum exchange caused by radiation pressure due to streams of photons interacting with a particle. Figure 3.1 shows a representation of Ashkin's original experiment [30] of a high-index particle located off axis in a mildly-focused Gaussian beam surrounded by a low-index solution. Consider two rays; A and B striking the sphere symmetrically about its centre. Both will undergo refraction in accordance with Snell's Law. The change in momentum experienced by the refracted ray will result in a force opposite to the direction of the change in momentum of the ray. For ray A, which is stronger, the resultant force F_a will be acting in the direction of the beam axis and propagation. The force F_a can be resolved into two components; the gradient force ($F_{gradient}$) and the scattering force ($F_{scatter}$) mentioned in the previous section. There will also be a force associated with ray B labelled F_b. This force will still have a scattering component in the direction of propagation but it will have weaker gradient component acting in the opposite direction to $F_{gradient}$ of ray A. Thus, the overall net force acting on the sphere is in the direction of highest intensity. Not shown in Fig. 3.1 are the reflection forces present at medium boundaries. These forces are quite weak compared to the larger refraction forces and the radial components tend to cancel each other although the axial components do contribute to the overall scattering force [30].

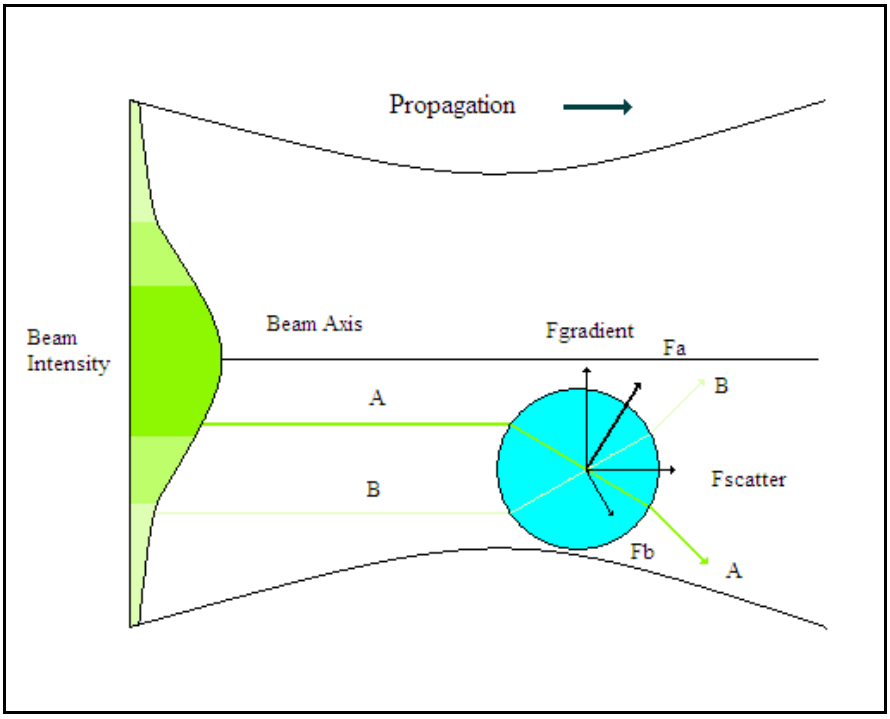

(**Fig. 3.1** Particle in a mildly- focused Gaussian beam showing the origins of $F_{gradient}$ and $F_{scatter}$.)

3.1.1) Single Beam Trap

Figure 3.2 shows the three main forces acting on a sphere in a single beam optical trap (also referred to as an 'optical tweezer'). Light is passed through a high numerical aperture lens and is focused at a specific distance [38]. For simplicity, the sphere is considered to be centred on the z axis and the two rays A and B are of equal intensity. The two rays A and B converging from either side of the objective lens undergo refraction when passing through the sphere. Again, the resultant change in momentum produces forces F_a and F_b with components (i) acting in a downwards direction if the sphere is above the trap focus or (ii) acting in an upwards direction if the sphere is below the trap focus. The overall net force on the sphere is labelled F_{net}. Again F_a and F_b can be broken up into two contributing forces; $F_{gradient}$ and $F_{scatter}$. $F_{scatter}$ acts in the direction of the original beam so can be thought of as a 'downward' force. Reflections at the solution/sphere boundary also contribute to $F_{scatter}$. $F_{gradient}$ is perpendicular to $F_{scatter}$ and this force needs to be dominant for trapping to occur otherwise the scattering force will push the sphere out of the trap. A simple description of the trapping forces acting on a sphere can be found in [42]. The equilibrium position for stable trapping will be when the beam focus is located slightly above the centre of the sphere, where the backwards gradient force balances out the scattering force. Also the equilibrium position is affected by Stokes forces which are viscous drag forces of the surrounding medium. If these drag forces are greater in magnitude than the trapping force, then the particle will be swept out of the trap.

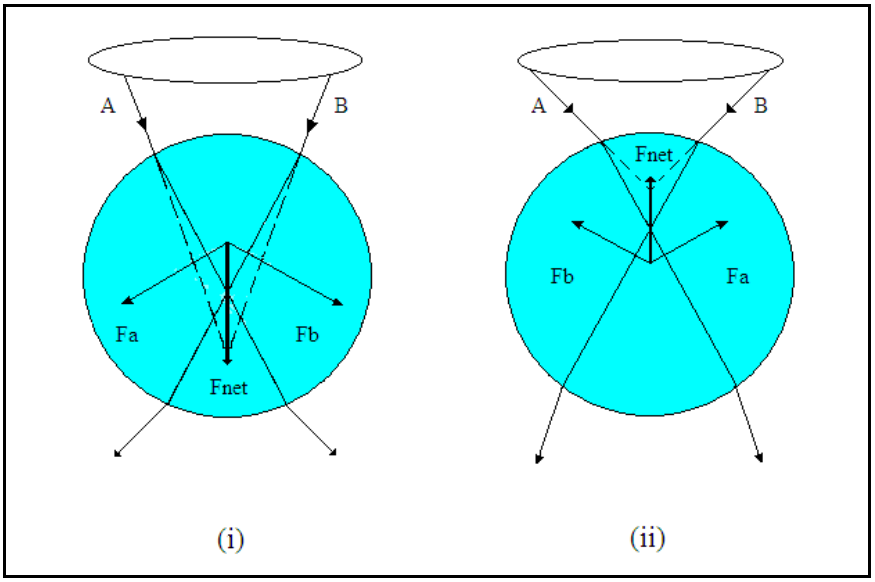

(**Fig. 3.2** Forces acting on a particle trapped in an optical tweezer; i) particle below beam focus and, ii) particle above beam focus.)

The force of a single ray striking a dielectric sphere at an angle of incidence θ is given by Eq. 3.1

$$F = Q\frac{n_s P}{c} \qquad \textbf{Eq.3.1}$$

where $\frac{n_s P}{c}$ is the incident momentum per second of a ray of power P in a medium of refractive index n_s and Q is a dimensionless factor relating to the quality of the trap [41]. Looking at these forces in greater detail, it is found that the total force acting on a sphere is given by the sum of contributions from the reflected ray and the multitude of refracted rays. Again, the total force can be broken up into a scattering/axial component (acting along the z axis) and a gradient/radial component (acting along the y axis) which are given by Eq. 3.2 & 3.3.

$$F_z = F_{scatter} = \frac{n_s P}{c}\left\{1 + R\cos 2\theta - \frac{T^2\left[\cos(2\theta - 2r) + R\cos 2\theta\right]}{1 + R^2 + 2R\cos 2r}\right\} \qquad \textbf{Eq.3.2}$$

$$F_y = F_{gradient} = \frac{n_s P}{c}\left\{R\sin 2\theta - \frac{T^2\left[\sin(2\theta - 2r) + R\sin 2\theta\right]}{1 + R^2 + 2R\cos 2r}\right\} \qquad \textbf{Eq.3.3}$$

The R and T values refer to the Fresnel reflection and transmission coefficients and θ and r refer to the angle of incidence and refraction respectively. The terms in the brackets in Eq. 3.1 & 3.2 can be labelled $Q_{scatter}$ and $Q_{gradient}$ respectively. Since the magnitude of the total force can be considered a vector addition of $F_{gradient}$ and $F_{scatter}$, it can be represented as:

$$F_{total} = \left(F_{gradient}^2 + F_{scatter}^2\right)^{1/2} \qquad \textbf{Eq.3.4}$$

and likewise for Q;

$$Q_{total} = \left(Q_{gradient}^2 + Q_{scatter}^2\right)^{1/2} \qquad \textbf{Eq.3.5}$$

For $F_{gradient}$ to be dominant, a large beam convergent angle is needed as $F_{gradient}$ is dominant at these large angles. Studies [41, 43] showed that incident angles of ≈ 70° produce optimum traps. This corresponds to a high numerical aperture lens (NA ≈ 1.25 in water). Trapping can be achieved via lenses with smaller numerical apertures; however when the convergent angle is 30° or less, $F_{scatter}$ becomes dominant. One of the disadvantages of using a high NA oil-

based objective is the small working distance associated with these lenses (typically in the order of ~0.1mm [45]). Therefore the axial trapping depth is quite limited. Lower NA and water-based objectives can increase the effective working distance of the system but at the cost of lower trapping efficiency due to the smaller angular convergence. The effective refractive index of the system $n = \frac{n_p}{n_s}$ (where n_p is the refractive index of the particle and n_s is the refractive index of the surrounding medium/solution) is also an important consideration when designing traps. For effective trapping, n should be between 1.05 and 1.5. The above equations assume a circularly polarised input beam, however improvements in trapping efficiency can be made if using radially polarised beams [43]. The forces associated with these traps are quite small, ranging in magnitude between 10^{-10}-10^{-12} newton, depending on the power of the trap. The required trapping power is quite small, ranging from hundreds of microwatts to a few milliwatts, depending on particle size, effective refractive index and beam convergence.

The ray optics approach described above gives quite valid results when using a relative particle size $\beta = \frac{2\pi a}{\lambda} \geq 20$ where a is the radius of the particle and λ is the wavelength of light [44]. If this is not the case, then the generalised Lorenz-Mie theory should be used [44, 45, 47, 48], especially for particles in the 0.5–5 μm range, as it takes into account diffraction effects and can be used to predict the forces acting on a medium sized particle with greater accuracy.

Single beam optical tweezers have continued to be employed in various studies of colloidal particles [45, 49], such as investigating trapping of carbon nanotubes [50], constructing 2D optical lattices [51], investigating mesoscopic orbitals [52], force measurements between particles [53], trapping red blood cells [54], trapping of aerosols with super continuum laser sources [55], hydrodynamic interactions between particles [56, 57] and multiple trapping of particles using single tweezers [58]. Recently, multiple traps have been generated by the diffraction pattern of a beam passing through a wire mesh grid [59] and by a modified self imaging effect [60]. Single beam traps are useful for studies on isolated particles; however

the development of Holographic Optical Tweezers (HOTs) has enabled the study of complex colloidal systems.

3.2 Holographic Optical Trapping

Holography is particularly suited to the field of optical trapping as it allows for the creation of multiple, independent optical tweezers in various 2D and 3D configurations [5] thus allowing trapping of multiple particles. A hologram can be specifically designed (either through a CGH or DOE) to alter the wavefront of a single beam into multiple beams thus eliminating the need for multiple beam sources. The use of CGHs to generate optical tweezers is not new. In 1994 He *et al* [61] demonstrated single particle trapping using computer generated holographic doughnut beams, while DOEs have been implemented in generating arrays of optical traps [62-65] for various colloidal studies. These methods generate phase-type Fourier holograms via binarisation or tiling techniques using various forms of the FFT. Figure 3.3 taken from [63] shows a typical optical trapping arrangement which incorporates a DOE. The input laser beam is typically expanded and collimated before passing through or reflecting from a DOE (or SLM). The overall beam containing the zero-order and diffracted beams is then reduced via a series of lenses to fill the back aperture of a microscope objective, which brings the diffracted beams to focus at the desired points in the sample well. The trapping events are recorded using devices such as CCD and CMOS cameras. The use of dichroic mirrors enhances the imaging of trapping events as it blocks out reflections and ‘ghost’ traps connected with the trapping laser, leaving light from an illumination source. Modifying the initial input beam into a converging beam can allow for the suppression of the zero-order bright spot as well as pushing unwanted higher orders out of the sample plane [66].

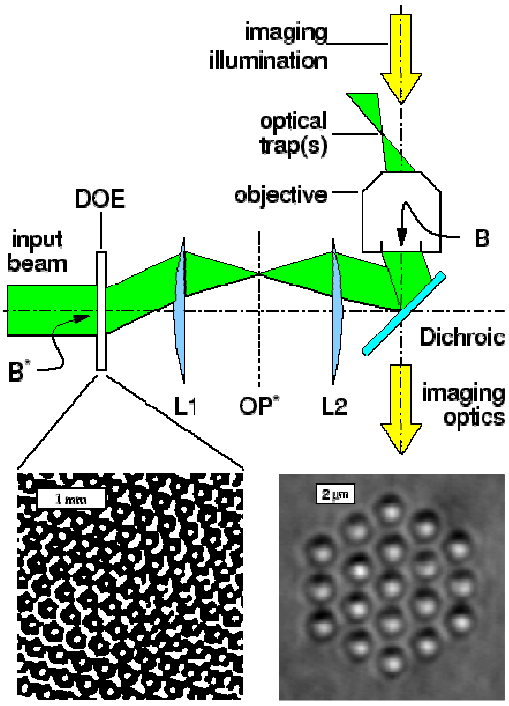

Figure 3.3: Schematic representation of a typical holographic optical tweezer array. A collimated laser beam incident from the left is shaped by a DOE, transferred to an objective lens' back aperture (B) by lenses L1 and L2 and focused into a trapping array. OP^* denotes the plane conjugate to the trapping plane. The point B^* is conjugate to B. The phase pattern on the lower left (black regions shift the phase by π radians) produced the traps shown in the lower right filled with 1 µm diameter silica spheres suspended in water. www.physics.nyu.edu/grierlab/cgh2b/img12.png[63]

The introduction of liquid crystal displays (LCDs) as spatial light modulators (SLMs) [6, 67-71] in transmission and reflection modes has greatly expanded trapping capabilities, enabling the generation of multiple, reconfigurable traps in 2D and 3D. Also, due to the high refresh rates associated with SLMs, dynamic optical trapping can be achieved via the continuous updating of holographic interference patterns. Different algorithms for phase holograms have been implemented using SLMs to generate more efficient traps, these being based on the Gerchberg-Saxton algorithm [6, 72, 73], the adaptive-additive algorithm [6, 63] and other optimisation techniques [6, 66, 73, 74] which have enabled detailed studies on colloidal systems [75-78].

The common HOT systems (with SLMs or DOEs) are quite complex and expensive which has limited their widespread use. Most of the current setups make use of high NA microscope-objective lenses which limits the sample volume available to trapping. In this project, it is proposed to substitute this lens with a 50 mm camera lens which will increase the

volume available for trapping, although at the expense of trapping efficiency as the numerical aperture of this lens is quite low (≈ 0.33), but it is hoped that that the optical power available will still be sufficient for trapping. What is proposed is to create computer generated holograms using a point source method [20] that will generate amplitude holograms of three-dimensional structured light fields with a large number of trapping locations and making use of an inexpensive, easy to build trapping arrangement.

4) Experimental Methods

In principle, a single hologram could be used to convert a collimated laser beam into an array of tightly-focused spots. This would need to achieve large angles of diffraction (~60°), hence fringes need to be very closely spaced (approx λ) over a reasonably large area (~ 10 mm or more). This requires high resolution, which means large array sizes which correspondingly leads to large data files as well as increased calculation times. A common technique is to use a lens to perform most of the beam focusing, with a CGH to take care of the details of the spot pattern with small deflections about the main focus.

Design of Trapping System

As mentioned previously in chapter 3, high numerical aperture lenses are desired for good optical trapping, therefore microscope-objective lenses are often used. The disadvantage with these lenses is that they have a very small working distance of a few millimetres and, for the purposes of the project; a larger working distance of tens of millimetres is required. Therefore a small F-number (f/1.4) 35mm SLR camera lens with 50 mm focal length and a NA of 0.33 was selected as the lens system. The trapping system was subsequently designed around this.

Rationale

The CGH will be computed as if it was to be used by itself (i.e. without the extra lens). The pattern will then be multiplied by the complex conjugate of the phase function which will be supplied in practice by the lens. This should produce a CGH of relatively low resolution (diffracting power), which nevertheless is properly corrected for aberrations in its focus. A Pentium computer (Core 2 at 1.86 GHz) running MATLAB v5.53 software was used for the calculation of the holographic diffraction patterns. The calculation and subsequent generation of the holographic patterns, using a 1024×1024 array size, was quite fast, approximately 29 seconds for a 32 point source hologram. This increased to approximately 83 seconds when generating a 96 point 'ABC' point source hologram. This suggests a calculation time of ~0.9 seconds per point. These diffraction patterns were then printed using a variety of different printers to test their output qualities. 1024×1024 array sizes were used as this offered the best compromise between fringe resolution, output quality and calculation time.

4.1) Coding Scheme

A point source coding scheme based on first principles, was used in the calculation of the holographic diffraction pattern. Holograms representing a hexagonal close packed (HCP) crystal structure were calculated from a series of point sources spaced over a range of *x, y & z* distances, thus allowing 'A', 'B' and 'C' planes to be created. All coordinates and distances are in mm. The dimensions of the hologram plane are set in the code (e.g. 21.5 mm×21.5 mm) and this corresponds to an array size of 1024×1024. The dimensions were chosen to be this size due to the fact that the lens to be used for hologram reconstruction had a maximum aperture of 35 mm. Each point source gives rise to a spherical wave with a complex amplitude H_P in the form of:

$$H_P = A\left(\frac{z}{r}\right)\exp^{-ikr} \qquad \textbf{Eq. 4.1}$$

$$\text{where } r = \sqrt{(x'-x)^2 + (y'-y)^2 + z^2} \qquad \textbf{Eq. 4.}$$

The equation is normalised so that the amplitude at point ($x'= x$, $y'= y$) on the hologram plane is equal to A (refer to Fig 2.2 for hologram geometry). A function calculates the distance r from the point source to every point on the hologram plane. From this the complex amplitude in the hologram plane is calculated using eq. 4.1. The complex amplitudes for individual points are added together to obtain the final, total complex amplitude which is then multiplied by a phase function simulating a well-corrected diverging lens with focal length f:

$$H_c = \exp^{ikr'} \qquad \textbf{Eq. 4.3}$$

This phase function removes the convergence which will later be supplied by a focusing lens, and in effect, focuses the points at infinity (See Appendix A.1 for full treatment on derivation of lens function). This is desired as the resolution requirements on the hologram to focus at a specific z distance are thereby relaxed. Otherwise, a significantly larger sized array would be needed to satisfy the resolution requirements along with being able to converge the beam at a desired z distance. A reference-less beam coding method [79] is used to convert the complex field pattern to a real intensity pattern (see Appendix A.4) to simulate the result of interference with an on-axis reference beam. The resulting calculations can be expressed graphically as an interference pattern and thus, printed. This interference pattern will act as a diffraction grating when transferred to film by photographic-reduction techniques. It is

important to ensure that the axis of the system is the same for both the lens function and the spherical point source functions. Otherwise, errors such as aliasing can occur if the two functions are not on the same axis.

If the hologram is reilluminated at normal incidence with a plane wave travelling in the same direction as the reference beam, a virtual image of the point sources will be produced on the side of the hologram closest to the reilluminating source. To turn this into a real image, the hologram is reilluminated in the reverse direction. The reilluminating wave is then brought to a set of focused points on the far side of the plate. In fact, the hologram can be used in either orientation: in the first case, the conjugate beam is brought to a real focus, in the second case; the primary image is the real image.

If all points have the same amplitude factor *A*, then a 'uniform phase' hologram is produced. Alternately, a random phase factor may be applied to each spherical wave source, thus becoming:

$$H_p = A\left(\frac{z}{r}\right)\exp^{-ikr}\exp^{-i2\pi\phi} \qquad \textbf{Eq. 4.4}$$

where ϕ is a random number generated between 0 and 1.

Both random phase and uniform phase methods were trialled. Thus the overall equation including the lens phase function is for uniform phase:

$$H_{Total} = \exp^{ikr'}\left(\sum_n A\left(\frac{z}{r}\right)\exp^{-ikr}\right) \qquad \textbf{Eq. 4.5}$$

where *n* is the number of point sources in the light field. For random phase:

$$H_{Total} = \exp^{ikr'}\left(\sum_n A\left(\frac{z}{r}\right)\exp^{-ikr}\exp^{-i2\pi\phi}\right) \qquad \textbf{Eq. 4.6}$$

The coding simulates a HCP crystal structure (see Appendix E for program source code) by generating point sources separated in relation to *d* values, where *d* is the separation between adjacent planes. For example, looking at the 'A' plane of the crystal structure, the separation of points along the *x*-axis is given by $\sqrt{3}d$, while the separation along the *y*-axis is *d/2*. To model this configuration, the program accepts as input the *x, y & z* starting positions (mm)

relative to an origin in the centre of the hologram plane, the *d* spacing (in mm) and the number of points in each row and column. The program will then generate a rectangular grid of points separated by $\sqrt{3}d$ in the *x*-direction and *d* in the *y*-direction. It will then generate a second grid shifted $\sqrt{3}d/2$ along the *x*-axis and downward *d/2* along the *y*-axis. This configuration simulates an 'A' plane in the HCP crystal structure. Therefore, entering 5 as the number of points will result in 50 point sources being generated for the 'A' Plane. The 'B' and 'C' planes are generated in a similar way, with appropriate offset in *x, y* and *z*.

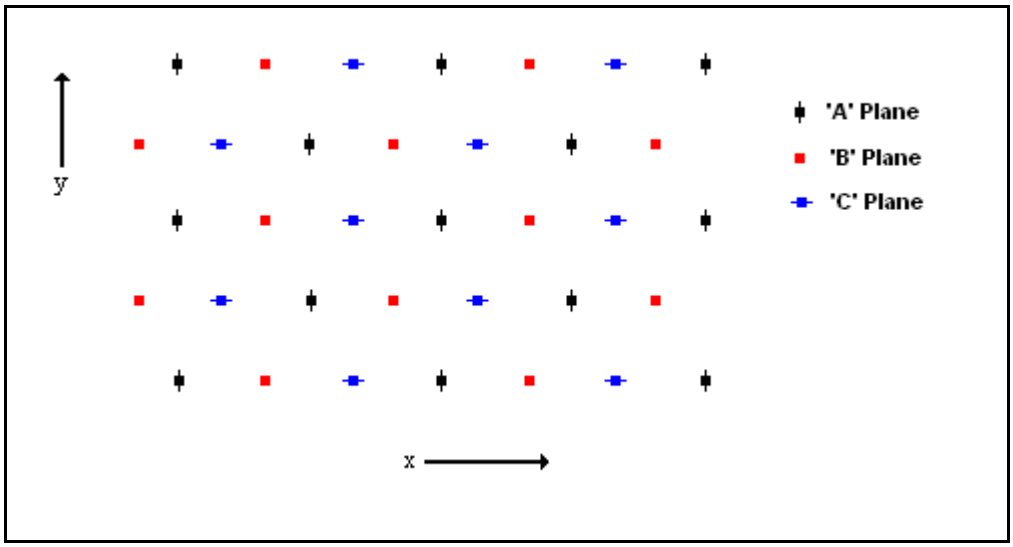

(**Fig. 4.1** HCP crystal structure – 2D view.)

The holograms were generated assuming a wavelength of 514.5 nm and were required to have dimensions of 21.5 mm×21.5 mm using an array size of 1024×1024 pixels. These dimensions were chosen due to several factors:

- The height of the film plate of the camera being used for photographic reduction of the holograms is limited to 25 mm; therefore the reproduction size of the final hologram must be smaller than this.
- A camera lens with a focal length of 50 mm was used in the experimental setup to focus the light field at an initial *z* distance of 50 mm.
- The combination of wavelength, array and hologram size gave a good compromise between minimum resolvable point separation and maximum diffraction angle; where the minimum resolvable point separation in both *x* & *y* directions is determined by:

$$\Delta x_{\min} \geq \frac{\lambda z}{Mdx} \qquad \textbf{Eq. 4.7}$$

where M is the array size and dx is the width of each pixel. The maximum width of the imaged array (and height assuming x & y dimensions are the same) is thus:

$$\Delta x_{\max} \leq \frac{\lambda z}{2dx} \qquad \textbf{Eq. 4.8}$$

This gives the maximum diffraction angle as: $\frac{\Delta x_{\max}}{z} = \frac{\lambda}{2dx}$ **Eq. 4.9**

As can be seen from the above equations; keeping z a constant while decreasing λ results in greater resolvability but limits the maximum width available for the hologram while increasing λ has the opposite effect. The same applies if λ is kept constant and z varies. Also increasing the size of the hologram (Mdx) should give greater resolvability but unless the array size M is increased and pixel width dx is decreased to compensate, the diffraction angle dramatically decreases (See Appendix A.3 for full mathematical treatment).

4.1.1) Test Pattern Method

To test hologram efficiency and performance, especially around the edges, two types of test patterns have been developed. One method called *Testsph,* constructs a series of 5 coplanar point sources in an upright cross pattern separated by 50 µm, from 9 individual holographic diffraction patterns. Each individual holographic diffraction pattern contributes to only one point in the final imaged array. The individual holograms are first generated in a 1024×1024 array, and then cropped so only two square portions (for example; the top left and bottom right) remain. The rest consists of a blank background. These individual diffraction patterns are added together to form a final hologram. Ideally, the reconstructed output should consist of 5 focused points separated by 50 µm. The performance of the hologram can then be judged by how well the contributions from opposite squares overlap at the point of focus. The individual points along with their associated hologram portions are shown in Table 1, where north, south, east and west refer to the top, bottom, right and left portions respectively of the diffraction pattern in Fig. 4.1.1a

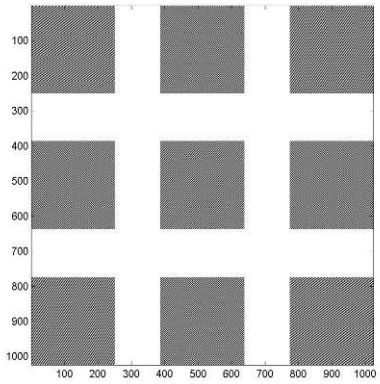

(Fig. 4.1.1a *Testsph* Holographic diffraction pattern.)

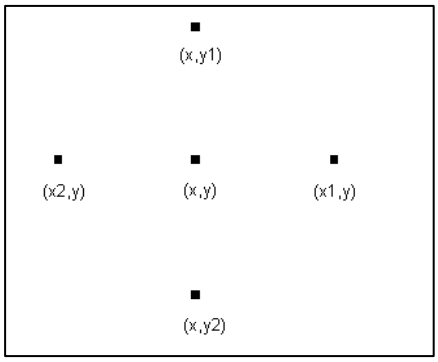

(Fig. 4.1.1b *Testsph* Point configuration.)

Point	Hologram portion
Centre point (x, y)	centre portion
Point (x, y1)	east & west portions
Point (x, y2)	northeast & southwest portions
Point (x1, y)	north & south portions
Point (x2,y)	northwest & southeast portions

(Table. 1 *Testsph* point coordinates and associated hologram portions.)

The diffraction pattern of *Testsph* is shown in Fig. 4.1.1a along with the associated point source configuration in Fig. 4.1.1b.

Another method called *Testpoint,* consisted of a single hologram again consisting of 5 different points arranged in an upright cross position. The points are again separated by 50 µm. The difference with this method is that a single diffraction pattern is generated instead of individual ones for individual points. The generated diffraction pattern is broken up into 9 individual squares. Since each of these squares is part of the original hologram, the combination of all 9 will reproduce the original image of 5 points. The performance of this hologram can be evaluated by blocking off individual squares of the hologram in turn and inspecting the effect on the quality of the generated image.

The two different methods should give the same output during holographic reproduction as the point coordinates and the initial (*x, y*) starting positions are the same for each. Since a 50 mm camera lens is being used to focus the holographic image, both holograms were designed with a *z* distance of 50 mm.

4.2) Photographic Reduction

The printouts were photographically-reduced to photographic film to form the final hologram whose size was required to be ≈ 20 mm (later 21.5mm) square. The camera has to be placed at a specific distance from the pattern to ensure the proper reduction ratio for the hologram. This reduction ratio is based on the formula

$$D_o = \frac{f}{M}(1+M) \qquad \textbf{Eq. 4.8}$$

where D_o is the distance required from the original printout to the film plane, f is the focal length of the camera lens and M is the desired magnification factor, given by: $M = \frac{I_F}{I_I}$ where I_I and I_F are the initial size of the printed diffraction pattern and the final size of the hologram respectively. The I_I value is independent of any calculation and is the result of using the maximum available paper area for printing. Once this value is known, then D_o can be calculated. Using a camera lens of f = 55 mm (nominal) and calculating for a hologram size of 21.5 mm×21.5 mm, the resultant D_o value is shown in Table 2 below.

Paper size:	A3	A4
Image size on printout: (mm)	272	202
D_o predicted with f = 55 mm: (mm)	751	572
Actual D_o required for desired image size: (mm)	814	620

(**Table 2**. D_o values required for A3 & A4 printouts.)

As seen in Table 2, the actual length from the camera to the print out required to get the desired de-magnification was slightly higher than the calculated theoretical value. This is due to the variation between the stated and actual focal length of the lens. Using the theoretical values of D_o in an initial recording process, it was found that the dimensions of the photographic reductions were approximately 23.5 mm × 23.5 mm. This would be consistent with the lens having an actual focal length of approx. 59.6 mm. Using this new value for f and substituting it into Eq. 4.8, corrected D_o values can be found. These new values gave the proper size of the final hologram.

4.2.1) Types of Film

Initially, Agfa 8E56 holographic film was used in photographing early diffraction patterns. However, due to the age of the film stock (around 30 years), the film had deteriorated in quality. This was evident in the large exposure times necessary for recording (in the order of 2 minutes). This is not desirable as, over time, mechanical drifts and vibrations can blur the images.

A 35 mm Nikon F2 camera with a high resolution MicroNikkor 55 mm focal length lens set at varying apertures along with Kodak Kodalith 35 mm high contrast slide film were used to photograph the patterns. The 55 mm lens was chosen due to its excellent flat field characteristics. Two Broncolor MiniCom 80 lamps were used to illuminate the patterns. The Kodalith film behaves almost digitally in its interpretation if something is to represented as 'black' or 'white', therefore it was hard to achieve good tonality in the film which is required as some of the diffraction patterns (the uniform phase type) possess a high degree of tonality. However, the advantage of this film is its high ISO (8-12 depending on the illuminating source) which is high compared to holographic film and it has high resolution for a photographic film. It was difficult to have a standard aperture setting for the camera lens due to the high contrast nature of the Kodalith film and the slight variations in each pattern. For example, a standard lamp power/aperture setting would give rise to variations in exposures for the different diffraction patterns. Therefore, each pattern was photographed with a range of lamp power/ aperture settings and the most suitable exposure would be selected. After exposure, the film was developed for 3 min in a 1:1 mixture of diluted Ilford Iltholith DL A & B. The manufacturer's recommended time, agitation and dilutions were used. The film was fixed normally for 3 minutes. The film was rinsed with water for 10 min and then allowed to dry. Figure 4.2.1 shows the layout of the photographic-reduction and recording process.

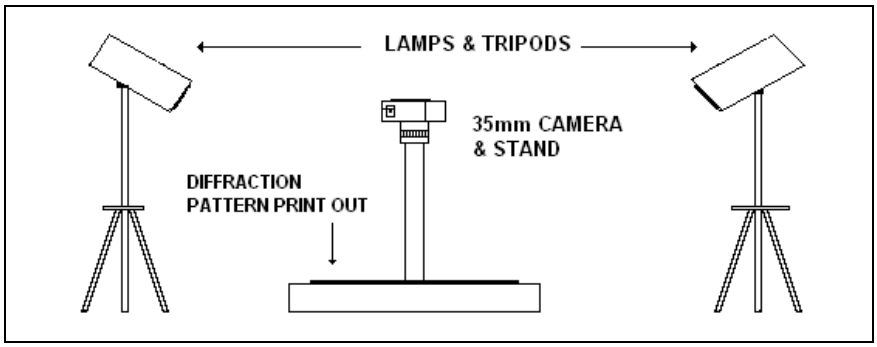

(**Fig. 4.2.1** Photographic-reduction and recording setup.)

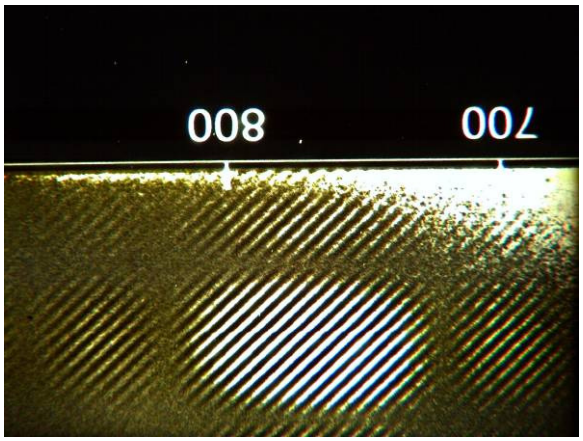

(**Fig. 4.2.1a**. Kodalith film.)

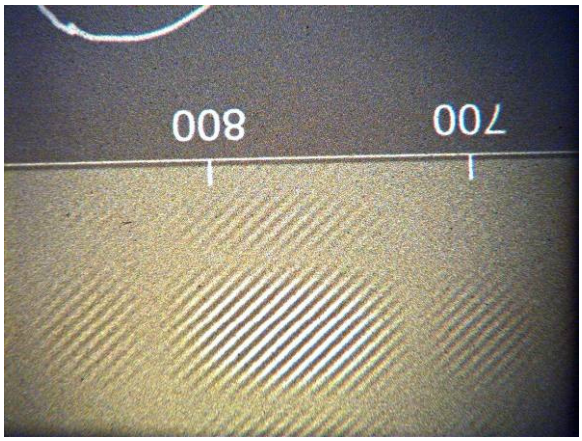

(**Fig. 4.2.1b.** Ilford FP4+ film.)

Due to the extremely high contrast of the Kodalith film, which resulted in some uneven exposures across the various recorded patterns, it was decided to try an alternative; Ilford FP4+ 35 mm film. It was found that while the resolution was adequate for our purposes, there wasn't enough contrast in the film to adequately reproduce the interference fringes. This reduces the diffraction efficiency in the final display (i.e. fainter holograms). Figures 4.2.1a & b show the same diffraction pattern viewed under a Zeiss 'Ultraphot' microscope with the Kodalith and FP4+ films respectively. Notice that while the resolution is approximately the same, there is a notable difference in contrast between the two films.

A reversal bleach process was trialled with the Kodalith film in an effort to improve the efficiency by physically converting the hologram (i.e. film) from an amplitude to a linear phase hologram (as described in section 2.2.1). This reversal bleaching process has proven to be very effective when applied to holographic film in conventional holography. However, this method was unsuccessful with the Kodalith film as the diffraction efficiencies of the bleached holograms were found to be inferior in quality to the holograms produced using the development/fixing method outlined above. This suggested that the bleaching recipe was not

optimised for the Kodalith film. Time constraints prevented further investigation of alternative bleaching techniques for Kodalith film.

4.3) Holographic Display

The initial illumination of the holograms used the set-up shown in Fig. 4.3a. The laser used was a Spectra Physics Model 2060 Ar^+ laser with wavelength 514.5 nm. The 514.5 nm line was chosen over other lines due its relatively high output power and the fact that it offered the best compromise between resolvability and diffraction angle (with longer wavelengths having a greater diffraction angle but lower resolvability). When viewing the hologram through an eyepiece, an optical filter has to be placed in front of the laser to avoid injury as the Ar^+ laser is quite powerful (Class 4). The beam reflected off a series of mirrors then it passed through a spatial filter (40x objective lens, 25 μm pinhole aperture) which was used to expand the beam. The 40x microscope-objective (or any microscope-objective) produces a diverging beam; however the expanded beam tends to be quite 'messy' with variations in intensity due to high spatial frequencies present in the original beam as well as imperfections present in the objective. A pinhole aperture is used to 'clean' up the beam profile as it attenuates these frequencies and provides uniform intensity and phase across the beam. The expanded beam travelled through a good quality collimating lens, producing uniform plane waves. The beam then passes through the holographic film, which rests on a plate with a variable aperture to control the area of the beam passing through. A 50 mm camera lens (Asahi Super Takumar 3430617) is placed on top of the film. It is important to ensure that the beam passing through the film passes through the middle of the lens. After passing through its focus, the beam goes through a magnifier (Zeiss Ultraphot 10x objective lens) which then focuses it onto the detector array of a digital camera for viewing by a computer. A Mightex CMOS camera (1280x1024 pixels with a pixel spacing of 5.2 μm), controlled by a PC was used in the capturing of holographic images. The camera's exposure can be controlled by the computer to produce acceptable images.

The setup shown in Fig. 4.3a was subsequently altered with the film holder, 50 mm lens, objective lens and camera mounted horizontally on an optical rail in an effort to increase stability and improve control of the set up (Fig. 4.3b). The 40x objective lens in the spatial filter arrangement was replaced with a 10x objective to reduce light leakage.

Correspondingly, the 10x magnifying objective lens was replaced with a 40x to ensure that it had a large enough numerical aperture to comfortably resolve detail in the imaging plane (see appendix A.5). When viewing the holographic image, the 50 mm lens could be adjusted horizontally to improve focus.

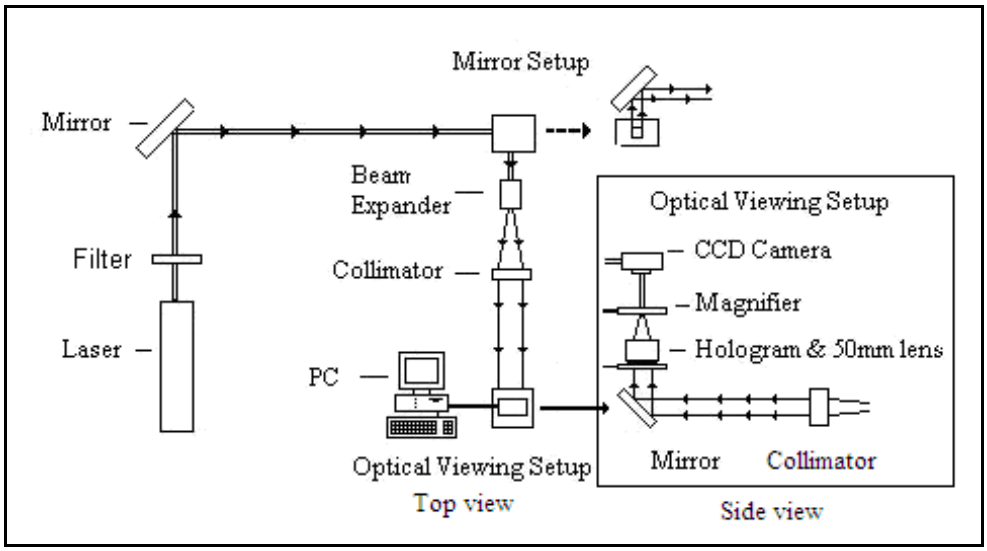

(**Fig. 4.3a** Initial Holographic display with vertical mounted set up.)

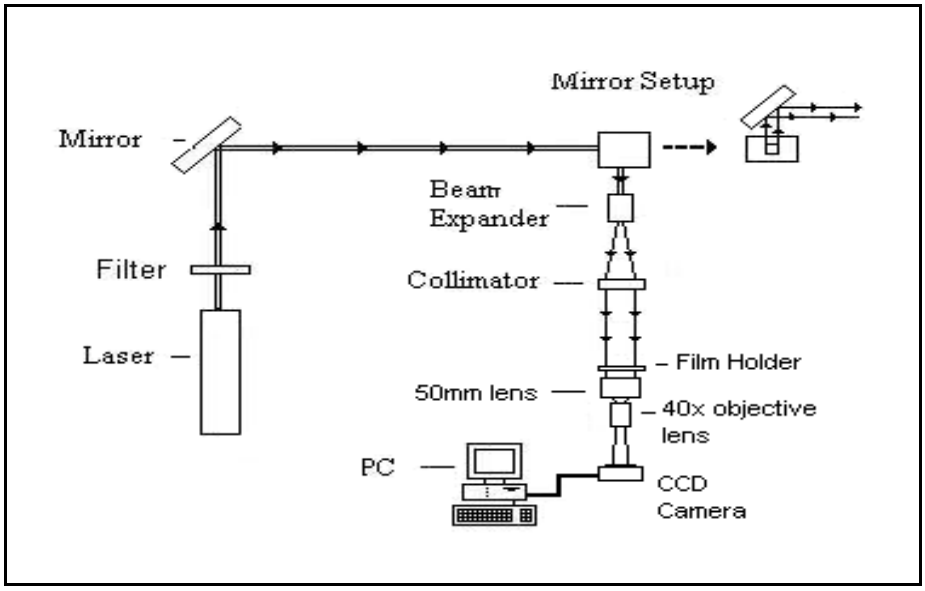

(**Fig. 4.3b** Holographic display with horizontal mounted set up.)

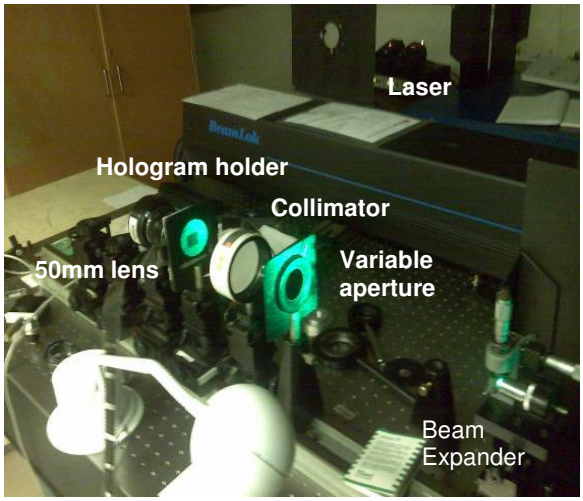

(Fig. 4.3c-1 Side view of viewing arrangement.)

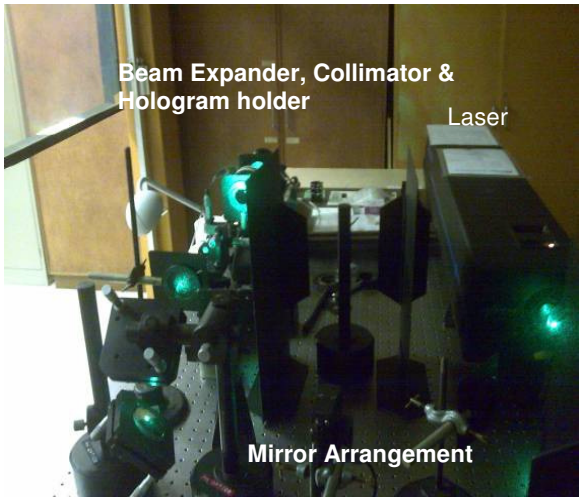

(Fig. 4.3c-2 Mirror arrangement.)

Figures 4.3c-1 & 2 are images of the holographic display setup shown schematically in Fig. 4.3b. Figure 4.3c-1 is a side on view which shows (from right to left) the beam expander, variable aperture, collimator, film holder and 50 mm lens. The objective lens and digital camera are not in place. Figure 4.3c-2 shows the laser and mirror arrangement in greater detail, especially the angled mirrors in the left of the image.

4.4 Spherical Aberration Measurements

To determine the amount of spherical aberration present in the 50 mm camera lens used for reconstruction, measurements were undertaken to record the phase curvature of the lens by photographing the interference pattern caused by light exiting from the camera lens interfering with plane waves created by a high quality collimating lens. The experimental set up is shown in Fig. 4.4. The laser used is Spectra Physics Model 2060 Ar^+ laser with wavelength 514.5 nm. The two beam expanders in the set up each contain a 10x microscope objective and a 25 µm pinhole aperture.

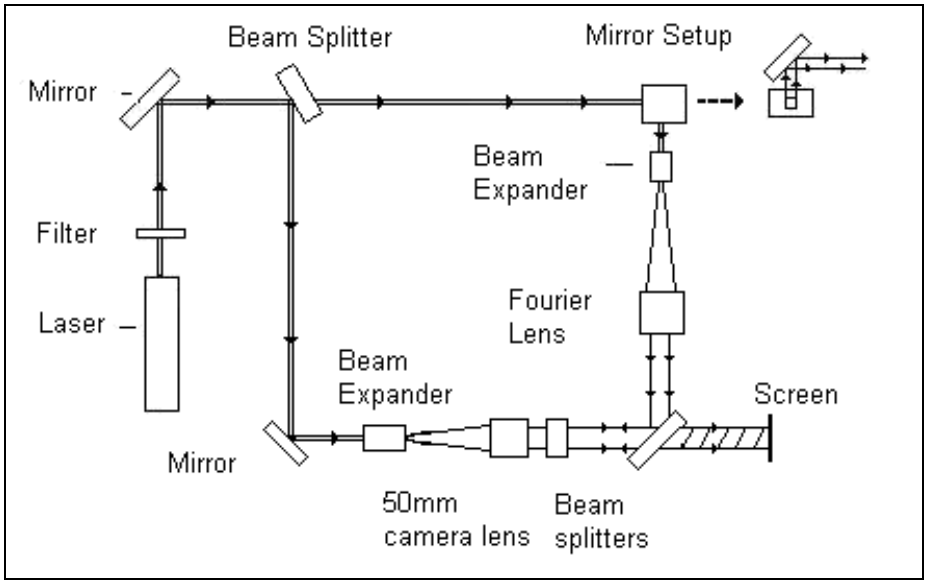

(**Fig**. 4.4 Phase Curvature experimental set up.)

A reference plane wave was created with a 485 mm focal length lens from a Fourier bench. A point source was created in the focal plane of the 50 mm lens with a beam expander. The wave transmitted by this lens was combined with the reference plane wave reflected from a flat $\lambda/4$ beam splitter which was placed in the same plane relative to the lens as the final hologram would be. The interference pattern produced was photographed using 50 mm large format slide film and the resulting fringe pattern was analysed. The pattern showed a relatively small change in phase across the centre of the lens; however the phase change became greater near the edges as evident in the closely spaced fringes. The film was placed into a scanner and the position of the fringes from the resulting images could be accurately plotted. The results from these tests will be explored in chapter 5.3.

4.5) Colloidal Trapping Set-up

While the setups shown in Fig. 4.3a & b were adequate for viewing holographic images, they weren't suitable for undertaking trapping experiments. In an effort to improve the efficiency of the setup and to impose greater control over the various optical components, the set up was modified again (see Fig. 4.5). The various beam steering mirrors were replaced with two multi-layer dielectric coated mirrors. These have a lower absorption (less than 1%) compared to the previous multi-coated mirrors employed [80]. The 10x objective previously used in the

beam expander setup was replaced with a 4x due to concerns over power loss in the system as there was light leakage occurring. The 4x produced a narrower beam profile, better matched to the area of the hologram. The new setup resulted in system with an overall transmission of ≈ 40% without a hologram inserted, which was an improvement over previous systems. However, introducing a hologram slide into the system increased the power loss significantly. The power loss in the system will be discussed in greater detail in the following chapter. Light from an incandescent lamp was introduced into the arrangement through another beam splitter to provide background illumination when viewing the colloidal system. The colloidal liquid was injected onto a clean, uncovered welled glass slide which was placed in a sample holder between the 50 mm lens and the 10x magnifying microscope objective. A high-density filter, taken from laser safety glasses, was placed over the microscope-objective to decrease the intensity of laser light entering the digital camera, while still transmitting light from the incandescent lamp. The arrangement produced a good balance between background and laser illumination at the camera.

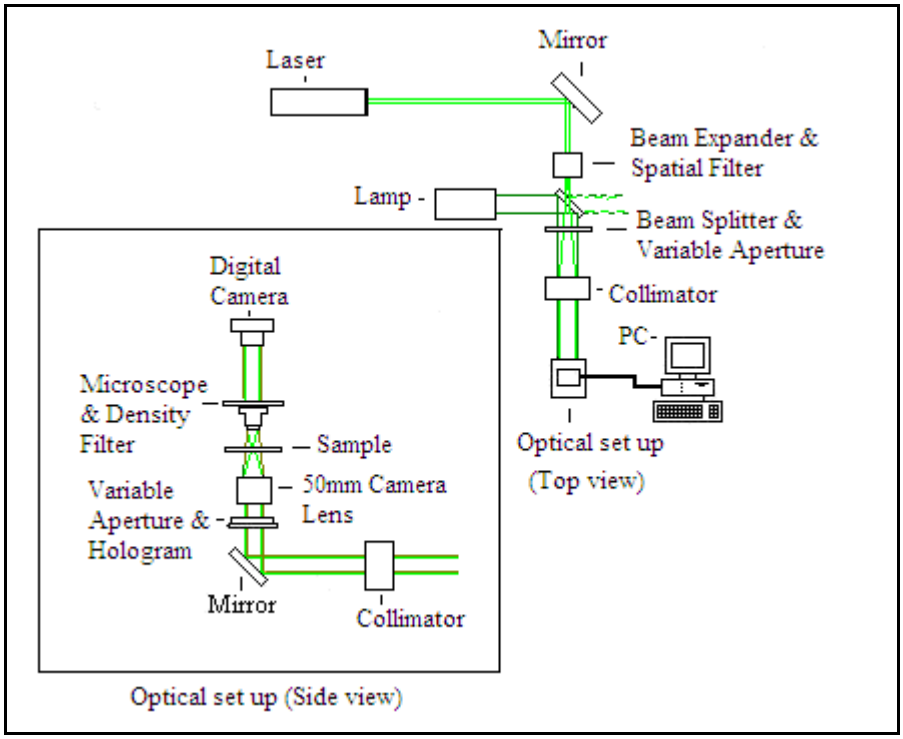

(**Fig. 4.5a** Holographic display & trapping set up.)

4) Experimental Methods

The camera allowed for the viewing and recording of trapping events. The Mightex CMOS camera did not have a video recording function which made it impossible to capture trapping events automatically over time. To overcome this, individual images were captured in quick succession and, using Windows Movie Maker, videos showing trapping occurring could be created.

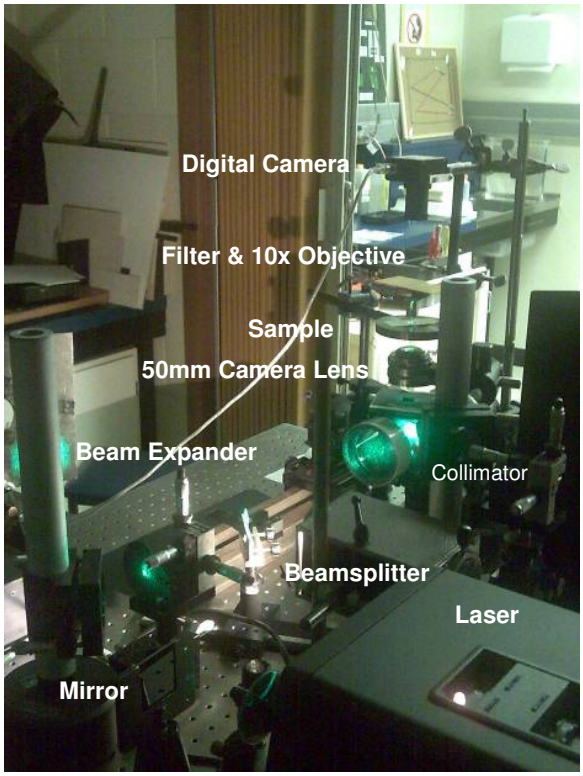

(Fig. 4.5b-1. Trapping arrangement–overview)

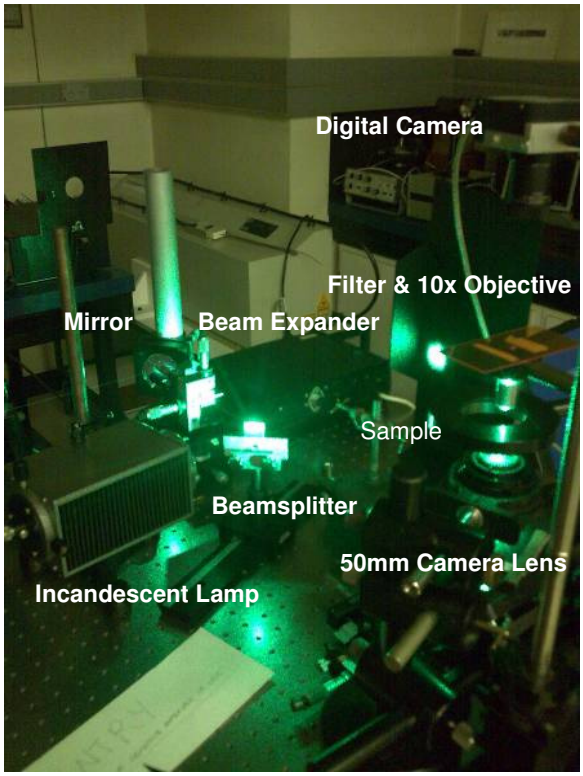

(Fig. 4.5b-2 Incandescent lamp and beamsplitter arrangement)

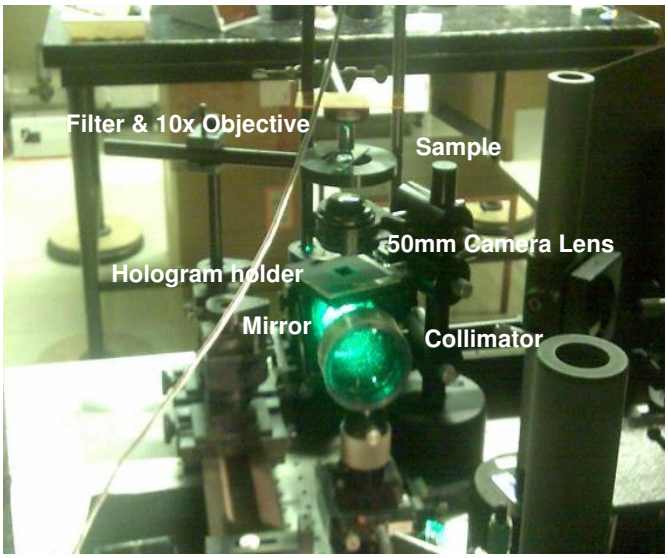

(Fig. 4.5b-3. Detailed view of trapping arrangement)

Figures 4.5b-1-3 shows images of the actual experimental set-up from three different perspectives. Figure 4.5b-1 shows the laser being reflected off the dielectric mirror (in left of image) and passing through the beam expander, beam splitter and through the collimating lens. What is not evident from this image is the angled dielectric mirror directly behind the collimator. This reflects the beam upwards, passing through the hologram holder, 50 mm lens, through the sample slide and into the 10x objective, which then focuses onto the digital camera. Figure 4.5b-3 shows the trapping setup in greater detail with the mirror visible behind the collimator. Also visible in this image, is the laser-blocking density filter obtained from laser safety goggles. Figure 4.5b-2 shows the beam splitter arrangement, with laser light reflecting off the angled beam splitter. The incandescent lamp is the rectangular object situated in the left side of the image. The first dielectric mirror as well as the beam expander is evident, with the pinhole aperture clearly visible in the setup.

4.6) Computer Simulated Reconstruction

Reconstruction of holographic images from the CGHs could be simulated using MATLAB. To achieve this, the final hologram array is simply Fourier transformed using the FFT functions. The absolute value of the resulting array is squared and the result of this simulates the reconstructed object. This process is rather useful in determining whether the coding of the hologram has been successful and in checking the position of the hologram image. However errors arise in using the FFT algorithm, due to the fact that it relies on the validity of the Fourier approximation, whereas CGH calculations do not. This results in the simulated image appearing blurred and therefore this method does not give an accurate representation of the actual holographic reconstruction. Examples of simulated reconstruction hologram images can be found in the next chapter.

5) Computer Generated Light Fields- Results

Different computational techniques, such as those employing the FFT algorithm (see Appendix D), were trialled before the point source coding method was selected as the preferred technique. Since the FFT method was an approximation and did not give full control over point position and spacing, it was decided that a coding scheme employing the diffraction integral directly would be more suitable since it offered greater freedom in point configurations, and should in theory lead to better results. The other methods were founf to produce inferior quality holograms and because of this, no holographic images are shown employing these methods.

Also to begin with, many holograms were created and tested using Agfa 8E56 Holographic film. Unsatisfactory results were obtained using this film which was due to the film stock's age and the long exposure times needed. An alternative film, the Kodak Kodalith 35 mm slide film was used as a substitute in lieu of holographic film. The images shown in this section make use of the Kodak film.

5.1) Test pattern results

Simulated Reconstruction

As described in Section 4.1.1, two test pattern holograms *Testsph* and *Testpoint* were generated to study aspects of reconstruction. Firstly, the reconstruction was simulated using the FFT function in MATLAB to perform a 2D FFT on the hologram data array. This is useful for simulating far-field diffraction but introduces errors when simulating near-field (or Fresnel) diffraction. The test pattern holograms are designed to give good focused points when used in series with a well-corrected converging lens of 50 mm focal length. A 2D FFT of the hologram produces an image containing inverse spherical aberrations which should not appear in the image when reconstructed in practice. Figures 5.1-1a and 1b show the MATLAB reconstruction:

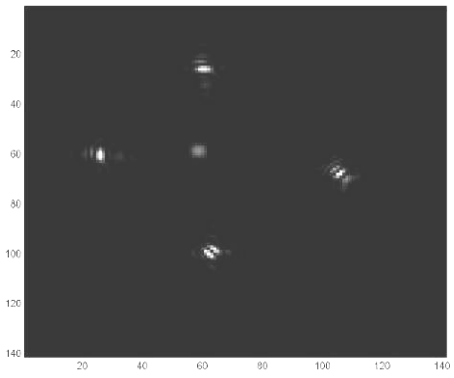

(Fig 5.1-1a. Reconstructed image of *Testsph***.)**

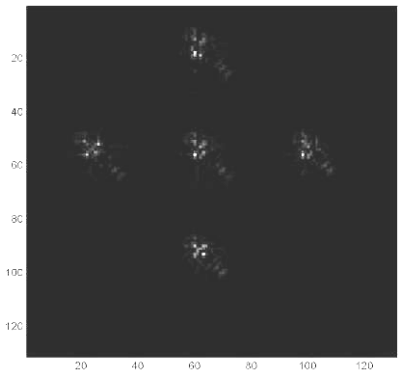

(Fig 5.1-1b. Reconstructed image of *Testpoint.***)**

As can be seen, the simulated images differ from each other. The point sources in the *Testsph* image (Fig. 5.1-1a) are not evenly spaced and the middle point is rather weak. This is expected, since only one portion of the total hologram is contributing to this point compared to two portions for the other points. The *Testpoint* reconstruction shows evenly spaced points, but with considerable aberration detail surrounding each point. Comparison with Fig. 5.1-1a shows where some of this aberration comes from. For example, the rightmost point in Fig. 5.1-1a, which is generated by diagonally-opposite corners of the hologram, is displaced to the right and down from its expected position. This contribution is more faintly visible in each of the points of Fig. 5.1-1b. The reconstructed points are blurred because different areas of the hologram are producing rays which converge to slightly different points. This may be due to the approximations in the FFT reconstruction.

Actual Reconstruction

(Fig. 5.1-2a Reconstructed image of *Testsph*.**)**

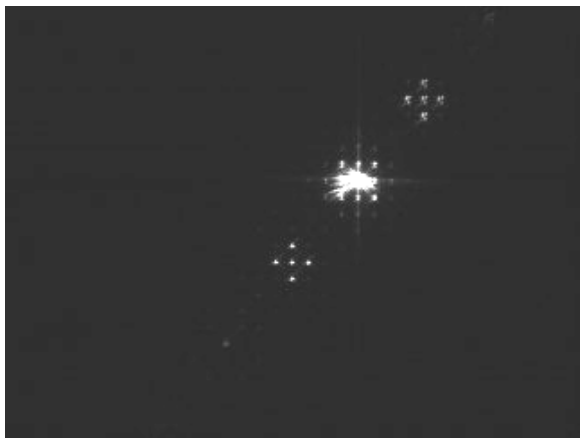

(Fig 5.1-2b Reconstructed image of *Testpoint*.**)**

Figures 5.1-2a & b show the same holograms reconstructed on the optical bench, using the setup of Fig. 4.3a. These holograms both employed the uniform phase technique and both clearly show the primary and conjugate images on either side of the direct beam, with one in focus. Both images are quite similar to their simulated reconstructed image counterparts, but the severity of aberrations seems to be reduced. The aberrations around the reconstructed points in *Testpoint* are not as apparent as they are in the simulated reconstruction. The point sources in the reconstructed image of *Testsph* still seem to be unevenly spaced which is similar to the reconstructed image of *Testsph.* This may be evidence of residual, uncorrected aberrations.

5.2) Uniform and Random Phase Techniques and Clipping

Sometimes, it is advantageous to apply random phases to the point sources of the hologram, which has an effect similar to a diffuser in the object plane. The resultant diffraction pattern then contains a more spatially-uniform distribution of power with less dynamic range, thus making photographic reproduction easier. This can be accomplished by multiplying each point source by a random phase function; $H = \exp^{i2\pi\phi}$ where ϕ is a random number. The random phase factor reduces the dynamic range of the hologram by diffracting information more uniformly across the spatial frequency spectrum. The disadvantage of the random phase is that in the presence of aberrations, a speckle pattern may emerge which can lead to degradation in the holographic image. Several tests were conducted testing the simulated and actual output of holograms with a) a uniform phase, and b) a random phase applied to try and find the most suitable method. The diffraction patterns produced from the random phase technique are more suited to the film being used as there is a greater fringe visibility across the whole area of the hologram. The diffraction patterns produced from the uniform phase technique have a high dynamic range which results in poor contrast in between the principal interference maxima (evident in the large amount of 'grey' in the pattern). It can be difficult for the printer and photographic film to adequately capture and display these patterns. Figures 5.2-1a & 2a show the diffraction patterns resulting from a single HCP 'A" plane of 50 points with a *d* spacing of 0.01mm generated in a 1024×1024 array. Notice the difference in contrast between the two patterns as a result of the high dynamic range of the uniform phase method and the introduction of a random phase function. Figures 5.2-1b & 2b show a magnified

portion of the same diffraction patterns in Figures 5.2-1a and 2a respectively. The difference between the two methods in fringe detail is clearly visible.

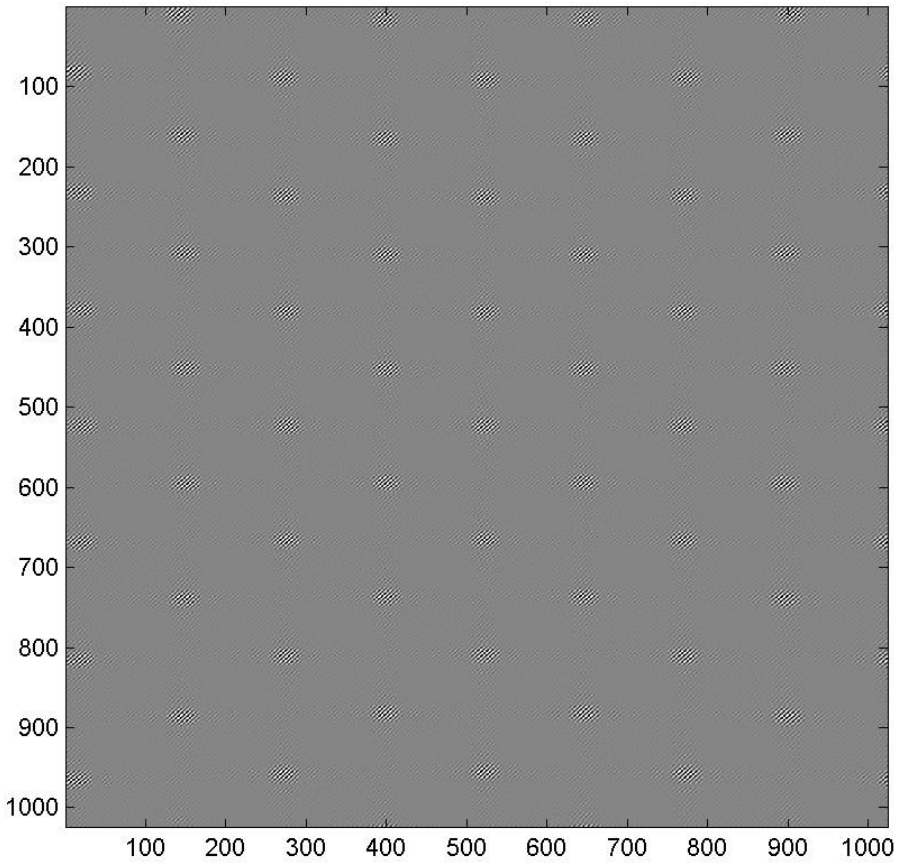

(**Fig. 5.2-1a** *d* spacing = 0.01mm, uniform phase diffraction pattern.)

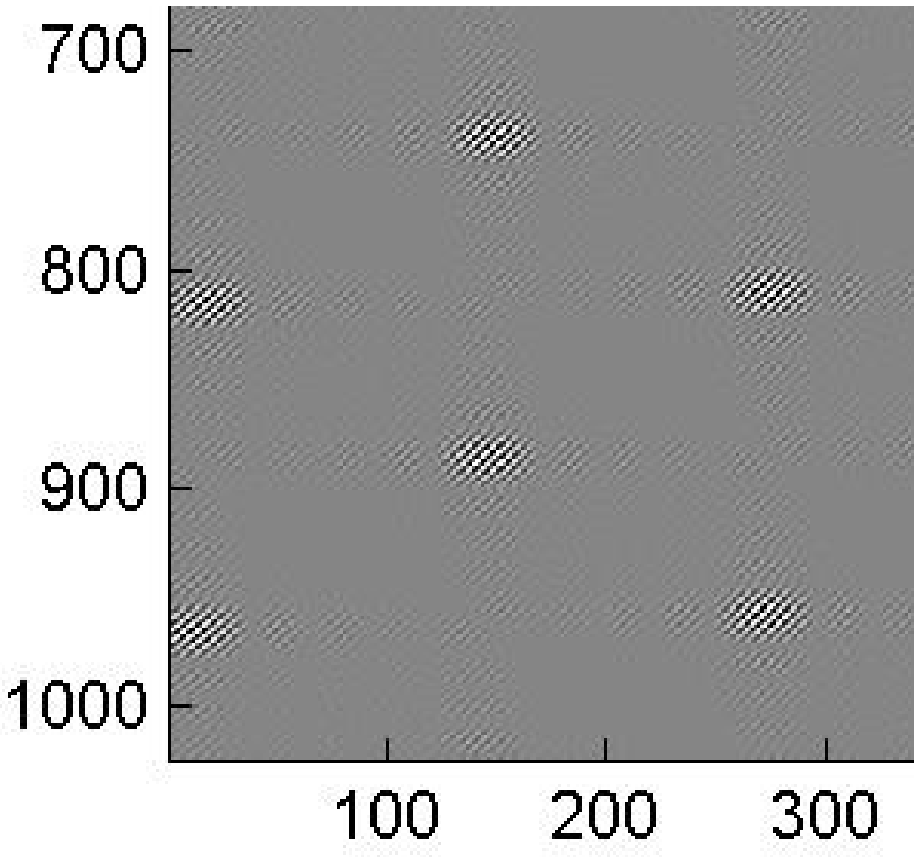

(**Fig. 5.2-1b)** Magnified uniform phase diffraction pattern.)

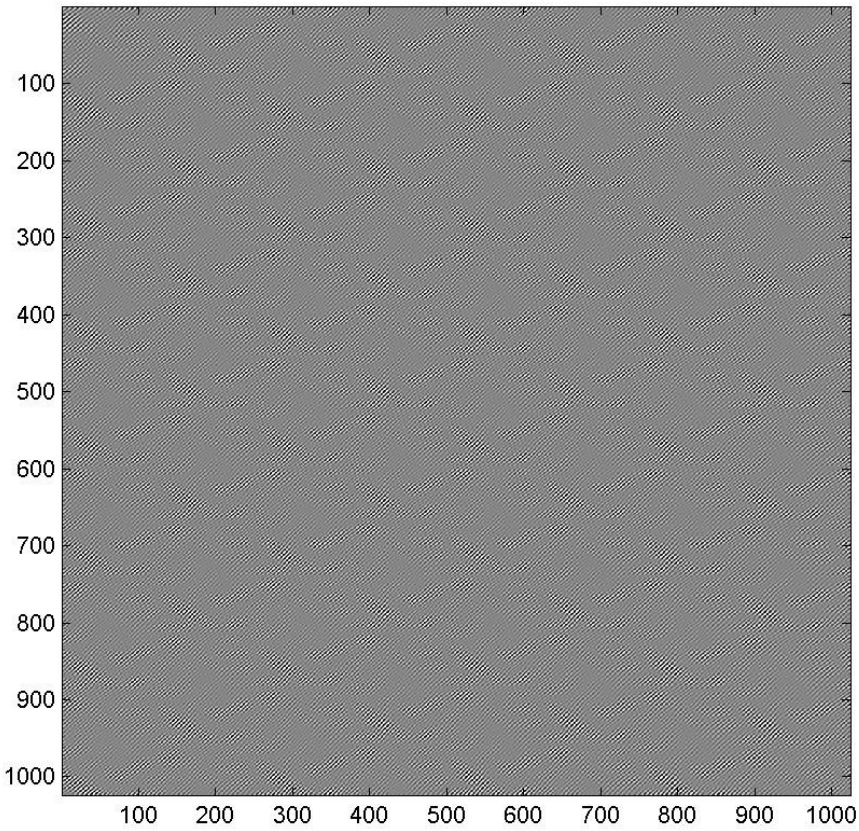

(Fig. 5.2-2a *d* spacing = 0.01mm random phase diffraction pattern.**)**

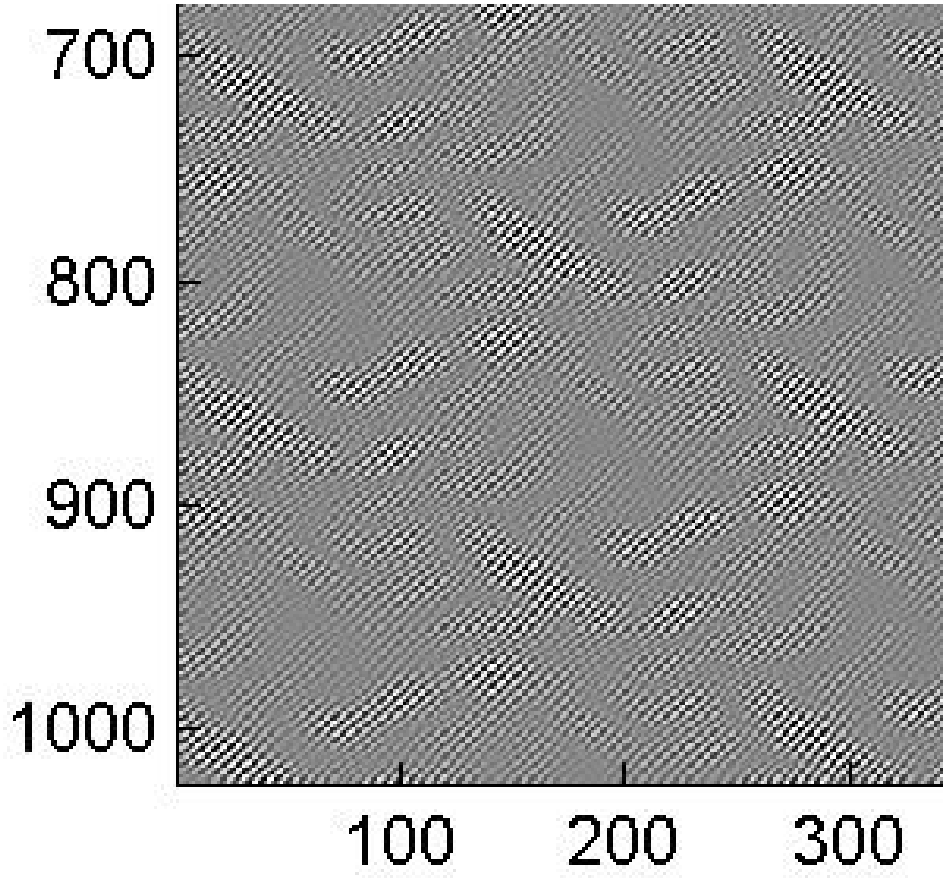

(**Fig. 5.2-2b** Magnified random phase pattern.)

The numerical reconstruction using a 2D FFT of a single HCP 'A' plane of 50 points with a *d* spacing of 0.01mm is shown in Figures 5.2-3a & b.

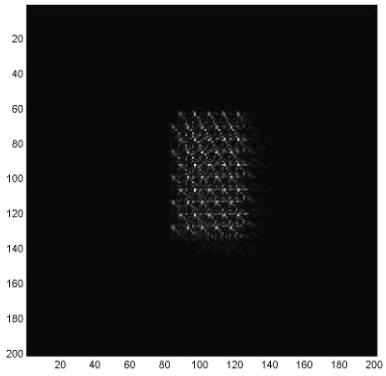

(**Fig. 5.2-3a** *d* spacing = 0.01mm uniform phase.)

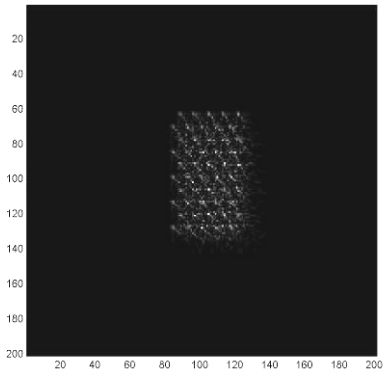

(**Fig. 5.2-3b** *d* spacing = 0.01mm random phase**.**)

Both methods give quite similar outputs, especially at larger *d* values. The random phase method tends to deteriorate when the *d* spacing gets smaller. This is expected as the associated speckle pattern will become more prominent. MATLAB cannot accurately reproduce the point sources in either case. This is evident in the almost triangular shape of the

individual points. These errors are a result of the fact that the 2D FFT method does not accurately simulate the effect of an applied spherical lens.

Another technique used to improve hologram pattern contrast was clipping. The output from the CGH program was normally an image file scaled so that the highest magnitude was 1.0, represented by a grey scale level of 255 (white), and the lowest magnitude was 0, represented by black. Contrast of fringes could be improved by clipping the file so that all magnitudes above a certain maximum value I_{max} (typically 0.8) were set to I_{max}, and all values less than a minimum I_{min} (typically 0.15) were set to I_{min}. The image was then rescaled between these values so that the range I_{min} to I_{max} was stretched to occupy grey levels 0 to 255. This process can improve the efficiency of the hologram, at the expense of introducing more power in the higher orders of diffraction due to the nonlinear scaling. No attempt was made to transform the digital data to compensate for the nonlinear response of the film, because any such correction would be insignificant compared with the nonlinearities introduced by clipping.

Actual Hologram Reproduction

The following images show reconstructions of holograms generated through different coding techniques, different configurations and different output printers. The images were all captured using a Mightex CMOS monochrome camera with global gain set to 2 and 1:2 decimation turned off. Figure 5.2-4 shows the accompanying scale for the following images captured using a 10x objective lens. The scale image was of a 1 mm rule and each small division is 10 µm while each large division represents 100 µm. The following holograms were recorded using the display set up shown in Fig. 4.3a.

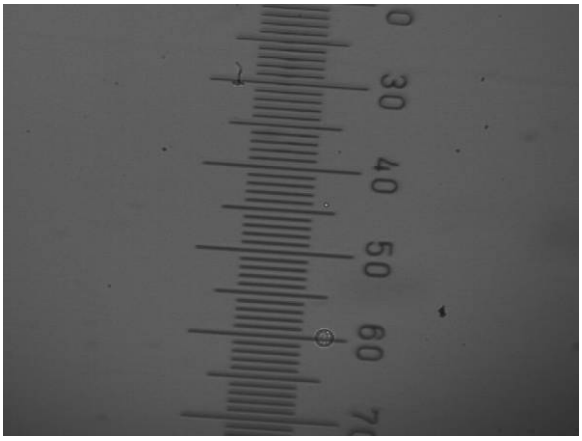

(Fig. 5.2-4 Scale image showing 10µm spacing**.)**

5.2.1) Severe Clipping

The dimensions of the following images are 1280×1024 pixels.

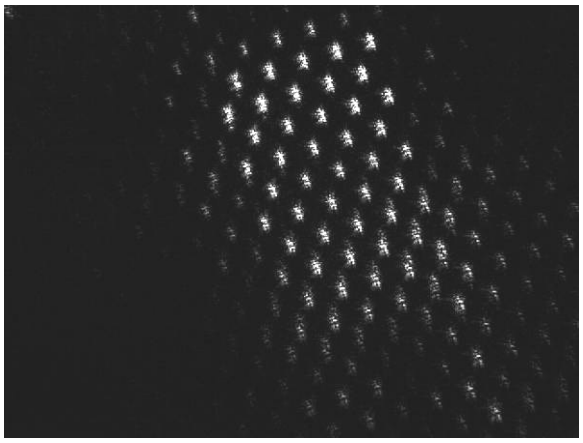

(Fig. 5.2.1-1 *d* spacing = 35 µm uniform phase**.)**

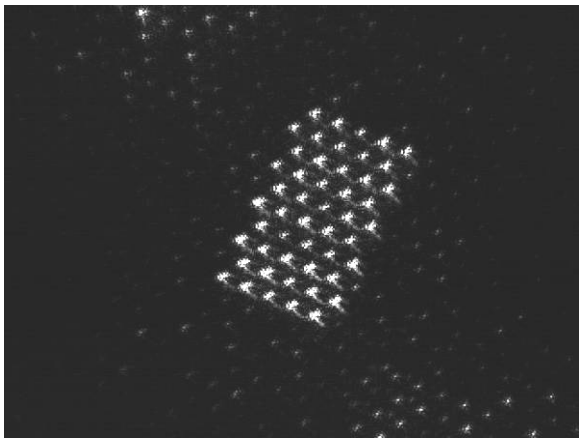

(Fig. 5.2.1-2 *d* spacing = 35 µm random phase**.)**

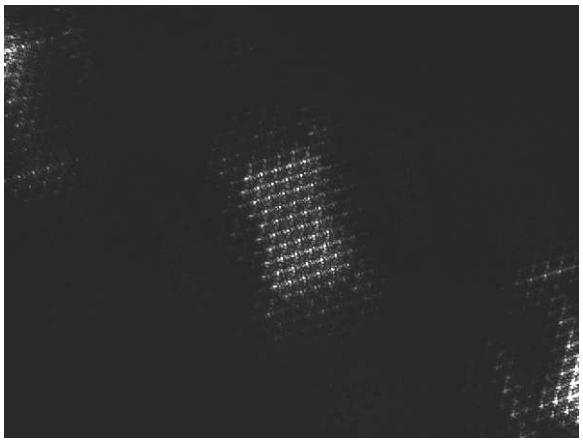

(Fig. 5.2.1-3 *d* spacing = 15 µm uniform phase.**)**

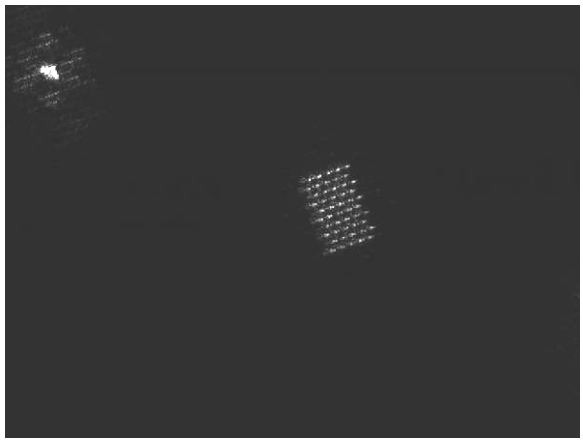

(Fig. 5.2.1-4 *d* spacing = 15 µm random phase**.)**

Figures 5.2.1-1–4 show the holographic output of a single 'A' plane generated with two *d* spacing's for both the uniform & random phase methods. These images are magnified by a 10x lens and captured on a digital camera. The output diffraction pattern for each hologram was severely clipped using the *clip* function (Appendix C) to obtain a suitable image with good contrast. Although it may not be readily visible in the above images, the amount of clipping used resulted in a large number of ghost images (especially in the uniform phase holograms) and increased power in the higher diffraction orders. Table 3 shows the common hologram specifications for the four images.

Hologram specifications	
Array Size:	1024×1024
x,y starting position:	0.2 mm
Number of Points:	50
z distance:	50 mm
Diffraction pattern clipped between (full scale 0-1):	(0.3 – 0.65)
Printer used:	Ricoh Aficio 2060 PCL 6
Output quality:	1200 dpi
Graphics mode:	Vector

(Table. 3 Hologram specifications for single 'A' plane holograms with severe clipping.**)**

It is noticed that the uniform phase method results in an increase of 'ghost' images compared with the random phase method. This could be caused by a number of factors; foremost being the severe clipping being applied to the diffraction pattern which reduces the dynamic range of the pattern. Since the uniform phase method has a larger dynamic range than the random phase to start with, clipping has a larger effect on it. Although it is difficult to determine from the above images; the random phase method produced light fields with greater intensities than the uniform phase method.

5.2.2) Reduced Clipping

The dimensions of the following images are 1280×1024 pixels. The holograms were coded using the random phase technique. Figure 5.2.2 shows the accompanying scale for the following images captured using a 10x objective lens. The scale image was of a 1 mm rule and each small division is 10 µm while each large division represents 100 µm.

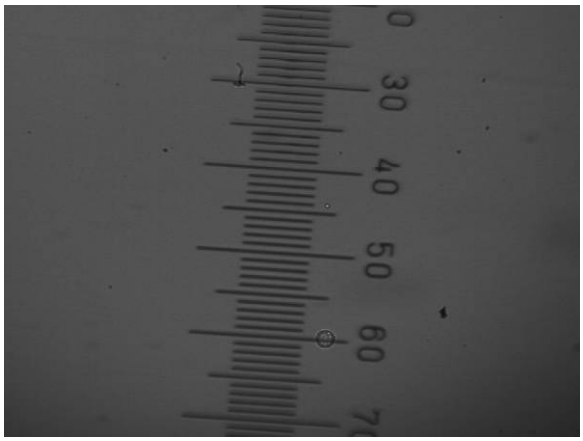

(Fig. 5.2.2 Scale image showing 10 µm spacing**.)**

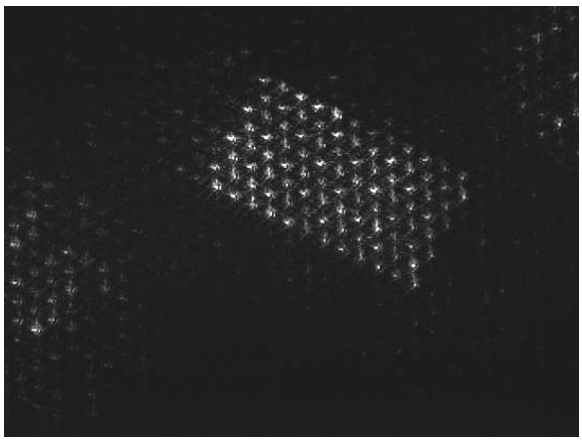

(Fig. 5.2.2-1 *d* spacing = 35 µm 'B' plane in focus**.)**

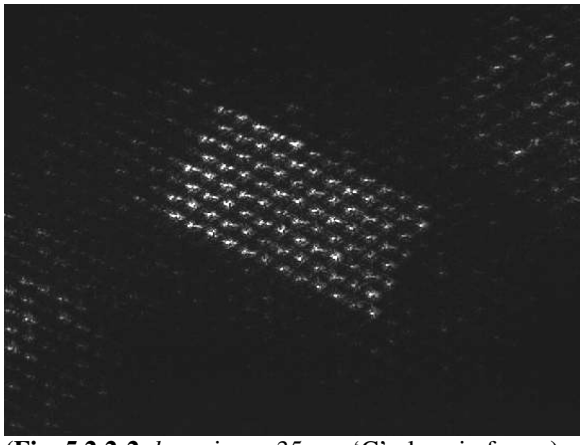

(Fig. 5.2.2-2 *d* spacing = 35 µm 'C' plane in focus.**)**

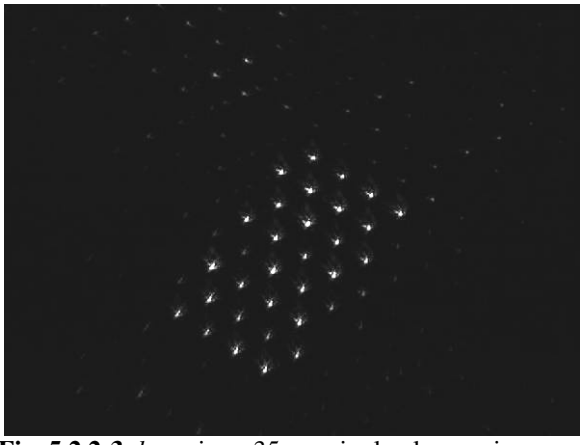

(Fig. 5.2.2-3 *d* spacing =35 µm single plane, primary image in focus.**)**

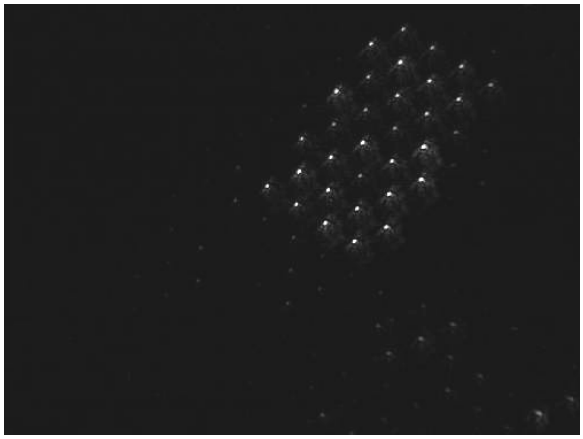

(Fig. 5.2.2-4 *d* spacing = 35 µm single plane, Conjugate image in focus.**)**

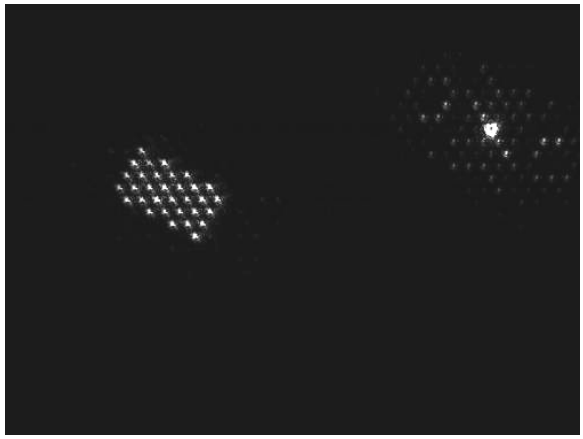

(Fig. 5.2.2-5 *d* spacing = 15 µm single plane**.)**

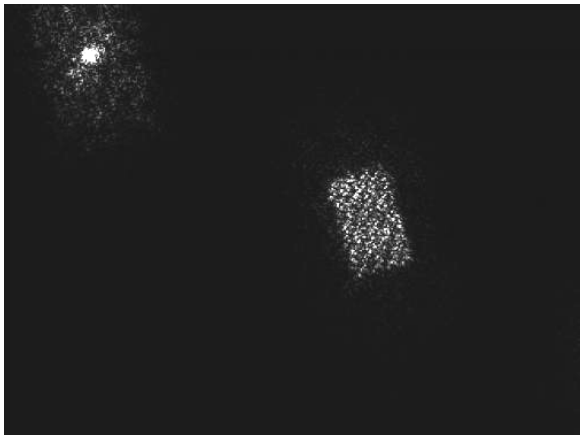

(Fig. 5.2.2-6 *d* spacing =15 µm 'ABC' plane**.)**

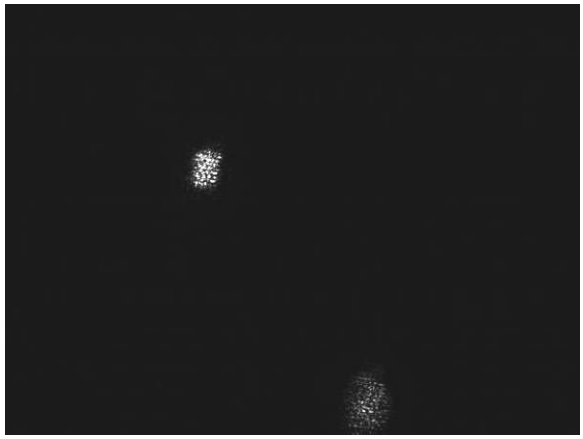

(Fig. 5.2.2-7 *d* spacing = 5 µm single plane**.)**

The point sources can clearly be distinguished when using a *d* value of 35 µm however; the intensity of each point varies. Figures 5.2.2-1 & 2 show 3D effects as individual planes are bought into focus. As expected, the 'ABC' images are less intense than the single plane

images and require large *d* values for each plane to be observed clearly. It is noticed that there is aberration present in each point, regardless of *d* spacing.

The digital camera can only just resolve the more closely spaced points in the Fig. 5.2.2-6 image. It appears that a speckle pattern is emerging in the light field, which is a characteristic of the random phase technique. The points in Fig. 5.2.2-7 cannot be resolved at all by the digital camera. Table 4 shows the specifications of the holograms created in this section.

Hologram specifications	
Array Size:	1024×1024
x,y starting position:	0.2 mm
Number of Points- 'A' Plane: 'ABC' Plane:	32 96
z distance:	50 mm
z increment: ('ABC' Plane only)	20 µm
Diffraction pattern clipped between: (full scale 0-1)	(0.2 – 0.75)
Printer used:	Ricoh Aficio 2060 PCL 6
Output quality:	1200 dpi
Graphics mode:	Vector

(**Table. 4** Hologram specifications for 'A' & 'ABC' plane holograms with reduced clipping.)

The above holograms were calculated using 20 mm as the desired output size for the finished holograms. Actual measurements showed the holographic film images to be 21.5 mm in width, probably due to a difference between the nominal and actual focal length of the camera lens (see chapter 4.2). This may partially explain the poor quality of the holograms as they were designed to be a different size to the actual size; however it is believed that the main reason for this poor quality lies with the printer/paper combination along with aberration in the converging lens. This decrease in quality is particularly evident in the 'ABC' type holograms. Rather than modify the photographic reduction set-up to correct the hologram size, the dimensions inside the code were modified to match the actual finished size.

5.2.3) Reduced Clipping – Comparison of Printers

Hologram specifications	
Array Size:	1024×1024
x,y starting position:	0.25 mm
Number of Points- 'A' Plane: 'ABC' Plane:	32 96
z distance:	50 mm
z increment: ('ABC' Plane only)	25 µm
Diffraction pattern clipped between: (full scale 0-1)	(0.2 – 0.75)
Printers used:	Ricoh Aficio 2060 PCL 6 Ricoh Aficio 1060
Output quality:	1200 dpi
Graphics mode:	Raster

(**Table. 5** Hologram specifications for 'A' & 'ABC' plane holograms with reduced clipping.)

Two different output printers (both black and white laser printers) were used to examine if there was any difference in the quality of the reconstructed holograms. The same settings were applied to each. The graphics mode was changed from Vector to Raster as this offered an increase in printout efficiency. In theory, there shouldn't be any difference between the two outputs but it was observed that the output tone and contrast of the diffraction patterns from each printer differed. It was decided to increase the *x, y* starting position to 0.25 mm to try to avoid stray light around the primary beam. Table 5 shows the hologram specifications for this section. The following images are all 1280×1024 pixels in size.

5.2.3a) Aficio 1060 Printer – Uniform Phase

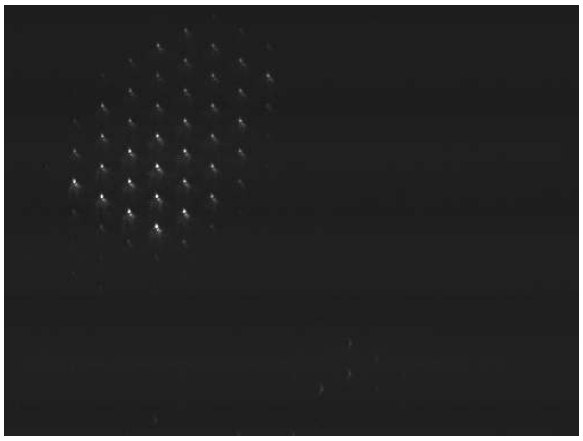

(Fig. 5.2.3a-1 *d* spacing = 35 µm single plane**.)**

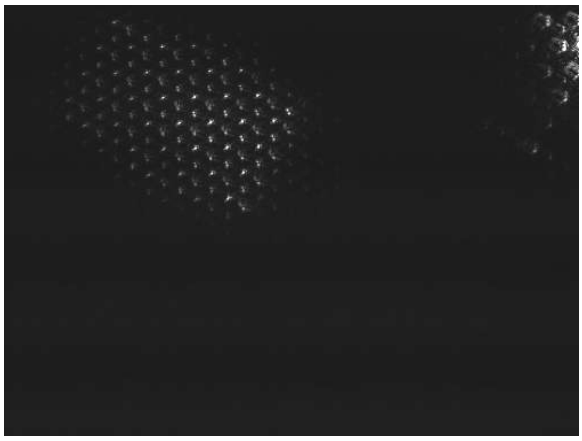

(Fig.5.2.3a-2 *d* spacing = 35 µm 'A' plane in focus.**)**

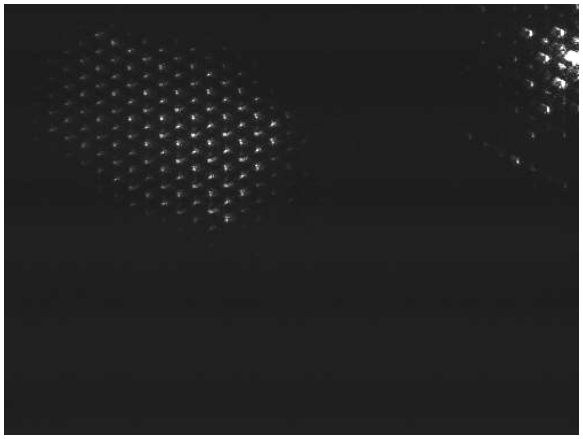

(Fig. 5.2.3a-3 *d* spacing = 35 µm 'B' plane in focus.**)**

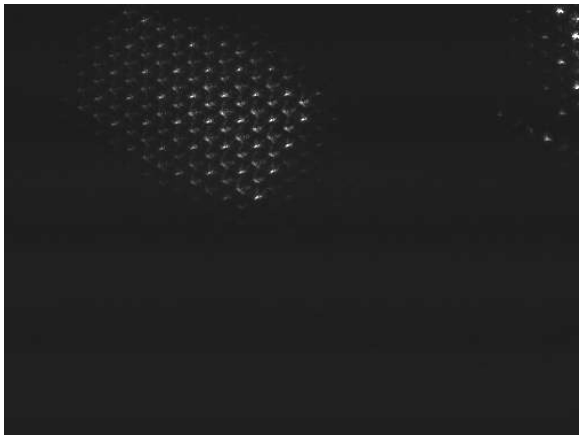

(Fig. 5.2.3a-4 *d* spacing = 35 µm 'C' plane in focus.**)**

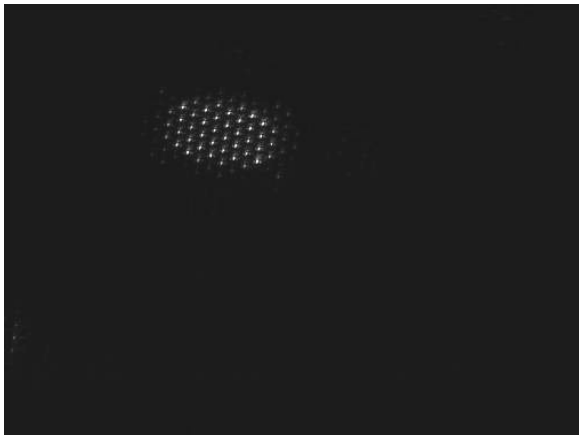

(Fig. 5.2.3a-5 *d* spacing = 15 µm single plane.**)**

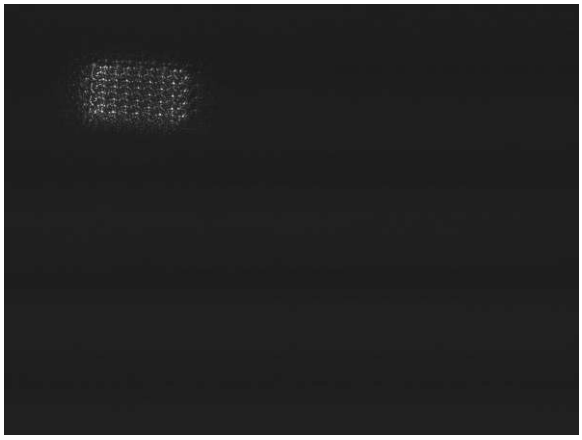

(Fig. 5.2.3a-6 *d* spacing = 15 µm 'A' plane in focus.**)**

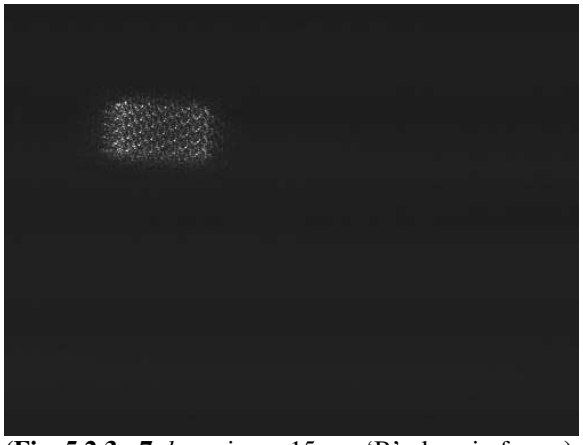

(Fig. 5.2.3a-7 *d* spacing = 15 µm 'B' plane in focus.**)**

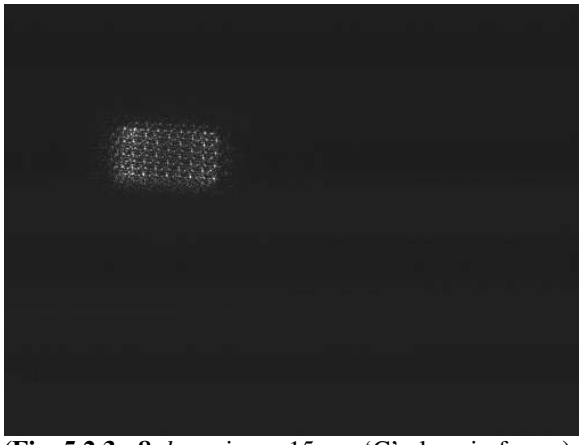

(Fig. 5.2.3a-8 *d* spacing = 15 µm 'C' plane in focus.**)**

5.2.3b) Aficio 1060 Printer – Random Phase

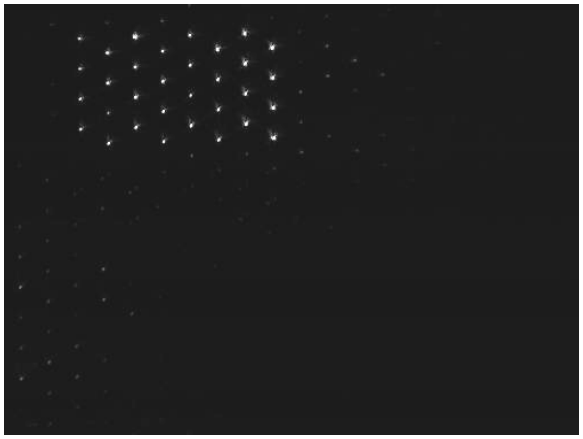

(Fig. 5.2.3b-1 *d* spacing = 35 µm 'A plane.**)**

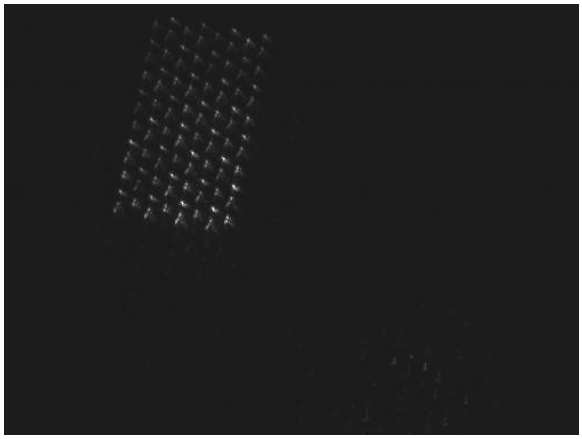

(Fig. 5.2.3b-2 *d* spacing = 35 µm 'A' plane in focus.**)**

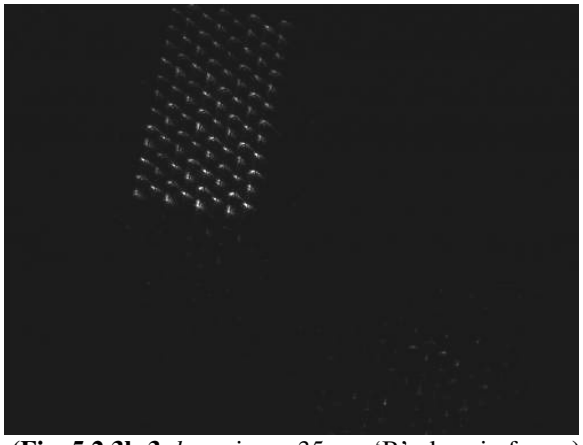

(Fig. 5.2.3b-3 *d* spacing = 35 µm 'B' plane in focus.**)**

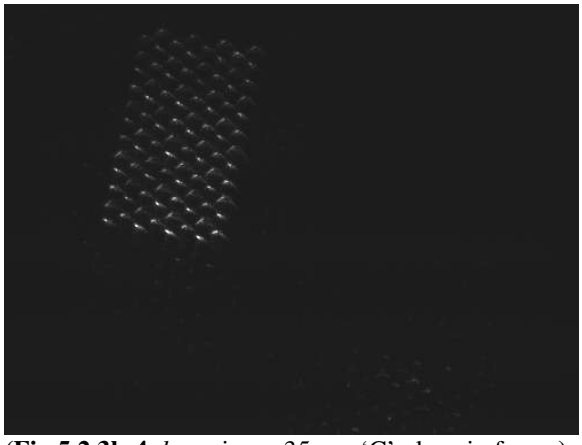

(Fig.5.2.3b-4 *d* spacing = 35 µm 'C' plane in focus.**)**

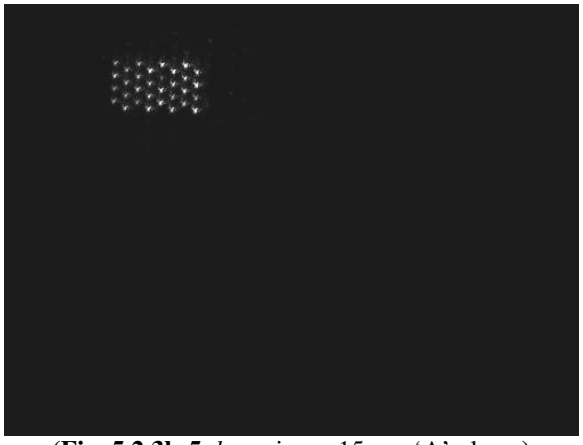

(Fig. 5.2.3b-5 *d* spacing = 15 µm 'A' plane.**)**

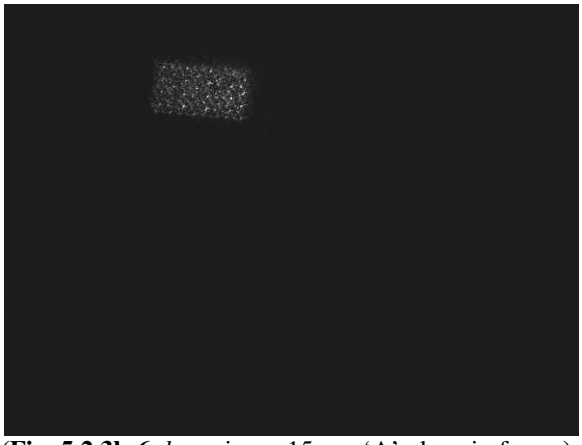

(Fig. 5.2.3b-6 *d* spacing = 15 µm 'A' plane in focus.**)**

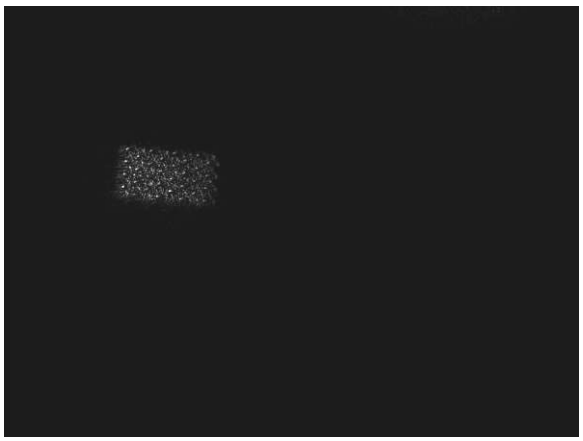

(Fig. 5.2.3b-7 *d* spacing = 15 µm 'B' plane in focus.**)**

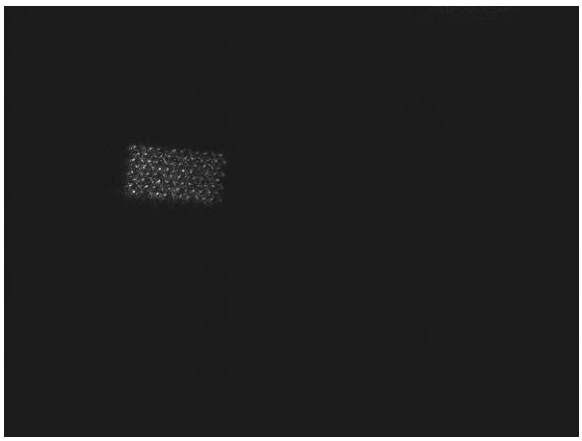

(Fig. 5.2.3b-8 *d* spacing = 15 µm 'C' plane in focus.**)**

5.2.3c) AFICIO 2060- Uniform & Random Phase

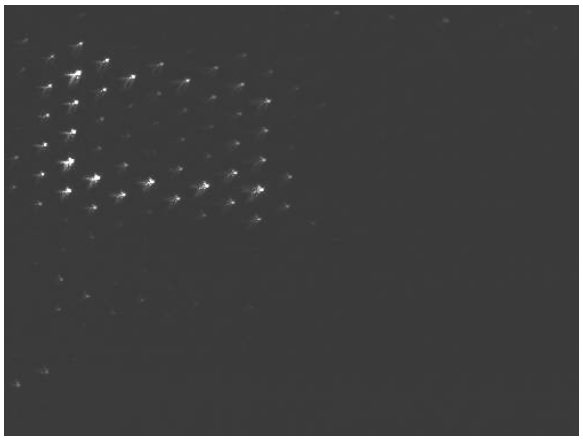

(Fig. 5.2.3c-1 *d* spacing = 35 µm 'A' plane**)**
(Uniform phase)

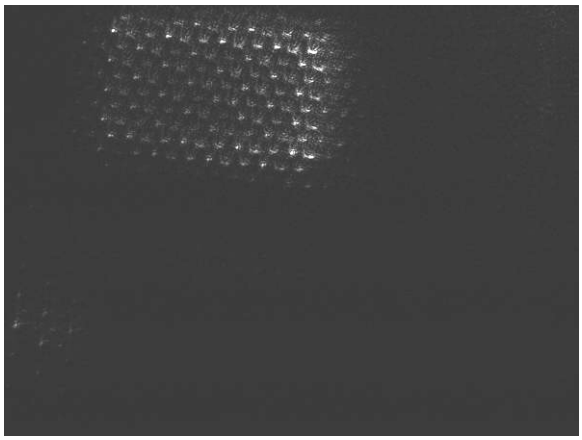

(Fig. 5.2.3c-2 *d* spacing = 35 µm ABC planes)
(Uniform phase**)**

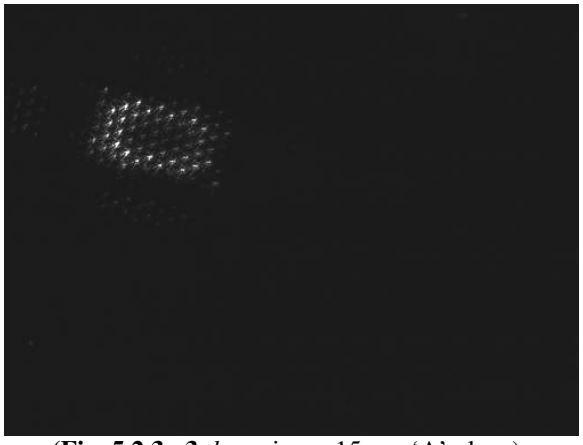

(Fig. 5.2.3c-3 *d* spacing = 15 µm 'A' plane)
(Uniform phase)

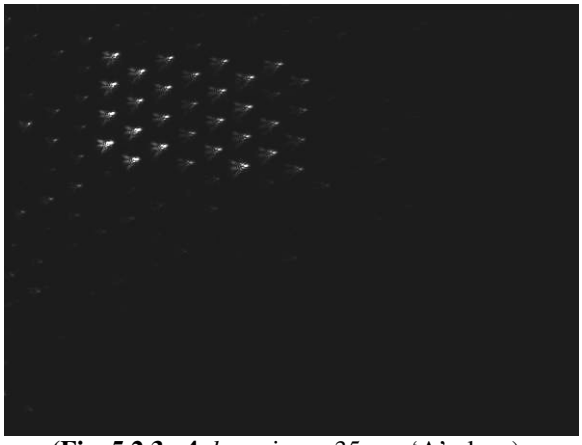

(Fig. 5.2.3c-4 *d* spacing = 35 µm 'A' plane)
(Random phase)

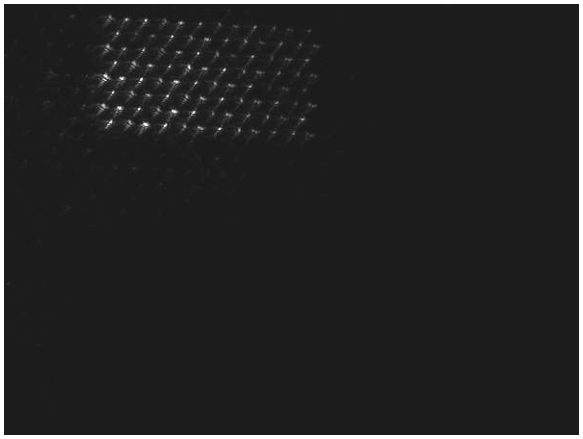

(Fig. 5.2.3c-5 *d* spacing = 35 µm ABC planes)
(Random phase)

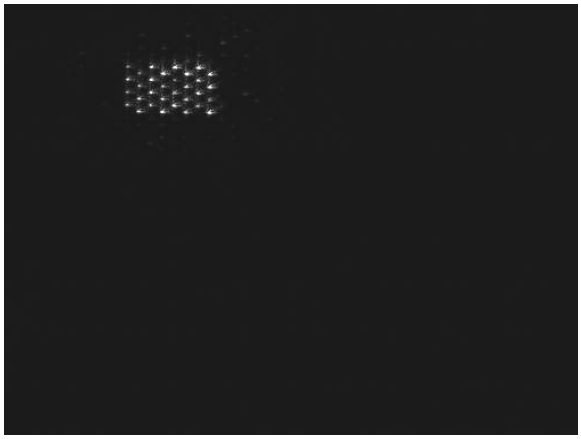

(Fig. 5.2.3c-6 *d* spacing = 15 µm 'A' plane)
(Random phase)

Moving the *x, y* starting position further from the optical axis tended to have a detrimental effect on the intensities of the points furthest from the centre for both uniform and random phase techniques. This is particularly evident in the 'ABC' holograms as evident in Fig. 5.2.3b-2 to Fig. 5.2.3b-4. This could be due to the fact that the distances of end point sources from the centre are close to the theoretical limits of the hologram.

It is noticed that the uniform phase holograms resulting from the output of the Aficio 2060 laser printer tended to be inferior to the ones resulting from the Aficio 1060 laser printer. This was initially surprising, since it was noticed that the Aficio 2060 tended to give a better output with increased tonality. However, due to the high-contrast nature of the film being used; the photographic output was of an inferior quality for the Aficio 2060, with areas on the film appearing to be over exposed. Thus, the quality of the associated holograms suffered as a result.

Examination under magnification of the printouts from both printers showed that there was a prominent half-tone pattern present, which tended to obscure the finer holographic fringes. As a result of these observations and tests, it was decided to try using an inkjet/photographic paper combination in an effort to improve results.

5.2.4) Light Clipping – Uniform & Random Phase

Hologram specifications	
Array Size:	1024×1024
x,y starting position:	0.2 mm
Number of Points- 'A' Plane: 'ABC' Plane:	32 96
z distance:	50 mm
z increment: ('ABC' Plane only)	25 µm
Diffraction pattern clipped between:	(0.15 – 0.8)
Printer/s used:	Epson Stylus PHOTO 1290 With Kodak Ultra premium A4 photo paper
Output quality:	2880 dpi
Graphics mode:	N/A

(**Table. 6** Hologram specifications for 'A' & 'ABC' plane holograms with light clipping)

To try and improve the quality of the printer and corresponding hologram output, a different printer was used. This was an Epson Stylus PHOTO 1290 A3 inkjet printer. By using premium quality photographic paper (265g/m^2) and the highest quality settings on the printer, it was hoped that this combination would give superior diffraction patterns which would subsequently lead to improvements in the associated holograms. The clipping was reduced in an attempt to improve the quality of the reconstructed hologram by decreasing power directed into higher diffraction orders and eliminating unwanted 'ghost' images. Table 6 shows the hologram specifications for this section. The above images were all captured using a 10x microscope objective lens to magnify the holographic image. However, since the numerical aperture of this lens was less than that of the 50 mm camera lens, loss of resolution could occur in the imaging plane. Therefore, a 40x lens was substituted to provide superior images. This is not important as far as trapping is concerned, since trapping will occur *before* the magnification stage. The following images are captured using the 40x lens and makes use of

the display set up shown in Fig. 4.3b. It was noticed that limitations of the film (i.e. nonuniformity in thickness of the film) affected the quality of the generated holographic image. The following images (Figs. 5.2.4-1a & b) show two cases of the primary beam with and without a piece of clear negative film inserted into the system. Figure 5.2.4-1b clearly shows the distortions in the primary beam as a result of it suffering phase distortions on passing through the film substrate.

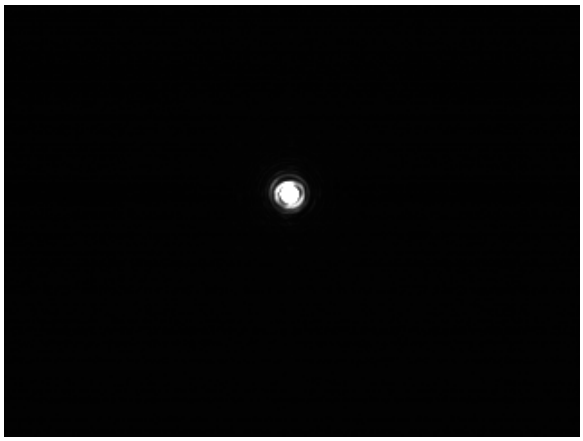

(Fig. 5.2.4-1a Primary beam**)**

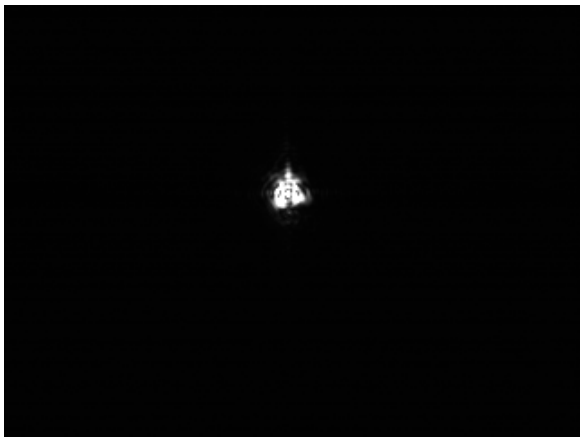

(Fig. 5.2.4-1b Primary beam passing through clear Kodalith negative film.**)**

To compensate for the unevenness in the film thickness, a reduced area of the hologram was illuminated with the laser. While this resulted in a fainter image (as expected), the point sources were more sharply defined and there were fewer ghost traps and interference effects present. The following images are 1280×1024 pixels:

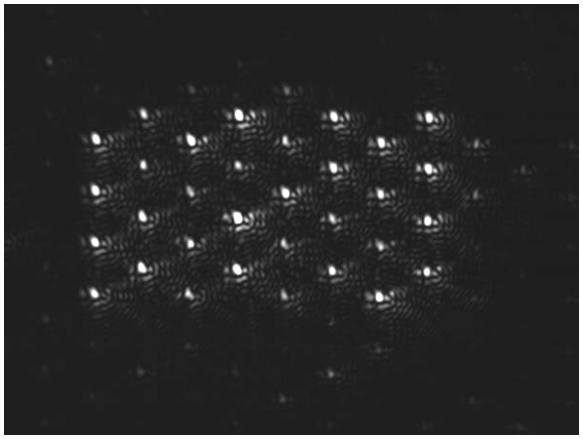

(Fig. 5.2.4-2a *d* spacing = 15 µm 'A' plane random with large aperture, exposure =90ms.)

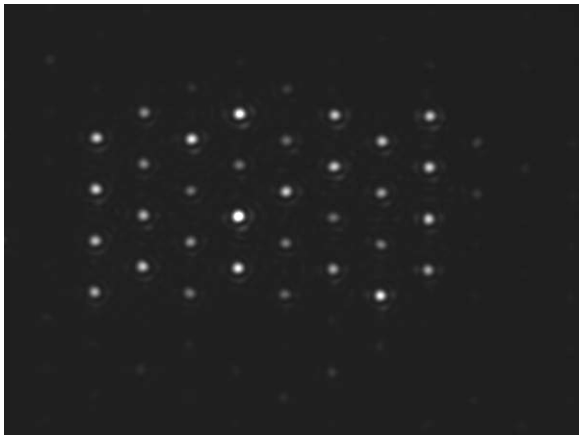

(Fig. 5.24-2b *d* spacing = 15 µm, single plane random with small aperture, exposure = 90ms**.)**

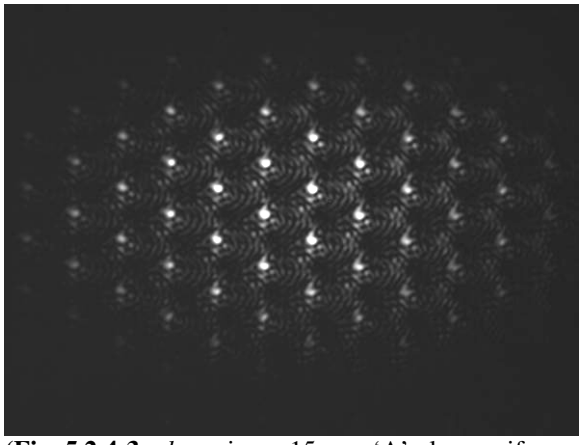

(Fig. 5.2.4-3a *d* spacing = 15 µm, 'A' plane uniform phase with large aperture, exposure = 300ms.)

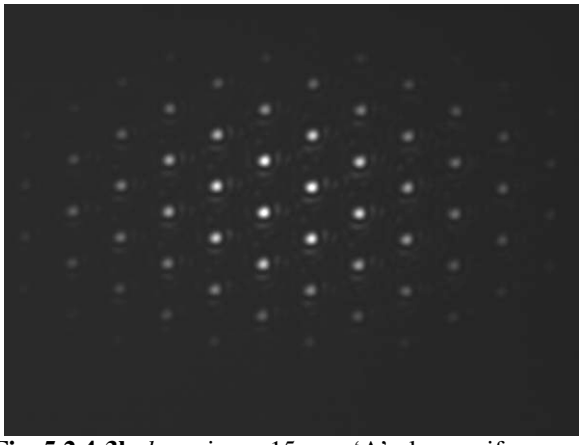

(Fig. 5.2.4-3b *d* spacing = 15µ m, 'A' plane uniform phase with small aperture, exposure = 300 ms.)

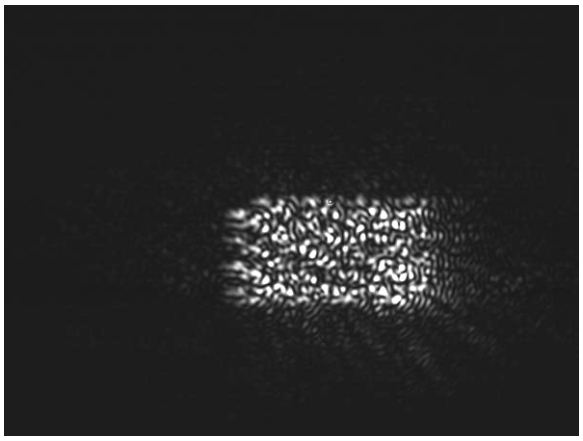

(Fig. 5.2.4-4a *d* spacing = 7.5 µm, 'A' plane random phase with large aperture, exposure = 60ms.)

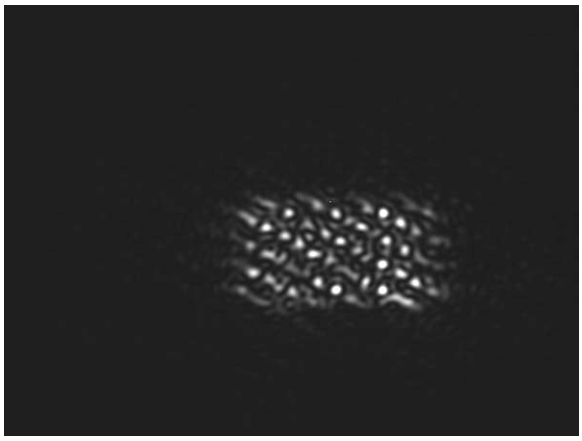

(Fig. 5.2.4-4b *d* spacing = 7.5 µm, 'A' plane random phase with small aperture, exposure = 60ms.**)**

The following images are 640×480 pixels:

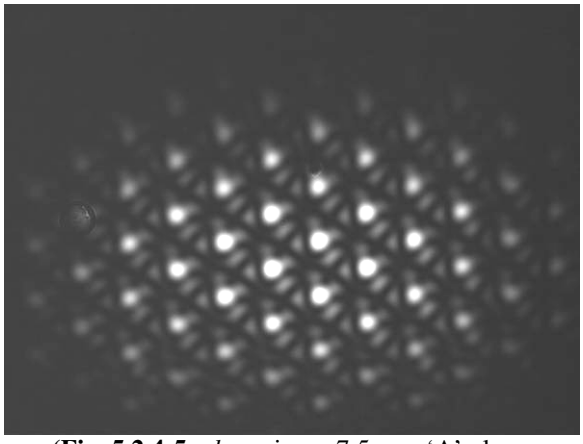

(Fig. 5.2.4-5a *d* spacing = 7.5 µm, 'A' plane uniform phase with large aperture, exposure = 180ms.)

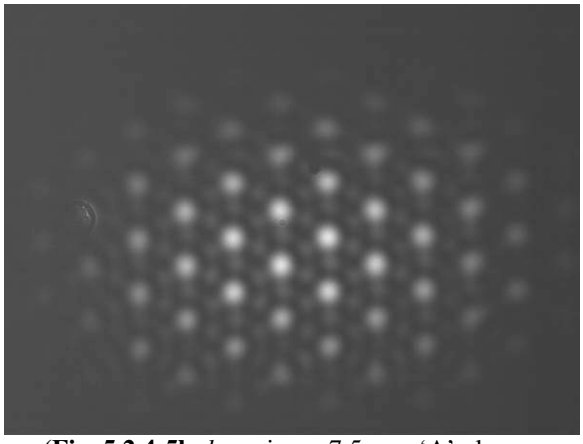

(Fig. 5.2.4-5b *d* spacing = 7.5 µm, 'A' plane uniform phase with small aperture, exposure = 202ms.**)**

The following images are 320×240 pixels:

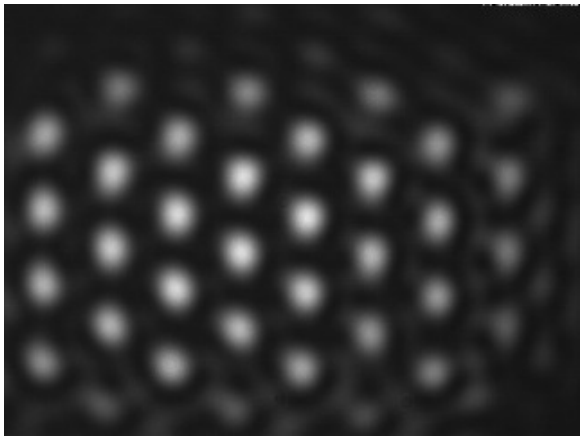

(**Fig. 5.2.4-6a** *d* spacing = 5 µm, 'A' plane uniform phase with small aperture, exposure = 180ms.)

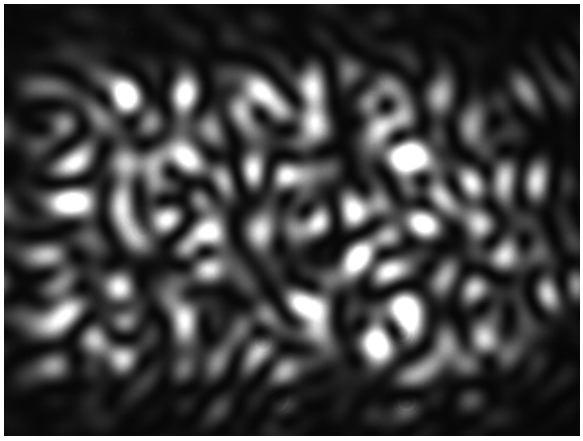

Fig. 5.2.4-6b *d* spacing = 5 µm, 'A' plane random with small aperture, exposure = 37.5ms.)

As can be seen from the above images' exposure times, the random phase technique produces a more efficient hologram in terms of diffraction; however it cannot accurately reconstruct the pattern for low *d* values. Using a small aperture, the technique is just able to resolve individual points at a *d* spacing of 7.5 µm (Fig. 5.2.4-4b); however it cannot resolve points lower than this as evident in Fig. 5.2.4-6b. Therefore, this technique is not suitable for creating holographic optical traps as traps typically require low *d* values, but is suitable for *d* values of 10 µm and above due to the higher diffraction efficiency. The uniform phase technique is therefore more suited to designing traps with low *d* values in spite of the decrease in efficiency compared to the random phase method.

Of course, reduction in the illuminated area of the hologram has the same effect as using a reduced numerical aperture – it increases the minimum size and separation of image points, and so reduces trapping efficiency. This trade-off has to be kept in mind.

5.3) Spherical Aberration Results

In addition to the limitations of the film, the 50 mm camera lens imposes spherical aberrations which further degrade the reconstructed image. These aberrations are particularly evident in the outer zones of the lens where phase deviations from the ideal are quite significant. Several tests were undertaken to measure these aberrations and to determine the amount of compensation required in the *lensph* function to overcome this (see Chapter 4.4). Three different situations were photographed with the setup in Fig. 4.4; these being with the pinhole

of the spatial filter positioned at the focal point of the centre of the lens, with the lens-pinhole distance changed to give approximately 6 interference fringes of focus error, and with about 12 fringes of defocus present. Figures 5.3a–c show these three types of fringe images.

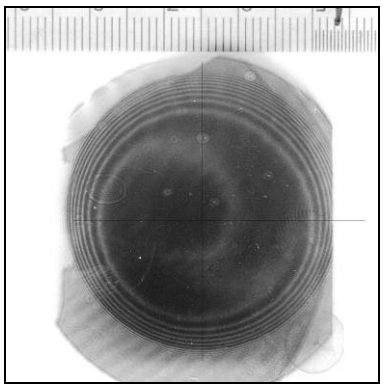

(Fig. 5.3a focal point at centre.**)**

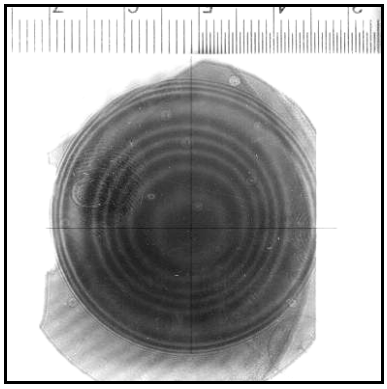

(Fig. 5.3b 6 fringe defocus.**)**

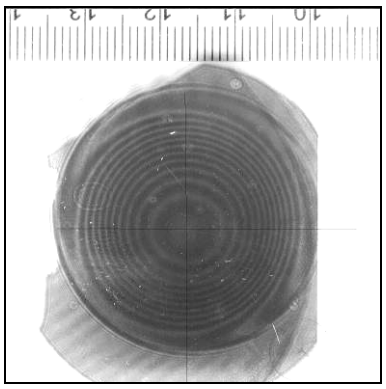

(Fig. 5.3c 12 fringe defocus.**)**

The film was placed into a scanner and the position of the fringes from the resulting images could be accurately plotted. From this data, a graph showing fringe number versus position could be obtained (see Appendix B for the associated graphs). A suitable equation was determined from this data, using the Solver function in MS Excel, to use in compensating for the aberrations present. The equation used to obtain a fit to the data is of the form:

$$m_f = A + Br_s + Cr_s^2 + Er_s^4 + Fr_s^6 \qquad \textbf{Eq. 5.3a}$$

where m_f is the predicted fringe order, A is the baseline coefficient, B is a tilt factor coefficient, C is a 2nd order coefficient expressing departure from ideal focus, and E and F are 4th and 6th order coefficients which are spherical aberration terms. The variable $r_s = r/r_0$ is the normalised radius from the centre of the lens, where r_0 =15 mm. The various calculated coefficients are shown in Table 7. Two determinations are made from each of the three recordings, one across a horizontal axis and one across a vertical axis. The best-fit position of the centre of the lens was also determined in the fitting procedure.

		Mult Hor	Mult Ver	Min Hor	Min Ver	Zero Hor	Zero Ver
	Rad	15	15	15	15	15	15
centre	x0	24.346	28.385	24.197	28.227	26.345	27.177
baseline	A	-0.166	0.024	-0.496	-0.483	0.097	-0.421
tilt	B	1.036	-0.681	0.242	-0.143	-0.378	0.718
2nd	C	10.625	10.368	4.509	5.278	-0.099	2.168
4th	E	7.492	6.801	7.981	5.784	3.483	0.171
6th	F	-6.781	-6.426	-6.706	-5.598	-4.606	-3.349
	error	0.2395	0.536	0.2095	0.619	0.031	0.3216

(**Table. 7** Fringe measurement data)

Equation 5.3a gives the calculated phase variation in terms of orders of interference, not optical path (in mm). It is converted into an optical path variation Λ_f by multiplying by the wavelength λ. The optical path change Λ_f just due to the aberration terms is thus:

$$\Lambda_f = m_f \lambda = \lambda E\left(\frac{r}{r_o}\right)^4 + \lambda F\left(\frac{r}{r_o}\right)^6 \qquad \textbf{Eq. 5.3b}$$

where r_0 =15 mm. The coefficients E and F are the average taken from the first three fitted E & F values in Table 7. These coefficients are then substituted into Eq. 5.3b to find the corresponding a and b coefficients in the *lensphcorr* function. Therefore $\frac{\lambda E}{r_o^4}$ corresponds to coefficient a, with $\frac{\lambda F}{r_o^6}$ corresponding to b. The r value in Eq.5.3b is the same as the r_1 value in Eq. a4 and the *lensphcorr* function (refer to Appendix A.1). The value for a (-7.86×10^{-8}) is made negative and b (3.046×10^{-10}) is made positive to apply the desired compensation.

The *lensphcorr* function is used in conjunction with the *spheric* and *sphericrand* functions when generating the holographic diffraction patterns.

5.3.1) Lens Compensation Results

Hologram specifications	
Array Size:	1024×1024
x,y starting position:	0.2 mm
Number of Points- 'A' Plane: 'ABC' Plane:	1, 4, 32, 50 N/A
z distance:	50 mm
z increment: ('ABC' Plane only)	25 µm
Diffraction pattern clipped between:	(0.15 – 0.8)
Printer/s used:	Epson Stylus PHOTO 1290 With Kodak Ultra premium A4 photo paper
Output quality:	2880 dpi
Graphics mode:	N/A

(**Table. 8** Specifications for holograms with compensated lens function.)

The following images show different point source configurations generated with and without the modified lens function. These images were taken using the setup (Fig. 4.5a) in chapter 4.5. The efficiency in this setup is evident in the decreased exposure times of the images compared to previous display setups. A 10x microscope lens was used to magnify the images except where noted. For ease of hologram image identification, a numbering system was introduced. Table 8 shows the different hologram specifications for this section. Table 9 gives a description of each holographic image:

Hologram Number:	Type & number of points:	*(x,y)* co-ordinates:	*d* spacing	Phase type:
HOLO 1	Corrected. 1 point.	(0.4,0.4) mm		Uniform
HOLO 2	Uncorrected. 1 point.	(0.4,0.4) mm		Uniform
HOLO 3	Corrected. 4 points.	(0.3,03) mm and separation of 50 µm.		Uniform
HOLO 4	Uncorrected. 4 points	(0.3,03) mm and separation of 50 µm.		Uniform
HOLO 5	Corrected. 'A' Plane, 50 points.	(0.2,0.2) mm	5 µm	Uniform
HOLO 6	Corrected. 'A' Plane, 32 points.	(0.2,0.2)mm	15 µm	Uniform
HOLO 7	Corrected. 'A' Plane, 32 points.	(0.2,0.2) mm	10 µm	Random
HOLO 8	Corrected. 1 point.	(0.4,0.4) mm		Random
HOLO 9	Corrected. 'A' Plane, 32 points.	(0.2,0.2) mm	5 µm	Random
HOLO 10	Uncorrected. 4 points	(0.3,03) mm and separation of 50 µm.		Random
HOLO 11	Corrected. 4 points.	(0.3,03) mm and separation of 50 µm.		Random
HOLO 12	Corrected. 'ABC' Planes, 96 points.	(0.2,0.2) mm, Plane spacing = 30 µm	15 µm	Uniform
HOLO 13	Corrected. 'A' Plane, 32 points.	(0.2,0.2) mm	7.5 µm	Uniform
HOLO 14	Corrected. 'A' Plane, 72 points.	(0.2,0.2) mm	15 µm	Uniform
HOLO 15	Corrected. 'A' Plane, 32 points.	(0.2,0.2) mm	7.5 µm	Random

(**Table. 9** Hologram image identification.)

5.3.1a) Uniform Phase

The following images are 1280×1024 pixels and were captured with a 10x objective. The aperture settings refer to the portion of the beam which illuminated the hologram.

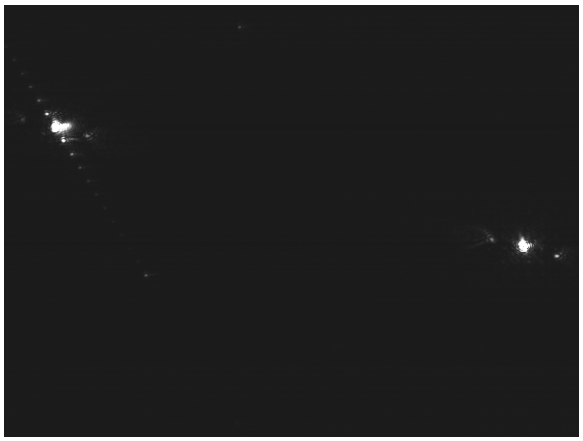

(**Fig. 5.3.1a-1a** HOLO 1, 1/3 aperture.)

(**Fig. 5.3.1a-1b** HOLO 1, 1/4 aperture.)

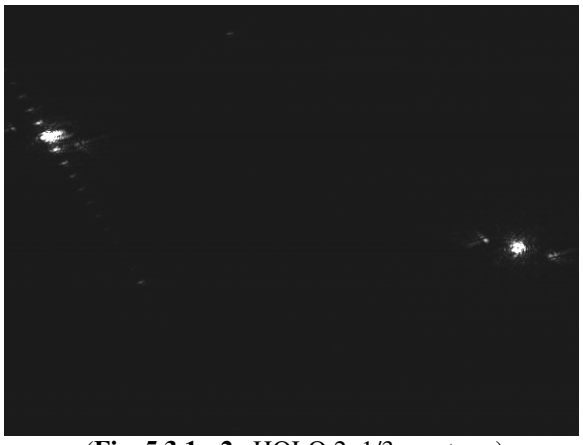

(**Fig. 5.3.1a-2a** HOLO 2, 1/3 aperture.)

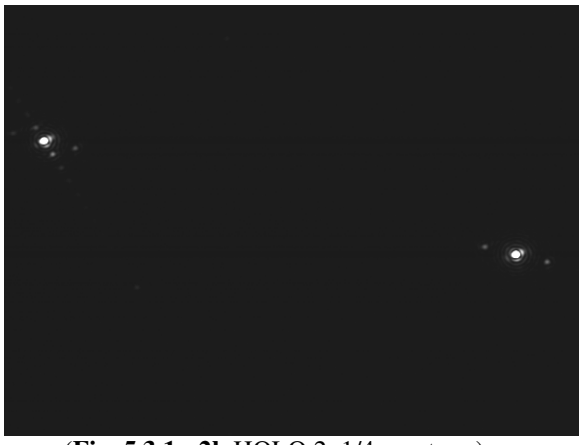

(**Fig. 5.3.1a-2b** HOLO 2, 1/4 aperture.)

(Fig. 5.3.1a-3a HOLO 3, full aperture.**)**

(Fig. 5.3.1a-3b HOLO 3, 1/3 aperture.**)**

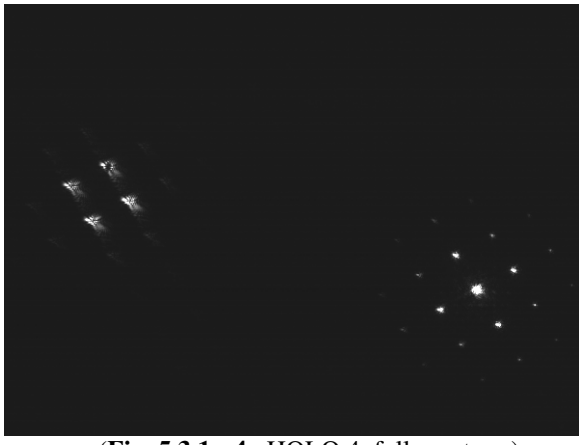

(**Fig. 5.3.1a-4a** HOLO 4, full aperture.)

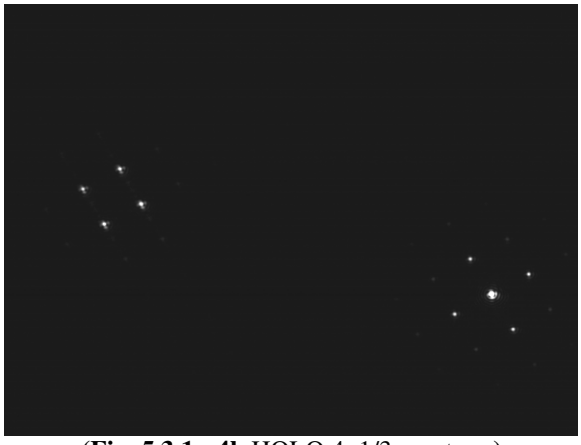

(Fig. 5.3.1a-4b HOLO 4, 1/3 aperture.**)**

The following images are 320×240 pixels:

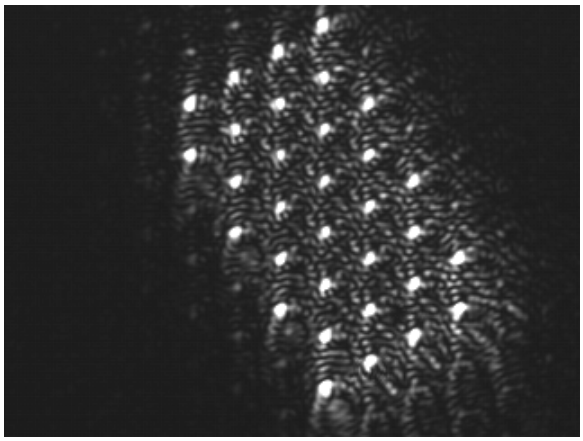

(Fig. 5.3.1a-5a HOLO 6, full aperture.**)**

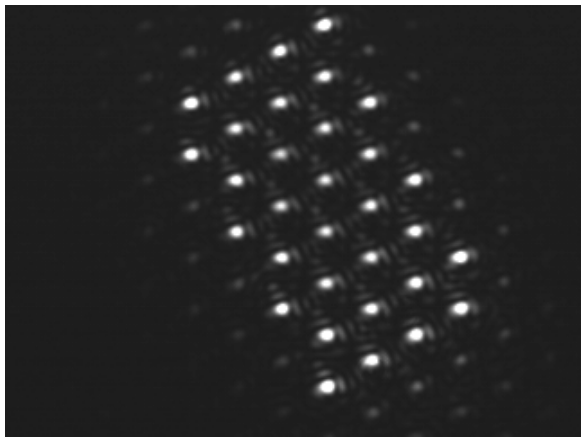

(Fig. 5.3.1a-5b. HOLO 6, 1/3 aperture.)

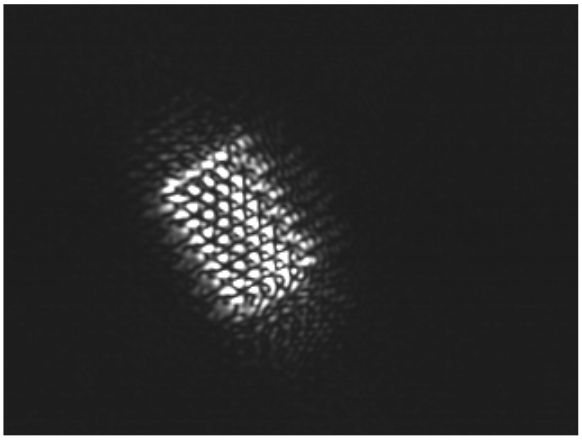

(Fig. 5.3.1a-6. HOLO 5, full aperture.**)**

5.3.1b) Random Phase

The following images are 1280×1024 pixels and a 40x lens was used in the capture of the two images:

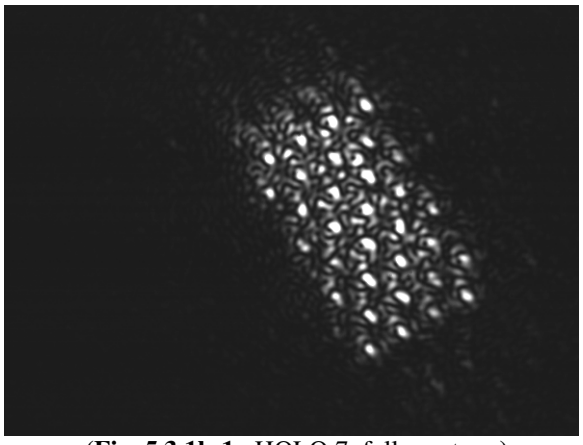

(Fig. 5.3.1b-1a HOLO 7, full aperture.**)**

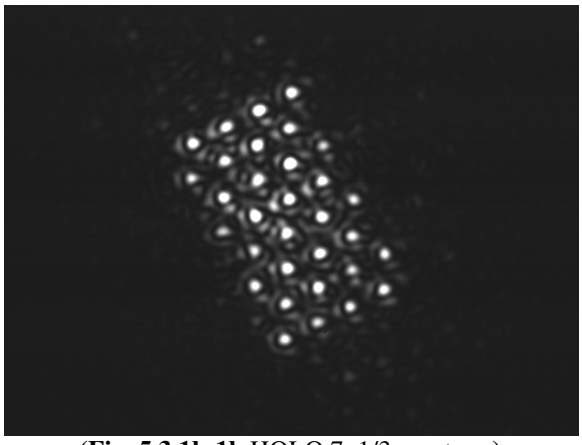

(Fig. 5.3.1b-1b HOLO 7, 1/3 aperture.**)**

The following images were taken with a 10x objective and are 320×240 pixels:

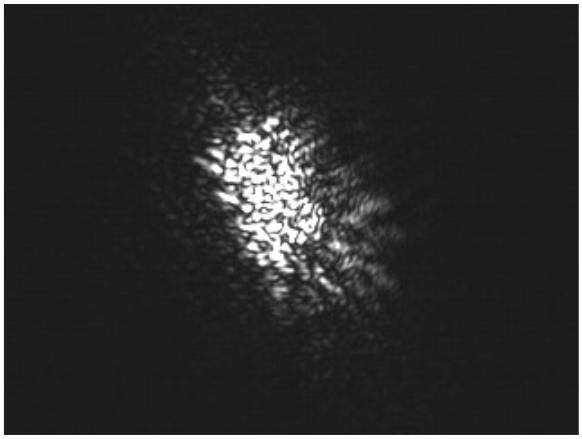

(Fig. 5.3.1b-2a HOLO 9, full aperture.**)**

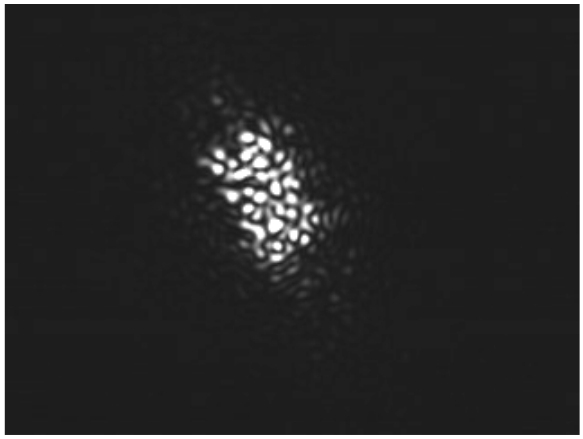

(Fig. 5.3.1b-2b HOLO 9, 1/3 aperture.**)**

There seems to be an improvement in the quality of the holograms employing the corrected lens function over the previous holograms. This is especially evident in the uniform phase 15 µm and 5 µm types as the 'A' plane structure is more defined (Fig. 5.3.1a-5a & b and Fig. 5.3.1a-6) compared to previous images (Figs. 5.2.4- 2a – 3b). Although there appears to be a slight increase in the efficiency of the random phase method in conjunction with the corrected lens function, individual point sources cannot be adequately resolved at lower *d* values (Fig. 5.3.1b-2a & b) again suggesting that this method is only suitable for higher *d* value light fields. However, it should be noted that the lens aberration correction is not expected to make

much difference in the quality of holograms viewed with a small aperture since the correction mainly comes into effect at the outer zones of the lens.

5.3.2 Index-Matching

The photographic film was sandwiched between two microscope slides to improve overall uniformity of the film thickness. Microscope oil (Corgille immersion oil type B – lot # 062175) was used to index-match on both sides of the film. The purpose of this was to try to minimise the effects of phase irregularities across the film surface. It was important to ensure that the glass slides were cleaned before use as any smudging of the surface led to distortions in the reconstructed holograms. The images of Fig. 5.3.2 were taken with index-matching. A 10x microscope lens was used to magnify the images.

5.3.2a) Uniform Phase

The following images are 640x480 pixels:

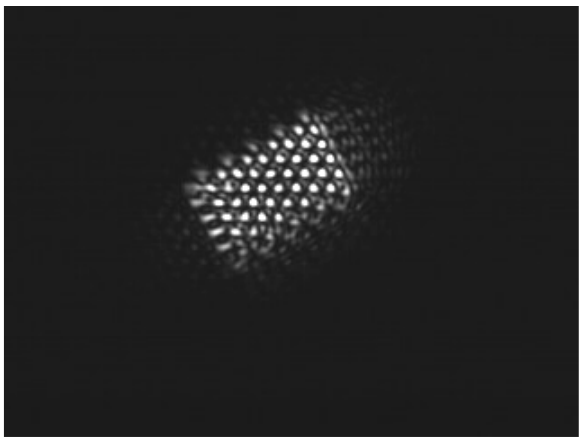

(Fig. 5.3.2a-1a HOLO 5 full aperture; exp = 0.2ms.**)**

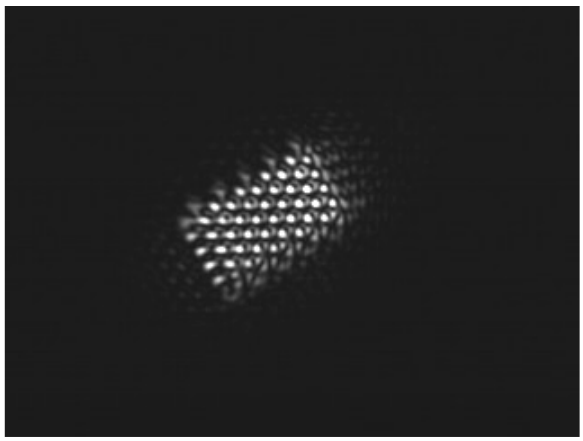

(Fig. 5.3.2a-1b HOLO 5 1/2 aperture; exp = 0.2ms.**)**

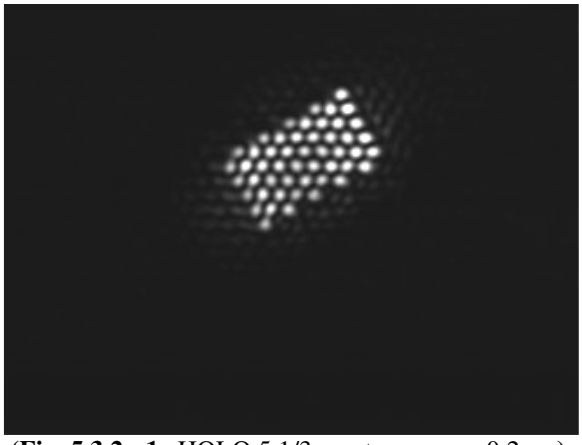

(Fig. 5.3.2a-1c HOLO 5 1/3 aperture, exp = 0.2ms.**)**

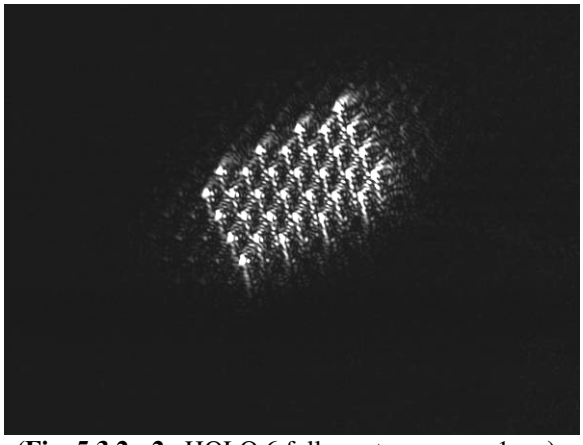

(Fig. 5.3.2a-2a HOLO 6 full aperture, exp = 1ms.**)**

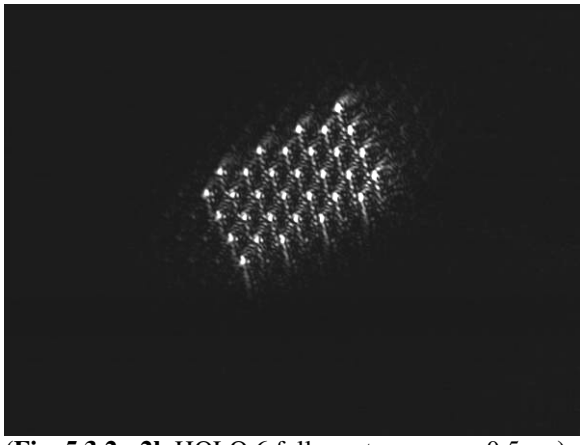

(Fig. 5.3.2a-2b HOLO 6 full aperture, exp = 0.5ms.)

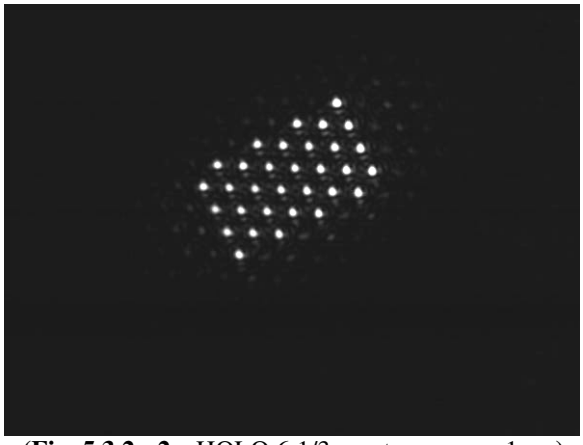

(Fig. 5.3.2a-2c. HOLO 6 1/3 aperture, exp = 1ms.)

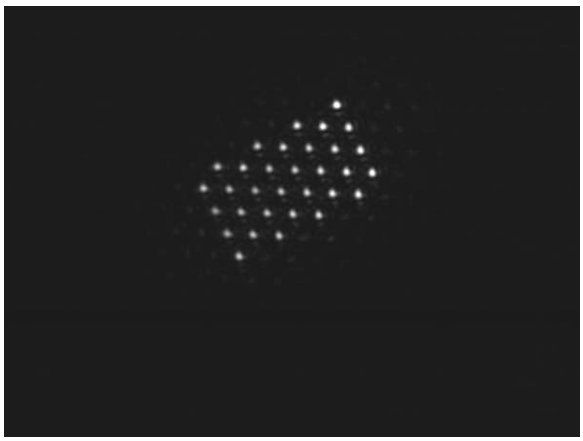

(Fig. 5.3.2a-2d HOLO 6 1/3 aperture, exp = 0.5ms.)

(Fig. 5.3.2a-3 HOLO 3 1/3 aperture, exp = 0.2ms**.)**

5.3.2b) Random Phase

The laser was set to 70 mW for the following images which are 640×480 pixels:

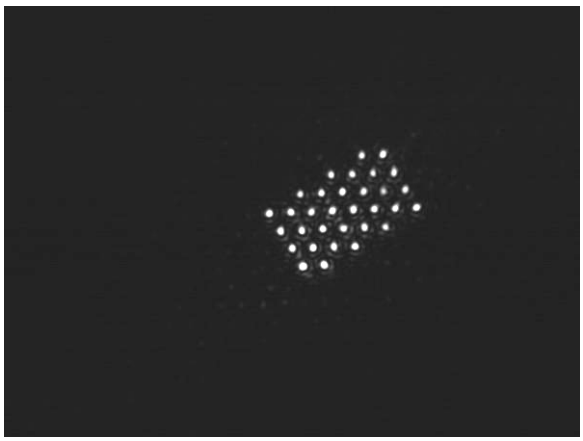

(**Fig. 5.3.2b-1a** HOLO 7 1/3 aperture, exp = 16ms.)

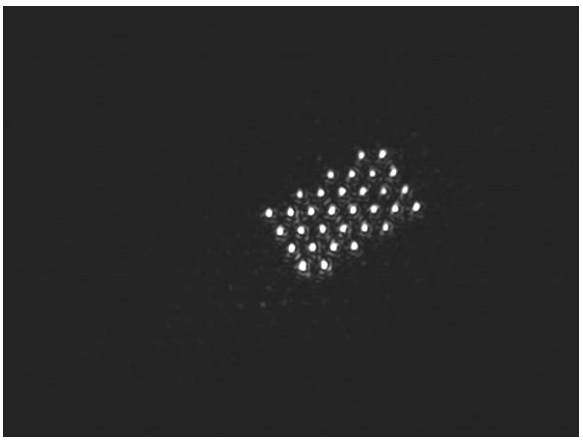

(**Fig. 5.3.2b-1b** HOLO 7 1/2 aperture, exp = 16ms.)

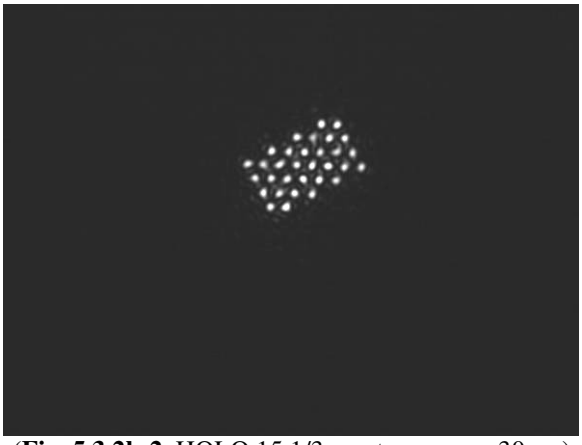

(**Fig. 5.3.2b-2.** HOLO 15 1/3 aperture, exp = 30ms.)

It is quite clear from the above random phase images that index matching has resulted in an improvement in the quality of the reproduced holograms. Individual points can quite easily be distinguished in both the 10 and 7.5 µm *d* spacing fields. However the intensities of the individual point sources are not uniform.

The above random phase images have a higher camera exposure time compared to the uniform phase images due to the fact that different laser line blocking filters were used. A stronger blocking filter, optimised for 514.5 nm and taken from laser safety glasses replaced the previous filter. This was deemed necessary to protect the camera as trapping experiments would require higher power than what was previously used in hologram reconstructions.

Summary

Overall, the index matching technique coupled with lens compensation methods has proved a success with the quality of the reconstructed holograms being superior to previous efforts. This should produce suitable light fields for two-dimensional trapping. Three-dimensional 'ABC' type holograms have successfully been generated and 3D effects have been observed; however, despite this, proper three-dimensional trapping with an 'ABC' type hologram is unlikely to be unattainable with the techniques developed here due to the complex nature of the patterns and the high *d* and *z* spacings required in resolving 3D effects. Other problems associated with this type of hologram include the fact that, for multiple planes, light from one plane will tend to interfere with light from other planes unless the individual traps are widely separated. Also, the diffraction patterns generated tend to be highly complex with extremely

fine fringe detail and the film has difficulty in reproducing this. Therefore, a useful, static multi plane light field will be extremely difficult to achieve in practice using these methods.

5.4) Power Measurements in Traps

To determine the beam power transmittance at various stages throughout the system, a series of measurements were taken using a silicon photodiode detector (United Detector Technology model 10DP) with associated multimeter to record the current. These measurements were taken after the 4x objective lens was introduced into the spatial filter arrangement (Fig. 4.5a) as previous systems had losses in the order of 94% [81, 82] without any holograms in place. The photodiode detector behaves in a linear fashion up to a maximum output of 10 mA, after which the detector becomes swamped. A neutral density filter was placed in front of the detector to reduce its output current to less than this. Various measurements were taken at the sample stage with and without various holograms in place and the results are displayed in Table 10.

Power Transmittance Measurements Throughout Optical System		
Stage	Current (in mA)	Percentage transmittance (%): (compared to initial beam)
Initial beam :	8.63	100
Sample stage with large aperture & hologram holder in place:	3.51	41
Sample stage with large aperture, hologram holder and 2 clear glass slides:	3.07	36
Sample stage with large aperture, hologram holder and hologram slide (Holo 3):	0.51	6.8
Sample stage with half-covered aperture, hologram holder and hologram slide (Holo 3):	0.32	3.7
Sample stage with large aperture, hologram holder and hologram slide (Holo 5):	0.29	3.4
Sample stage with large aperture, hologram holder and hologram slide (Holo 6):	0.39	4.6

(Table 10: Transmittance measurements throughout the optical system.**)**

HOLO's 5 & 6 are two different holograms with slightly different exposures. Even though the camera and lighting settings were the same for both; the differing diffraction pattern print outs affect the final overall density of the film. With the variable aperture open fully and with the hologram holder in place, the available beam power at the hologram plane is 41% of the laser output. It is noticed that adding the hologram to the optical system significantly increases the

power loss in the system so that only a few percent of the original power is available for trapping.

Although it is difficult to measure the power in each trap directly, some estimates can be made. For example; using the HOLO 3/half aperture measurement and taking an initial beam power of 1.35 W would result in approximately 50 mW remaining in the total beam after passing through the hologram. The primary spot (or zero order) in the resulting image would account for at least half of this power, leaving 20–25 mW to be spread over the eight traps (conjugate traps have to be included even though they will not be in focus). This suggests a range of 2.5–3 mW per trap. However the true figure will definitely be lower since higher orders have been ignored (but are present) and smaller, less intense 'ghost' traps are known to be present. These 'ghost' traps can be seen around the four primary traps in images concerning HOLO 3 and they detract from the overall intensity of the primary traps.

Due to their greater diffraction efficiency, random phase type holograms with multiple point sources offered the greatest chance of success in trapping multiple particles compared to the equivalent normal phase types. HOLO 7 was used to successfully trap multiple polystyrene particles and its associated power measurements are shown in Table 11:

HOLO 7 Power Transmittance Measurements		
Stage:	Current (in mA)	Percentage transmittance % (compared to initial beam)
Initial beam:	8.62mA	100
Sample stage with large aperture, hologram holder and hologram slide (Holo 7):	2.17	25
Sample stage with half-covered aperture, hologram holder and hologram slide (Holo 7):	1.38	16
Sample stage with two-thirds-covered aperture, hologram holder and hologram slide (Holo 7):	0.76	8.8

(**Table. 11** Power Transmittance for HOLO 7.)

As seen in Table 11, the beam power lost while passing through the hologram slide is significantly (~4 times) less than the HOLO 3 results. However, HOLO 7 will be made up of 64 primary and conjugate traps plus ghost and higher orders. Thus having multiple, individual traps with enough intensity for trapping will require significantly more efficient holograms. This is something that the uniform phase method cannot achieve.

5.4.1) Determination of Power in Individual Traps

To gain a better understanding of the trapping power associated with different light fields, a series of beam power calibration and responsivity measurements were undertaken. The Argon-ion laser was set to 300 mW beam power, with a variable density filter placed in front of the beam, which was then passed through a beam expander to provide an area of uniform irradiance across the beam. An International Light SpectrILight spectroradiometer (ILT-900) with an absolute irradiance calibration was used to record the spectral irradiance at this point. An integration of the spectral irradiance across the peak (from 510–520 nm) was undertaken, giving an integrated irradiance of 24.8 μW cm^{-2}.

As a check, a lux meter (Hagner EC1) was used to measure the illuminance of the beam at the same point, resulting in a reading of 95 lux (lm m^{-2}). The luminous efficacy at 515 nm is 408 lm W^{-1}, therefore the lux meter reading corresponded to an irradiance of 23 μW cm^{-2}, in good agreement with the SpectrILight measurement. An image of the same beam profile was captured using the Mightex digital camera at 1 ms exposure time and, along with a background exposure (i.e. beam blocked off) was analysed using the *ImageJ* software. Each pixel in the Mightex camera records intensity in 256 levels (or counts) from 0-255. Therefore anything higher than this level results in overexposure but still is recorded at 255. The *ImageJ* software can analyze images captured and give a record of the number of counts per pixel. It can also analyze a particular selected area in the image which is useful when looking at images of traps.

Analysing the above exposures resulted in a mean count per pixel of 93 counts at 1 ms after subtraction of background. From our calibration results, this corresponds to an irradiance of 0.2485 W m^{-2}. Therefore 1 count corresponds to:

$$\frac{0.248\ \mathrm{W\ m^{-2}}}{93} = 2.67 \times 10^{-3}\ \mathrm{W\ m^{-2}}\ \text{at 1 ms.}$$

Each pixel in the Mightex camera has an area of $(5.2\ \mu m)^2$ so the energy associated with one count is given by irradiance × pixel area × exposure time, which is:

$$1\ \text{count} = 2.67\times10^{-3}\ \mathrm{W\ m^{-2}} \times \left(5.2\times10^{-6}\ \mathrm{m}\right)^2 \times 10^{-3}\ \mathrm{s} = 7.2\times10^{-17}\ \mathrm{J}$$

This value can now be used in estimating the power in each trap.

5) Computer Generated Light Fields - Results

A series of images were taken of several light fields to find the approximate power in each trap. Bearing in mind that the camera is over exposed if the number of counts in each pixel exceeds 255, a relatively low laser output of 70 mW was used in combination with the laser safety glasses blocking filter. The optical density of this filter was measured by using the photodiode to compare its transmittance with a neutral density filter of known optical density 4.0. The result was a transmittance of 1.33×10^{-5}. All images are 320×240 pixels with approximately half aperture setting (circular diameter of 10.1mm) and the global gain on the camera set to 2.

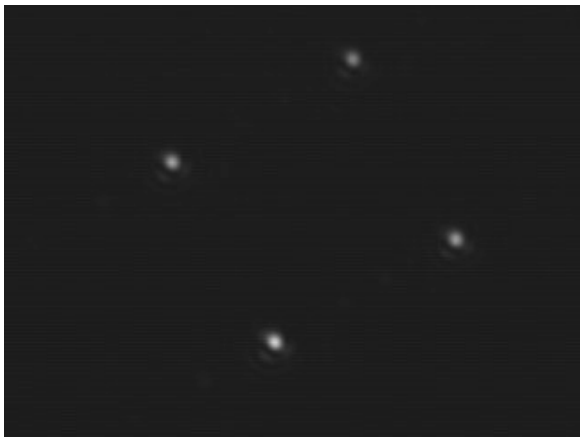

(**Fig. 5.4.1-1a.** HOLO 3, 2 ms exposure time.)

(**Fig. 5.4.1-1b.** HOLO 3, 3.5 ms exposure time.)

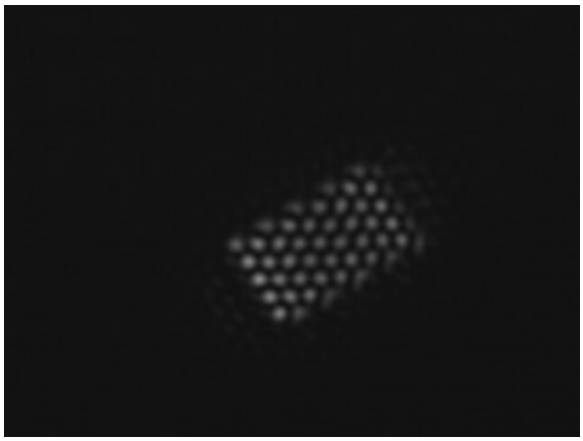

(**Fig. 5.4.1-2.** HOLO 5, 50 ms exposure time.)

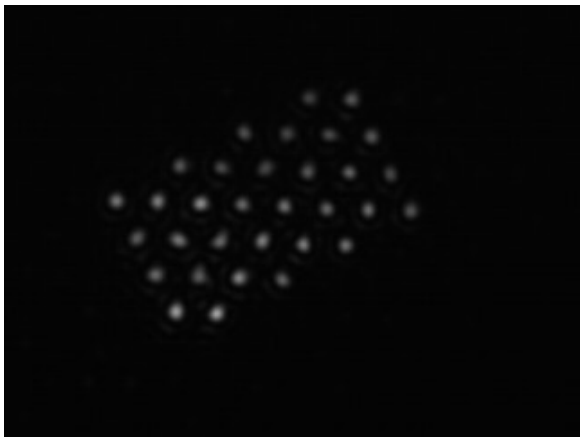

(**Fig. 5.4.1-3.** HOLO 7, 6 ms exposure time.)

ImageJ was used to analyse the above images and, taking into account the attenuation of the laser blocking filter, the individual power in each trap was estimated.

HOLO 3 Power in Individual Traps = 2ms Exposure				
Trap	1= Upper Left	2 =Upper Right	3 = Lower Left	4 = Lower Right
Power (W)	$\mathbf{1.69\times10^{-5}}$	$\mathbf{1.33\times10^{-5}}$	$\mathbf{2.33\times10^{-5}}$	$\mathbf{1.68\times10^{-5}}$
HOLO 3 Power in Individual Traps = 3.5ms Exposure				
Trap	1= Upper Left	2 =Upper Right	3 = Lower Left	4 = Lower Right
Power (W)	$\mathbf{1.71\times10^{-5}}$	$\mathbf{1.26\times10^{-5}}$	$\mathbf{2.39\times10^{-5}}$	$\mathbf{1.7\times10^{-5}}$

(**Table. 12** Individual trapping power in HOLO 3 traps.)

HOLO 5 Power in Selected Traps = 50ms Exposure					
Trap:	Upper left	Upper Right	Middle	Bottom Left	Bottom Right
Power (W)	$\mathbf{3.37\times10^{-7}}$	$\mathbf{3.24\times10^{-7}}$	$\mathbf{2.78\times10^{-7}}$	$\mathbf{4.02\times10^{-7}}$	$\mathbf{2.87\times10^{-7}}$

(**Table. 13** Individual trapping power in selected HOLO 5 traps.)

HOLO 7 Power in Individual Traps = 6ms Exposure					
	Row	Trap 1	Trap 2	Trap 3	Trap 4
Power (W)	Top 1	$\mathbf{4.49\times10^{-6}}$	$\mathbf{3.42\times10^{-6}}$	$\mathbf{3.03\times10^{-6}}$	$\mathbf{2.63\times10^{-6}}$
	2	$\mathbf{4.87\times10^{-6}}$	$\mathbf{2.93\times10^{-6}}$	$\mathbf{2.95\times10^{-6}}$	$\mathbf{3.54\times10^{-6}}$
	3	$\mathbf{3.9\times10^{-6}}$	$\mathbf{5.6\times10^{-6}}$	$\mathbf{3.13\times10^{-6}}$	$\mathbf{2.76\times10^{-6}}$
	4	$\mathbf{4.94\times10^{-6}}$	$\mathbf{3.89\times10^{-6}}$	$\mathbf{3.52\times10^{-6}}$	$\mathbf{3.46\times10^{-6}}$
	5	$\mathbf{4.4\times10^{-6}}$	$\mathbf{4.51\times10^{-6}}$	$\mathbf{4.0\times10^{-6}}$	$\mathbf{3.53\times10^{-6}}$
	6	$\mathbf{4.47\times10^{-6}}$	$\mathbf{4.93\times10^{-6}}$	$\mathbf{3.63\times10^{-6}}$	$\mathbf{2.67\times10^{-6}}$
	7	$\mathbf{6.32\times10^{-6}}$	$\mathbf{5.35\times10^{-6}}$	$\mathbf{4.4\times10^{-6}}$	$\mathbf{3.81\times10^{-6}}$
	Bottom 8	$\mathbf{6.37\times10^{-6}}$	$\mathbf{3.65\times10^{-6}}$	$\mathbf{3.78\times10^{-6}}$	$\mathbf{3.35\times10^{-6}}$

(**Table. 14** Individual trapping power in HOLO 7 traps.)

Tables 12-14 display the approximate trapping power of selected traps in the above images for an aperture of 10.1 mm×10.1 mm at the hologram holder. If a 1.5 W beam power was used instead of 70 mW and keeping the aperture constant, then it can be estimated that the power in each trap would be about 20 times greater. Also, if the aperture was increased to full (i.e. the entire hologram is exposed) then there would also be an increase in the power associated with each trap. For example, from the HOLO 3 results, it would be expected that each trap would be in the order of 1–2 mW if full aperture was used with a beam power of 1.5 W.

As mentioned above, these figures are only approximate. Nevertheless, they can be used as a guide to the order of magnitude of the power associated with each trap. The intensity profiles of HOLOs 3, 5 & 7 are shown in Figs. 5.4.1-4–6.

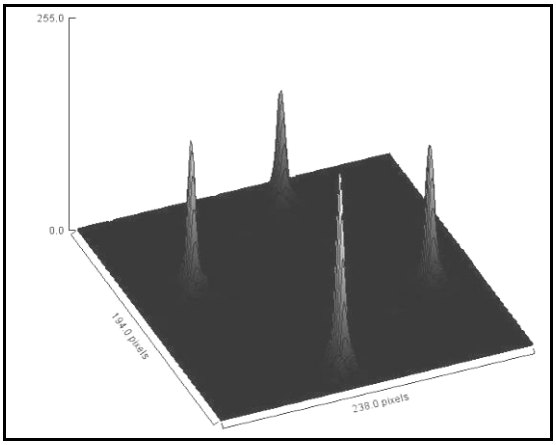

(**Fig. 5.4.1-4** HOLO 3 intensity profile.)

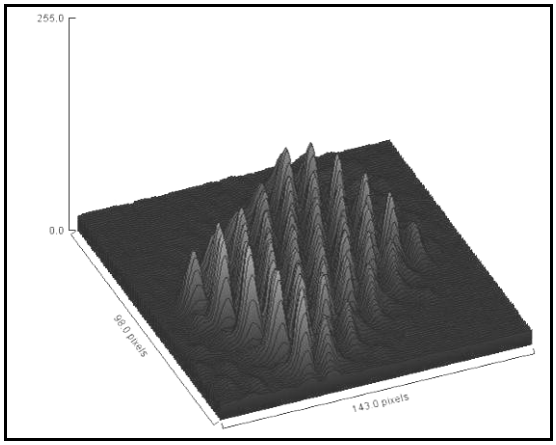

(**Fig. 5.4.1-5** HOLO 5 intensity profile.)

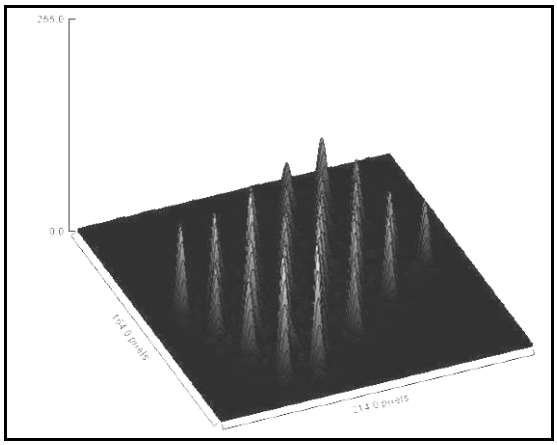

(**Fig. 5.4.1-6** HOLO 7 intensity profile.)

The plots are a 3D representation of intensity vs. area in the form of counts vs. pixels. The HOLO 3 traps in Fig 5.4.1-4 have a narrower and taller profile than the HOLO 5 traps in Fig 5.4.1-5 which is unsurprising considering the differences in the measured power of the two light fields. HOLO 7 (Fig 5.4.1-6) lies between these two extremes; its traps are narrower and more intense than HOLO 5 but do not approach HOLO 3's level. The variation in trapping intensities within each light field is evident and this is especially noticeable in the profiles of HOLO 5 and HOLO 7. These differences in trap power are due to the fact that HOLO 5 & 7 both contain more traps than HOLO 3 and thus, the incoming laser power is diverted into a larger number of traps.

6) Optical Trapping

This chapter concerns itself with results obtained from various optical trapping experiments using a single laser beam and different trapping configurations generated from various holograms. Two types of particles were used in the colloidal solution along with different solvents.

6.1) Single Beam Optical Trap

To test the suitability of the display set up, a single beam optical trap was used to capture single particles. The particles used were poly(methyl)methacrylate macroparticles (PMMA) immersed in decalin (decahydronaphthalene) and were prepared by the Colloids research group at RMIT University. The PMMA particles have an average diameter of 2 μm. Later on, polystyrene particles (diameter of 2.5 μm) immersed in a 4:1 water/glycerol mix were used instead. Trials were initially conducted using particles immersed in a dodecane solution as the particles were prepared in these solutions. Dodecane and decalin were used as they are necessary for index matching in colloidal investigations.

Particles:	**Density: (g cm^{-3})**	**Refractive Index:**
PMMA $(C_5O_2H_8)_n$	1.19	1.49
Polystyrene $(C_8H_9)_n$	1.05	1.52
Solvents:		
Decalin ($C_{10}H_{18}$)	0.896	1.469-1.481
Dodecane ($C_{12}H_{26}$)	0.753	1.421-1.423
Glycerol ($C_3H_3(OH)_3$)	1.261	1.47
Water (H_2O)	1.000	1.33

(**Table. 15** Density and Refractive Index values for particles and solvents.)

6.1.1) Microscope images of PMMA

The following images (Figs. 6.1.1-1-4) show PMMA particles in decalin ($C_{10}H_{18}$) observed through a Zeiss 'Ultraphot' microscope. Figure 6.1.1-1 shows particles fully immersed in decalin while Fig. 6.1.1-2 shows particles at the edge of the liquid on a glass slide. The particles to the left are still immersed in decalin while the dark ones to the right are on the

slide itself. Figure 6.1.1-3 is a scale image showing 10 µm spacing per small division. Figure 6.1.1-4 shows PMMA particles in a decalin-water solution. Individual particles are to be seen, however aggregation is occurring and there are decalin 'bubbles' (particles trapped in decalin) as well which are the larger, sphere shaped objects.

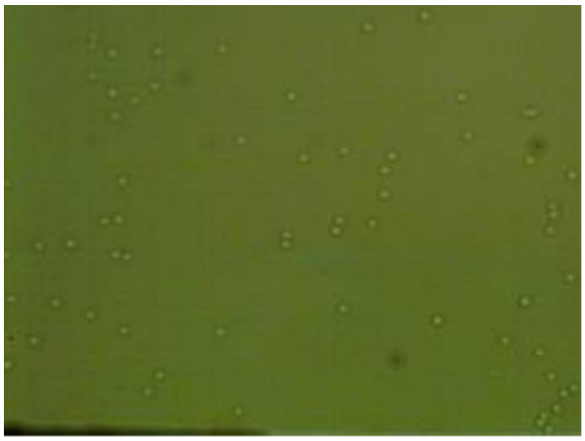

(Fig. 6.1.1-1 PMMA immersed in decalin.**)**

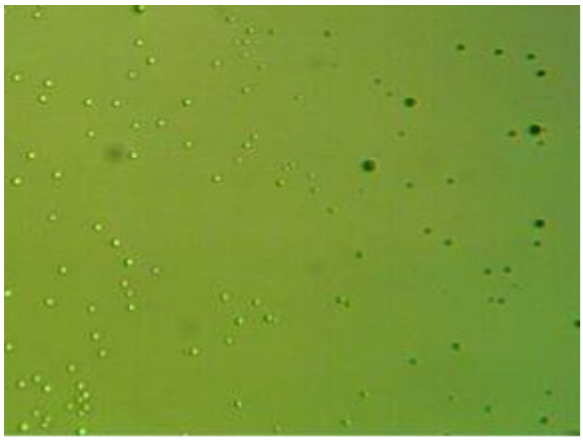

(Fig. 6.1.1-2 PMMA at edge of slide.**)**

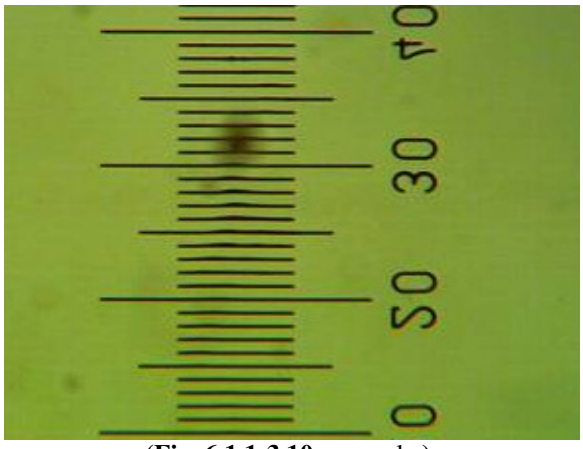

(Fig. 6.1.1-3 10 µm scale.**)**

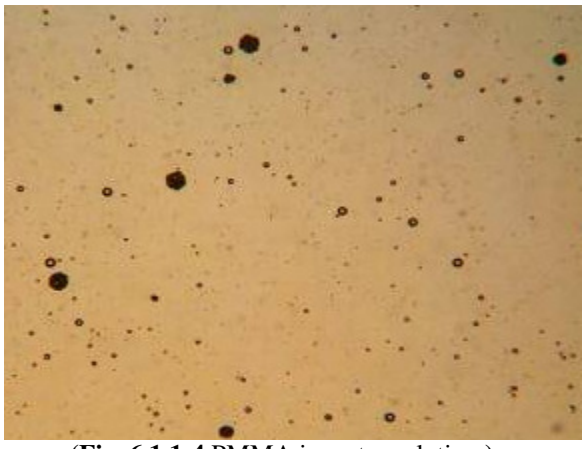

(Fig. 6.1.1-4 PMMA in water solution.**)**

6.1.2) PMMA Particles in decalin and dodecane Solutions

The following images show PMMA particles suspended in a pure decalin solution and in a dodecane solution. Trapping was unsuccessful in both the pure decalin and dodecane solutions owing to the close refractive index difference between the particles and the surrounding solution. For successful trapping, the relative refractive index of the solution (the ratio between the particles and the surrounding liquid) should be between 1.1 and 1.2 whereas for decalin and dodecane, it is 1.01 and 1.05 respectively. The density mismatch also caused the particles to sink rapidly and settle on the bottom of the glass slide. This was more evident

in dodecane due to its low specific gravity (0.753 g/cm^3) compared to PMMA (1.19 g/cm^3). The van der Waals forces of attraction between particles in this case are quite large, causing particles to tend to stick together, and therefore optical trapping is quite difficult.

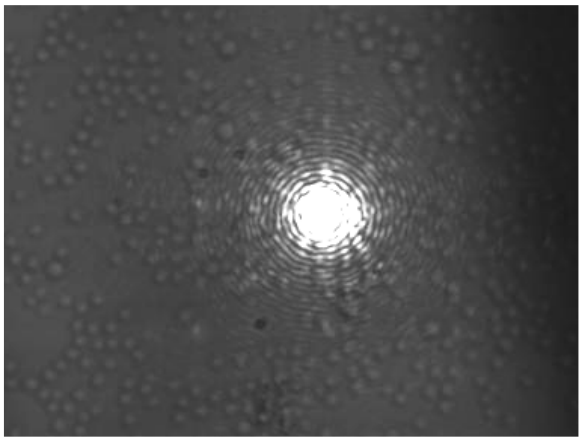

(Fig. 6.1.2-1 Particles in decalin solution.**)**

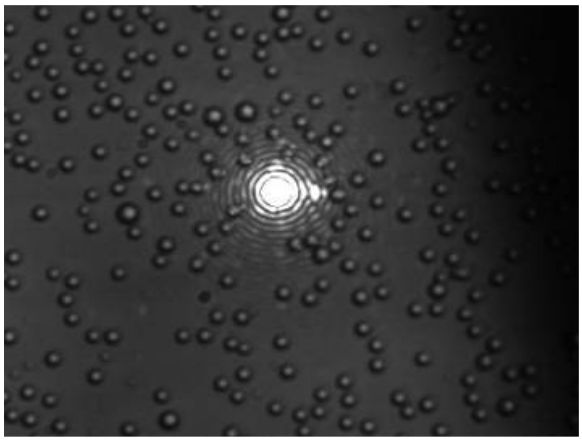

(Fig. 6.1.2-2 Particles in decalin/dodecane solution.**)**

Figure 6.1.2-1 shows PMMA particles suspended in a decalin solution. The bright patch in the centre of the image is the focused laser beam, while the fainter background illumination comes from the incandescent lamp (Fig. 4.5a). The particles appear faint due to the close match of the refractive indexes of the particles and the solution. Decalin is often used for refractive index matching with PMMA hard spheres. This image was taken with a 1.5 W initial beam power.

Figure 6.1.2-2 shows PMMA particles immersed in dodecane. The original images were 640x480 pixels but were cropped to magnify the PMMA particles for ease of viewing. The associated beam power was 650 mW. Some particles were lightly trapped using this solution however no clear images of trapping were taken as the particles would be held for a few seconds at most.

Due to the high beam power required to lightly trap a particle in dodecane (750 mW) combined with the density mismatch and the low relative refractive index, it was determined that this mixture would not be an effective combination for holographic trapping. In fact, the beam power required to achieve this would exceed the output capability of the laser system.

6.1.3) PMMA Particles in decalin & Water Solution

Since trapping was unsuccessful in a purely decalin and a decalin/dodecane solution due to the close refractive index matching of the solvents with the PMMA particles, it was decided to use water as the solvent. This isn't an ideal solution as the PMMA particles were already prepared in decalin, and decalin is insoluble in water. Shaking the solution thoroughly allowed for some of the PMMA particles to break free which is evident in the small particles seen in the images below. These free particles along with particles encased in solvent generally moved across the screen due to convection currents. The larger particles appear to be multiple PMMA spheres encased in decalin. The particles also tended to aggregate together which is visible in some of the images, especially in Fig. 6.1.3. This shows PMMA particles aggregating and forming a flocculation at the water/air barrier of the glass slide. This was observed to be typical behaviour of non-charged PMMA in water. Despite these disadvantages, trapping was achieved quite easily with a single beam and with a hologram (HOLO 3).

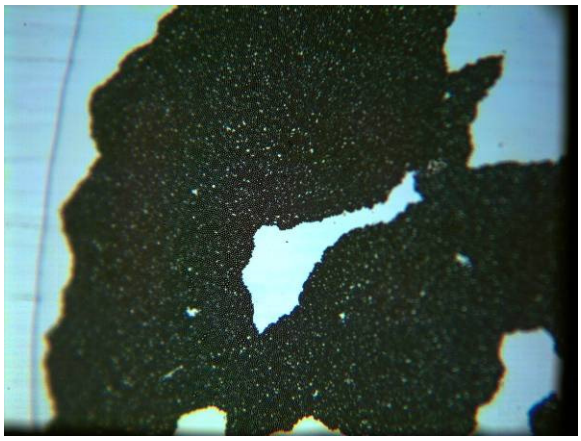

(Fig. 6.1.3 Aggregation and flocculation of PMMA particles in water**)**

6.1.3a) 150mW Beam Power

Note that in the descriptions of the following images, the directions 'north' and 'south' refers to the top and bottom of the images respectively.

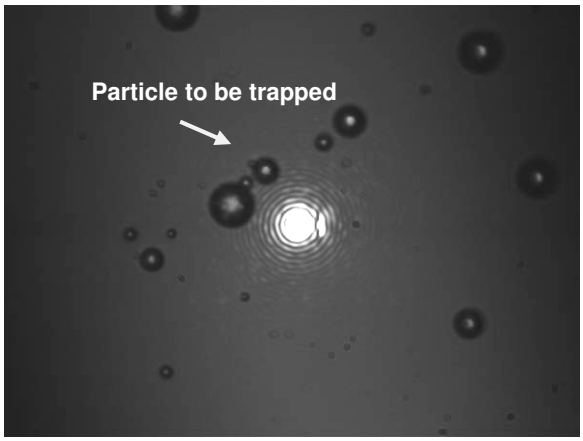

(**Fig. 6.1.3a-1a** Before trapping.)

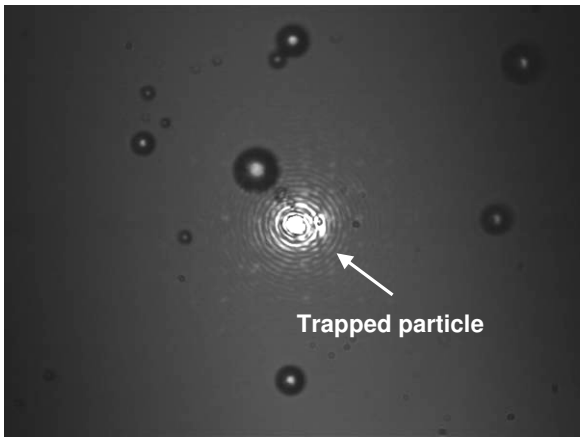

(**Fig. 6.1.3a-1b** After trapping and manipulation.)

Figures 6.1.3a-1a & b show PMMA particles encased in decalin, immersed in water (a) before and (b) after trapping with a single point source. The particle is manipulated in a southward direction. Notice how the smaller middle particle (PMMA) and larger end particle are dragged along as well. The associated diffraction effects caused by the trapping of the particle are clearly visible.

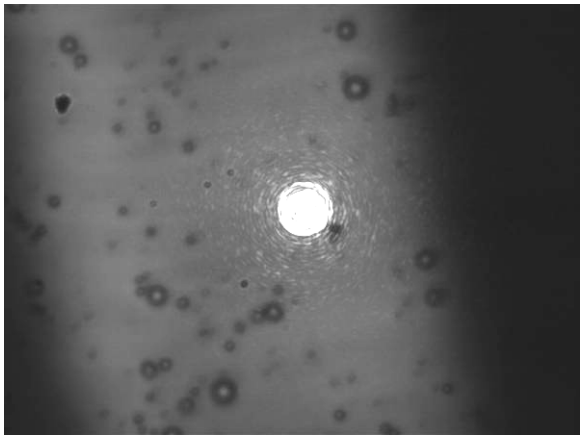

(**Fig. 6.1.3a-2a** Particle trapped in beam.)

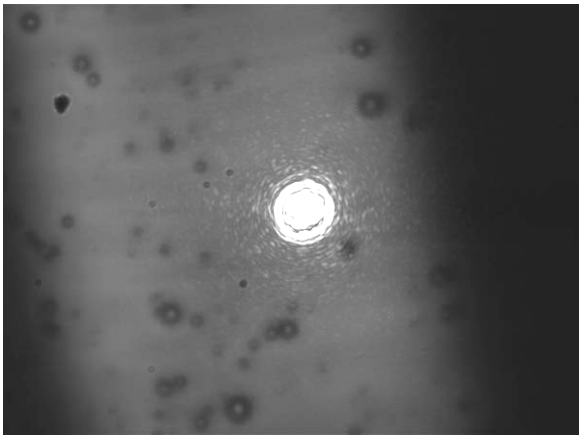

(**Fig. 6.1.3a-2b** Diffraction caused by trapped particle.)

Figures 6.1.3a-2a & b show a PMMA particle trapped in beam. Notice the intense diffraction effects caused by trapping. It was observed that the smaller the particle, the stronger the associated diffraction, as expected from theory. Particles are flowing in a south-easterly direction.

6.1.3b) 80mW Beam Power

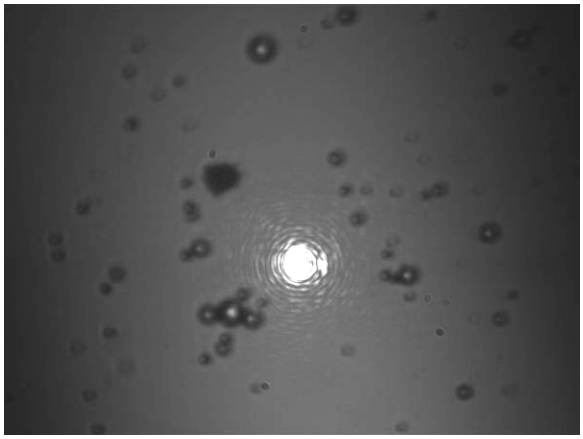

(Fig. 6.1.3b-1a Particles before trapping.**)**

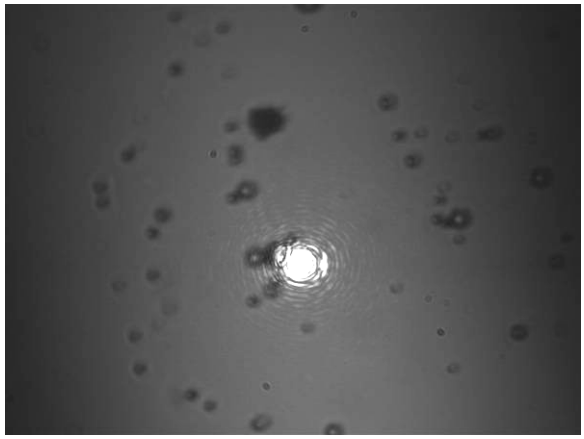

(Fig. 6.1.3b-1b During trapping event.**)**

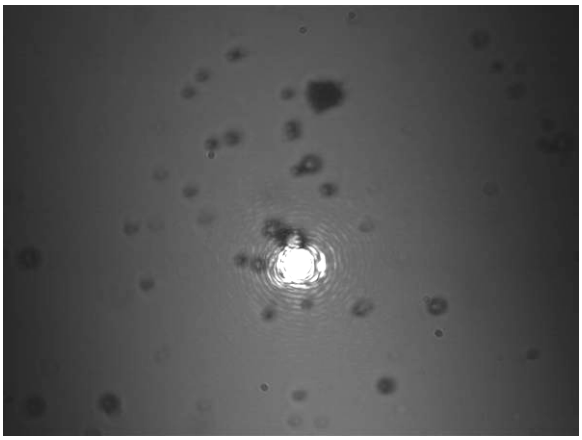

(Fig. 6.1.3b-1c Trapped particle manipulation.**)**

Figures 6.1.3b-1a – c show another series of trapping events with a) particles before trapping, b) a large particle and several smaller particles are now trapped and c) surrounding particles are being dragged by the trap. A small particle (probably a single PMMA particle) has broken free of the small cluster. Particle motion is in a north-easterly direction.

6.1.3c) 65mW Beam Power

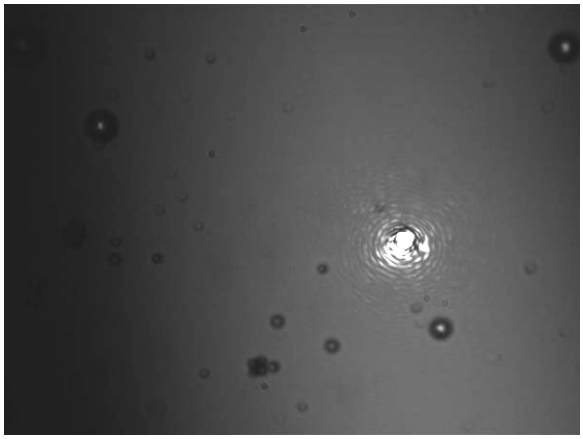

(Fig. 6.1.3c-1a Small trapped particle.**)**

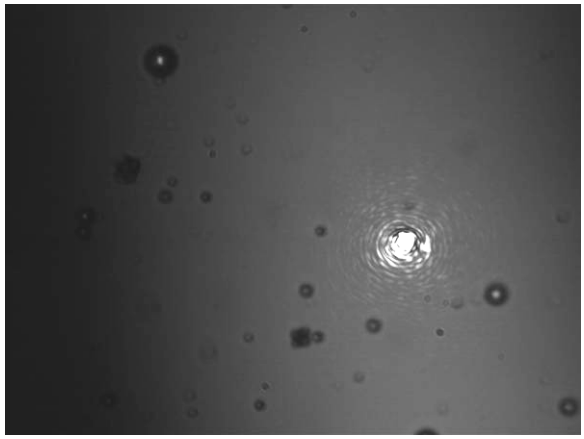

(Fig. 6.1.3c-1b Trapped particle after manipulation.**)**

Figures 6.1.3c-1a & b show a large particle being manipulated by the laser. The particle is visible in the north-eastern part of the trap and is held in place while other particles flow by. It was easier to observe trapping with larger particles because they could still be 'seen' inside the trap. It was more difficult to observe smaller trapped particles as it was harder to distinguish their outline inside the traps and also, the strong diffraction effects mentioned earlier were not always obvious. This may be due to masking of the fringes by the intense direct and scattered light of the trap. It is possible that single beam trapping could be achieved with a lower beam power; however the Spectra Physics Model 2060 Ar^+ laser is not optically-stable at output powers lower than 55–60 mW, although a neutral density filter can be placed in front of the laser to decrease the power in the beam. The 65 mW beam power refers to the initial laser output and beam power at the trapping plane will be considerably lower.

6.2) Holographic Trapping of PMMA Particles

The following images show particles being trapped using HOLO 3. This was the first time that holographic trapping had been achieved at RMIT University. Beam power was initially 1.5 W but was decreased to 1.35 W. The variable aperture below the hologram holder (see Fig. 4.5a) was adjusted, so that only a portion of the hologram was exposed to the beam. This has the effect of reducing the aberrations in the traps but at a cost of decreased power and increased depth of focus. There were three settings used; *full aperture* where the entire hologram was covered by the beam, *half aperture* where only half the hologram area was exposed to the beam and *one-third aperture* where only a third portion of the hologram was

exposed. The following images are all 640×480 pixels in size which corresponds to dimensions of 332 µm×250 µm.

6.2.1) 1.5 W Full Aperture

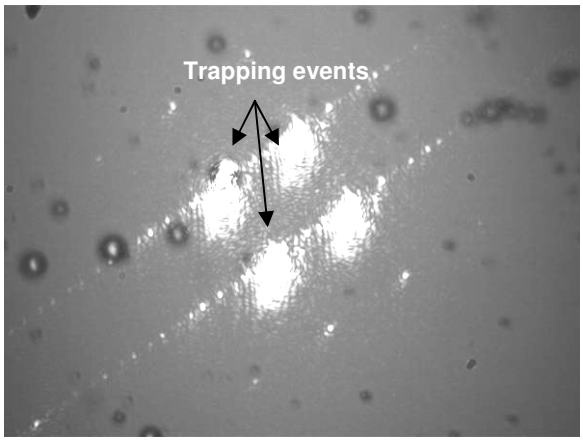

(Fig. 6.2.1-1a)

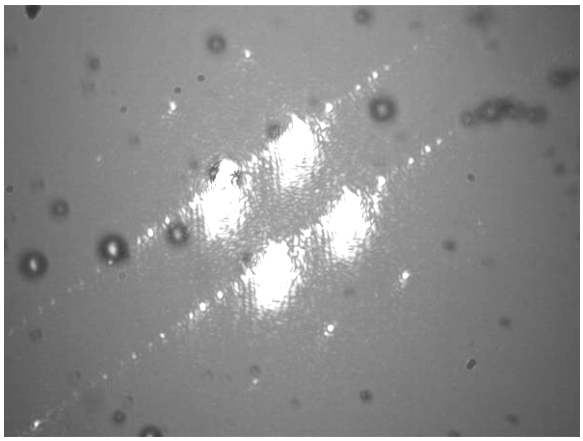

(Fig. 6.2.1-1b)

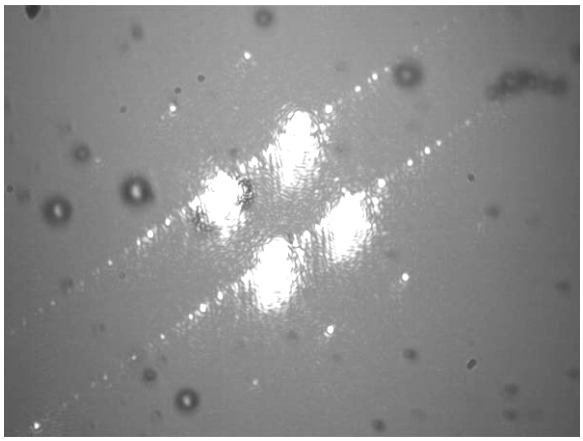

(Fig. 6.2.1-1c)

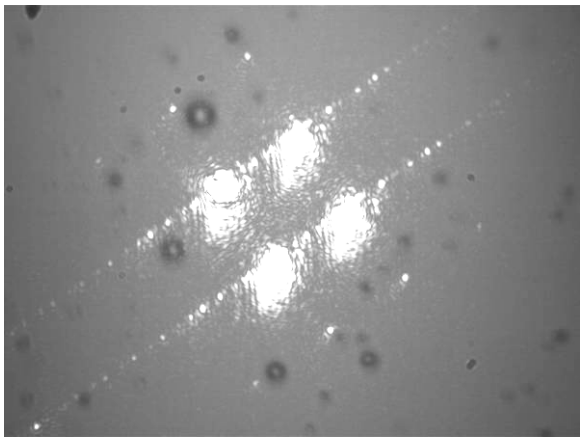

(Fig. 6.2.1-1d)

(Fig. 6.2.1-1 Trapping occurring in three traps over 40 seconds. 1.5 W full aperture.**)**

Figures 6.2.1-1a–c show trapping events occurring over 40 second duration. It is quite difficult to make out but particles have been captured in the top two and bottom-left traps. Particularly in the original digital images, definite diffraction effects can be observed in Fig. 6.2.1-1c in the top-right trap and in the top-left trap in Fig. 6.2.1-1d. Particles are flowing in a north-easterly direction.

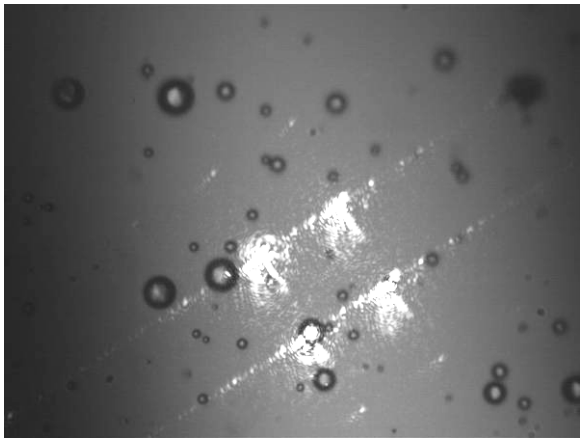

(Fig. 6.2.1-2a)

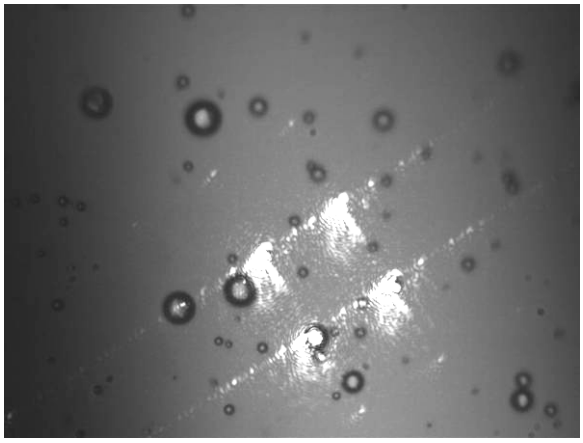

(Fig. 6.2.1-2b)

(Fig. 6.2.1-2 Multiple trapping of PMMA via HOLO 3 over 12 seconds. 1.5 W full aperture)

Figures 6.2.1-2a & b show trapping occurring in three of the four traps. The top left trap has captured a relatively small particle while the bottom left and right traps have captured large and medium sized particles respectively. Trapping is occurring over 12 seconds and particles are flowing in a south-easterly direction. These images have a different exposure to Figs. 6.2.1-1a – c and the traps themselves appear to be less intense due to the fact that they were captured on different occasions with the camera exposure reduced.

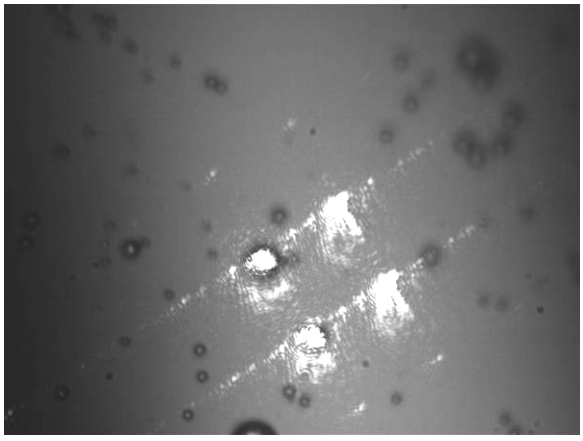

(Fig. 6.2.1-3a)

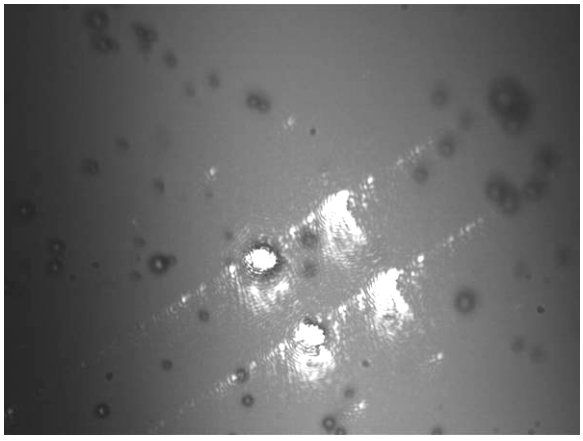

(Fig. 6.2.1-3b)

(Fig. 6.2.1-3 Large PMMA trapped via HOLO 3 over 20 seconds. 1.5 W full aperture.)

Figures 6.2.1-3a & b shows larger particles being captured by the top and bottom left-hand side traps over a period of 20 seconds. Initially there is a smaller particle captured in the bottom right-hand trap in Fig. 6.2.1-3a, however this has been released as shown in Fig. 6.2.1-3b. Particles are flowing in a southerly direction.

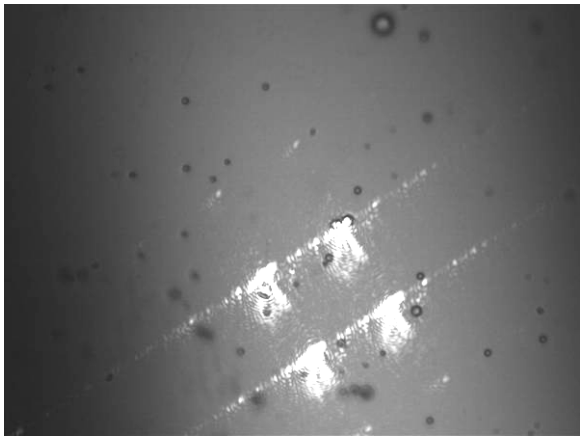

(Fig. 6.2.1-4a)

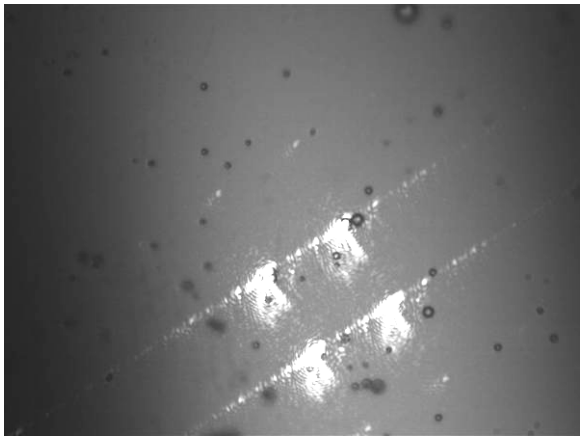

(Fig. 6.2.1-4b)

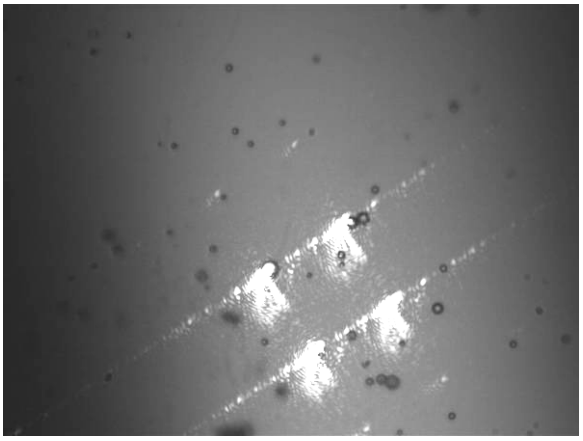

(Fig. 6.2.1-4c)

(Fig. 6.2.1-4 Small PMMA trapped via HOLO 3 over 20 seconds. 1.5 W full aperture.**)**

Figures 6.2.1-4a–c shows smaller particles being captured in three of the four points over a period of 20 seconds. Particles are flowing in an easterly direction. It was observed that it was difficult to trap in the bottom-right trap which is not surprising as this trap has lower power than the others (refer to chapter 5.4. for HOLO 3 trap powers).

6.2.2) 1.5 W Half Aperture

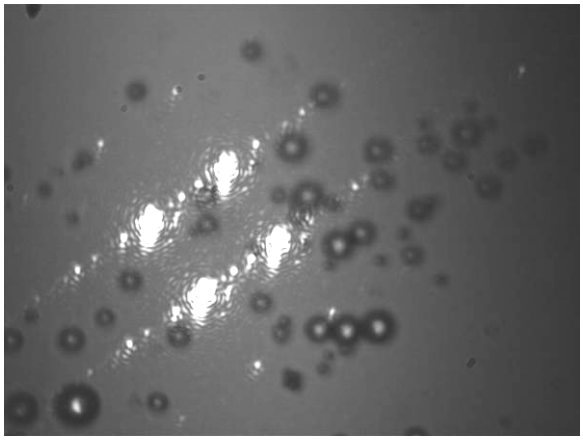

(Fig. 6.2.2-1a)

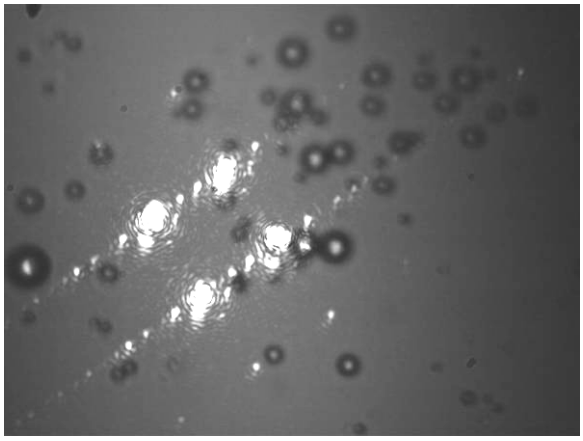

(Fig. 6.2.2-1b)

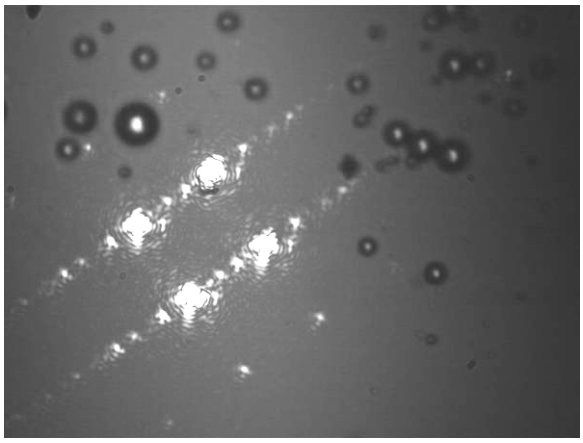

(Fig. 6.2.2-1c)

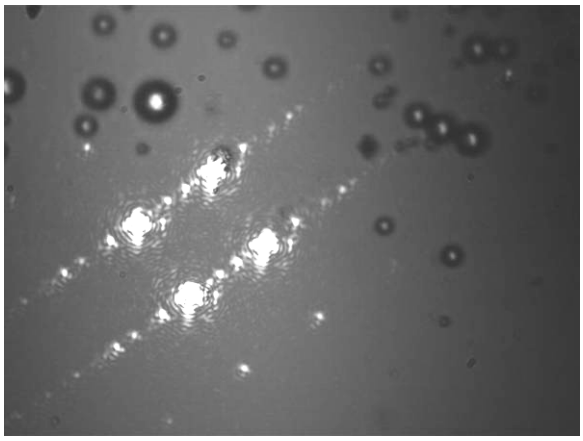

(Fig. 6.2.2-1d)

(Fig. 6.2.2-1. Trapping in each of the four traps via HOLO 3 over 2 min. 1.5 W half aperture.)

Figures 6.2.2-1a–d show trapping events occurring in each of the four traps over time. Two small joined particles, appearing in the lower-left hand corner in Fig. 6.2.2-1b, have subsequently been trapped by the bottom-left trap in Fig. 6.2.2-1c & d. Other particles, especially a large one, are located in the top two traps. Particles are flowing in a north-easterly direction and these events are occurring over duration of approximately 2 minutes.

6.2.3) 1.5 W One-Third Aperture

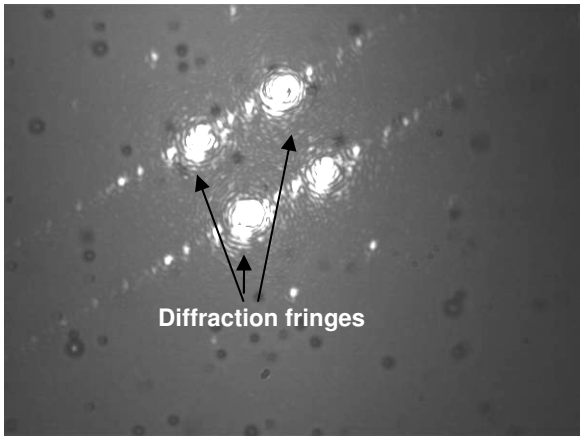

(Fig. 6.2.3-1a)

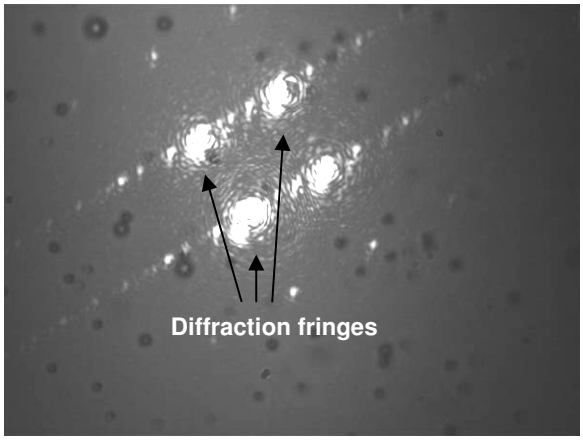

(Fig. 6.2.3-1b)

(Fig. 6.2.3-1 Trapping via HOLO 3 over 25 seconds. 1.5 W one-third aperture.)

Figures 6.2.3-1a & 1b show trapping occurring in several of the traps over a period of 25 seconds. The two top and bottom-left traps contain particles which is evident in the strong diffraction fringes present around these traps. Particles are flowing in a north-east direction. The difference in the apparent quality of the traps compared to images with higher aperture settings is clearly evident.

6.2.4) 1.35 W Full Aperture

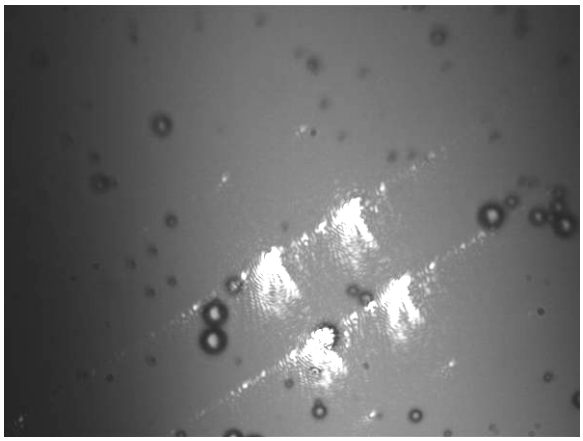

(Fig. 6.2.4-1a)

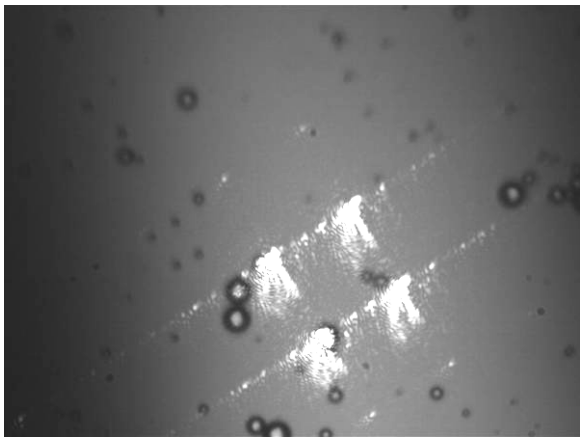

(Fig. 6.2.4-1b)

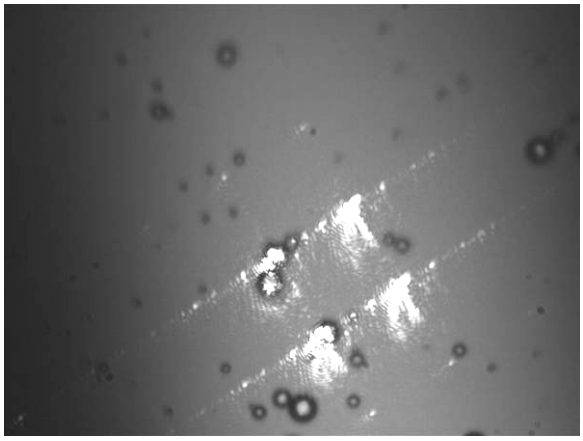

(Fig. 6.2.4-1c)

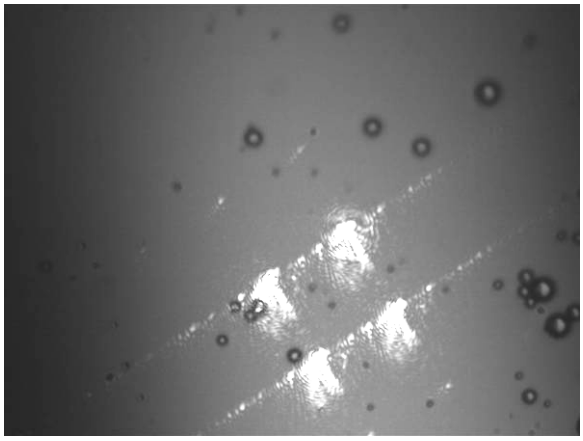

(Fig. 6.2.4-2a)

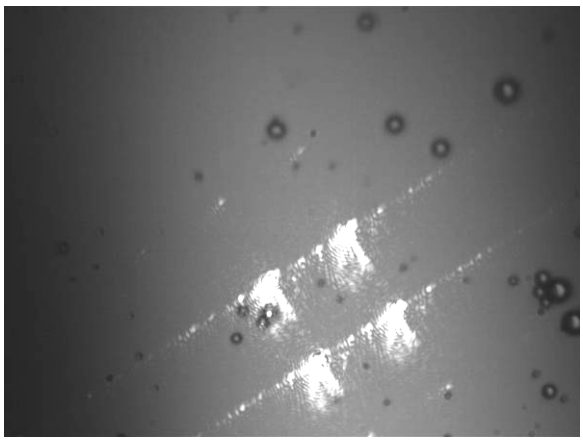

(Fig. 6.2.4-2b)

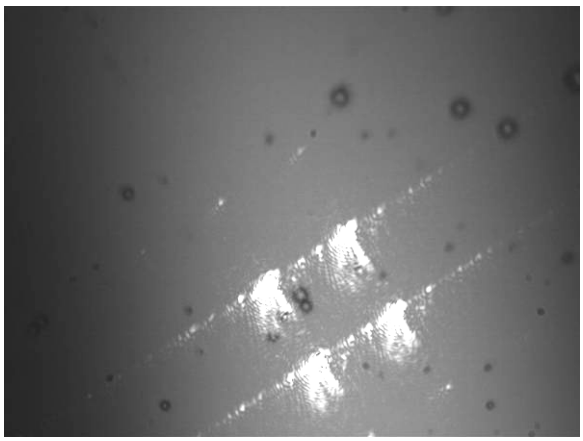

(Fig. 6.2.4-2c)

(**Fig. 6.2.4-1** Trapping via HOLO 3 over 15s.)

(**Fig. 6.2.4-2** Trapping via HOLO 3 over 30s.)

Figures 6.2.4-1a–c show trapping events occurring over a period of 15 seconds in multiple traps. There is a large particle captured in the bottom-left trap as well as the top-right trap which has been released in the following images (small, faint particle northeast of the top-right trap in Fig. 6.2.4-1b). The top-left trap has managed to capture a particle in Fig. 6.2.4-1b which is then pushed out of the trap by a larger particle in Fig. 6.2.4-1c. The large particle has remained captured in the lower-left trap for the duration and is about to be joined by a smaller particle in Fig. 6.2.4-1c. Figures 6.2.4-2a–c shows another series of trapping events occurring over 30 seconds. Figure 6.2.4-2a shows a particle about to be captured by the bottom-left trap while the top-left has a trapped particle and a particle is just about to escape the top-right trap. There is no evidence of this particle in either Fig. 6.2.4-2b or 2c which suggests the particle has been 'pushed' by the trap along the z direction and is now no longer in focus. The top-left trap now has two particles captured in Fig. 6.2.4-2c. Particles are flowing in a north easterly direction for both series of trapping events.

6.2.5) 1.35 W One-Third Aperture

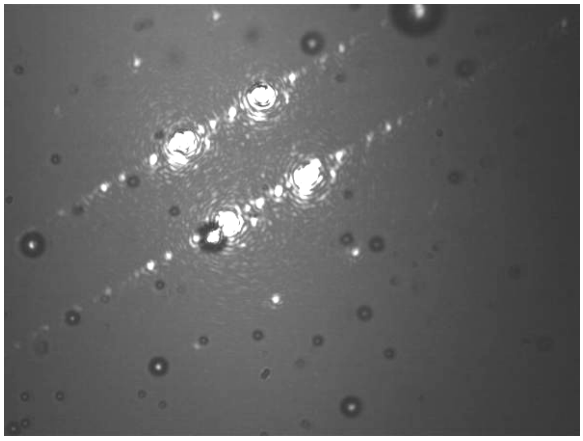

(Fig. 6.2.5-1a)

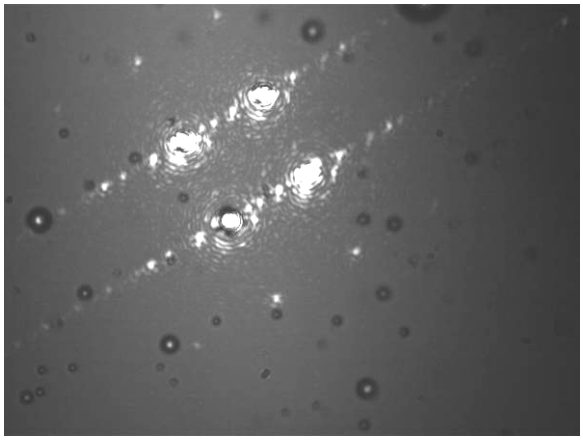

(Fig. 6.2.5-1b)

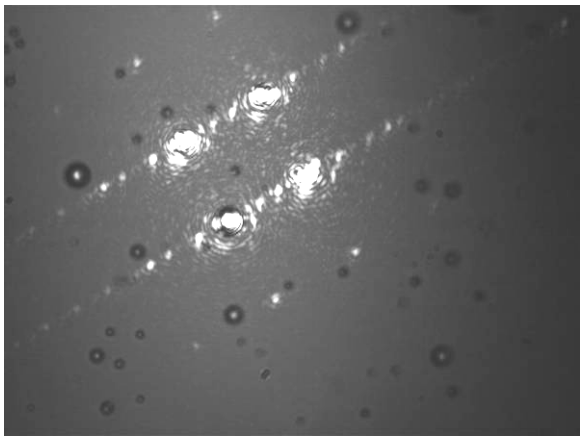

(Fig. 6.2.5-1c)

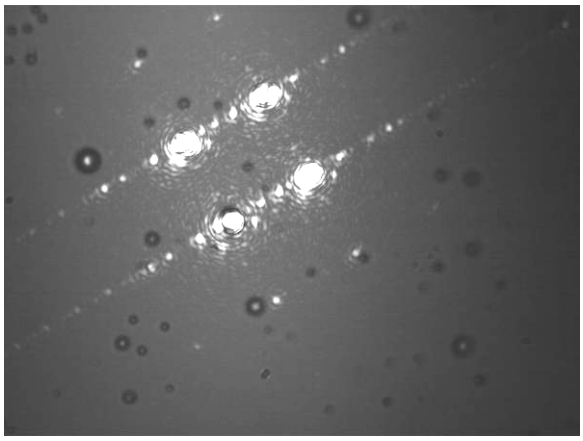

(Fig. 6.2.5-1d)

(**Fig. 6.2.5-1** Multiple trapping via HOLO 3 over 30 seconds. 1.35 W third aperture.)

Figures 6.2.5-1a–d show trapping occurring in each of the four traps. The traps are able to hold the particles in place while others flow in a northeast direction. The lower-left trap has a particularly large particle confined, which can be seen about to enter the trap in Fig. 6.2.5-1a. The outline of this trapped particle is clearly evident in the subsequent images. Trapping is occurring over a period of 30 seconds.

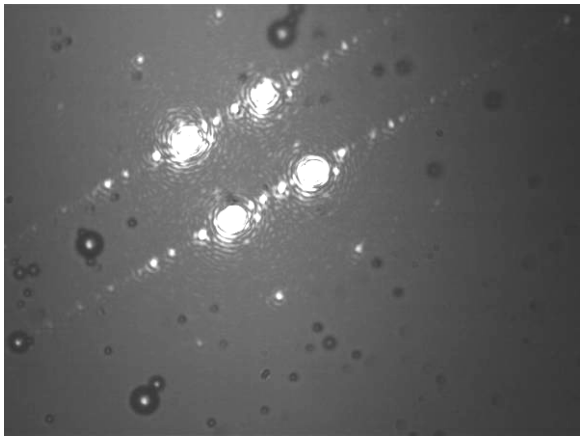

(Fig. 6.2.5-2a)

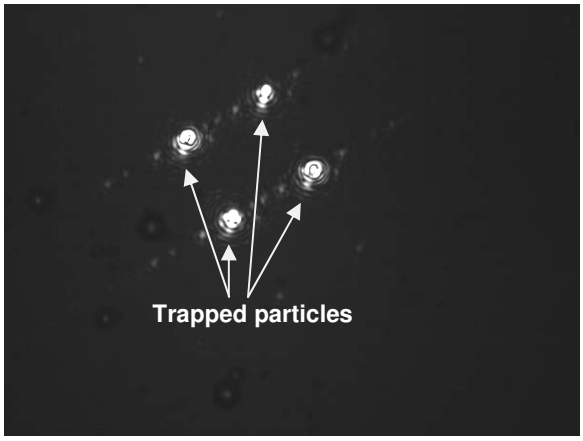

(Fig. 6.2.5-2b)

(**Fig. 6.2.5-2** Particles trapped in all 4 traps via HOLO 3. 1.35 W third aperture)

Figures 6.2.5-2a & b show trapping occurring in all four traps. Fig. 6.2.5-2b has a decreased exposure time which aids in the viewing of the particles within the traps. The particles appear as bright points of light, with a dark fringe outlining the shape of the particle. The particle in the top-right trap is quite difficult to make out as it is centred in the middle of the trap. The lower-left trap has captured two small particles. These particles are believed to be PMMA that has managed to separate from the decalin solution.

These trapping images are significant as they show trapping occurring even when the traps themselves show quite severe aberrations. While studies have shown that this is possible [83], the ease with which particles were captured was surprising. The power in each trap is quite small, possibly no greater than 1-2 mW each for the 1.5 W power setting and large aperture (refer to chapter 5.4.1 for HOLO 3 power loss measurements). It was observed that larger particles were captured with greater ease compared to the smaller particles. This is to be expected, since the gradient forces acting on the particles will be greater for larger sizes than for small ones. The trapped particles could be manipulated in the *x, y* direction by carefully adjusting the fine controls on the sample holder. It is believed that these larger particles were PMMA particles encased in decalin.

The difference in the apparent quality of the traps with low aperture settings compared to traps with higher aperture settings is clearly evident; however, while decreasing the aperture greatly enhances the 'look' of the trap, there is a disadvantage of broadening the central focal point of each trap and the overall trapping power of each trap obviously decreases. It was

observed that it was difficult to trap particles with a 1.35 W beam power since this results in a trap power < 1 mW. However, it has been shown that trapping is indeed possible at these low powers although the particle tends to be only 'lightly' held and can escape quite easily when influenced by external factors such as slight vibrations and thermal currents.

6.3) Holographic Trapping of Polystyrene Particles

As mentioned above, the PMMA/water solution is not ideal, due to the presence of decalin. Therefore it was decided to use 2.5 µm polystyrene spheres (Bangs Labs PS05N/5893 inv#L030808A) which could be easily mixed with water and offered a good refractive index contrast. Glycerol was added to the water/particle solution to density match the particles with the surrounding solvents. This was a 4:1 ratio of water to glycerol by volume. The images in this section are all 320×240 pixels in size which corresponds to dimensions of 166 µm ×125 µm.

6.3.1) 1.5 W Half Aperture

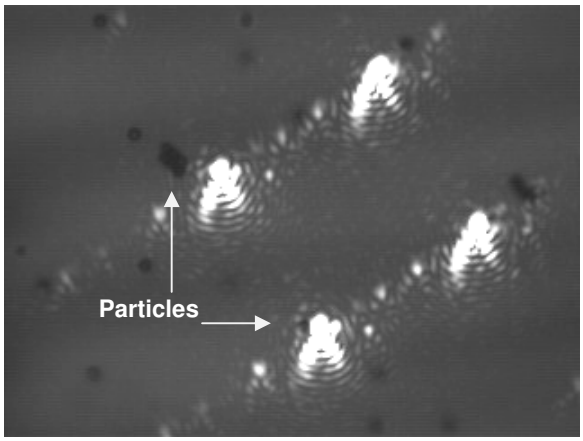

(**Fig. 6.3.1-1a**)

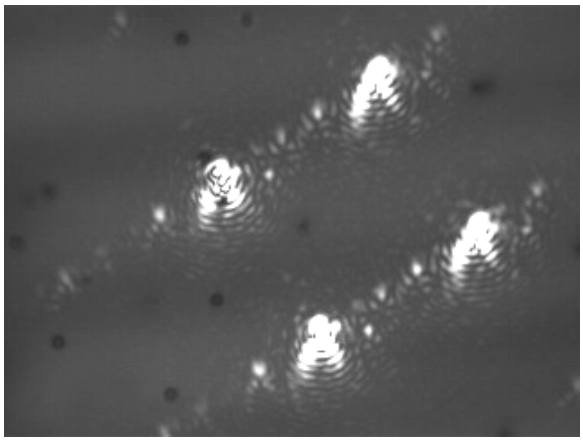

(**Fig. 6.3.1-1b**)

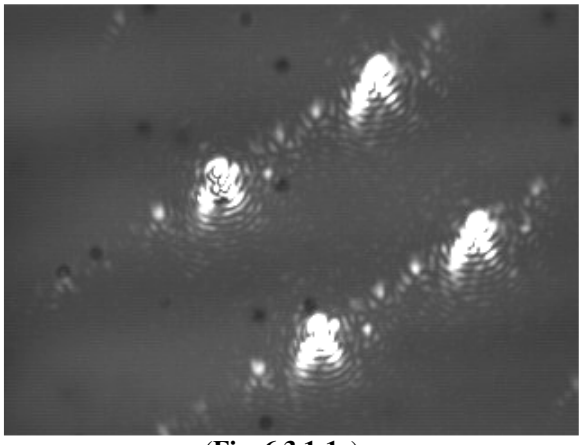

(**Fig. 6.3.1-1c**)

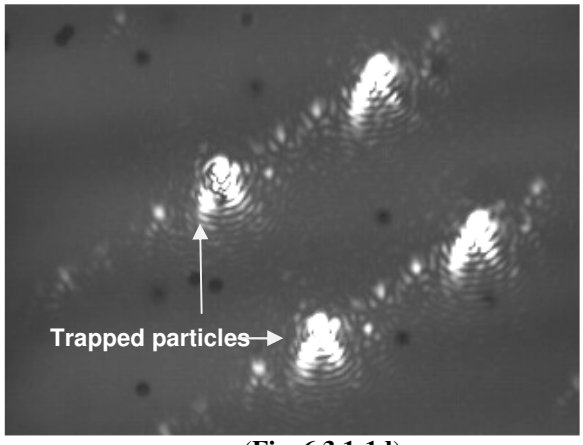

(**Fig. 6.3.1-1d**)

(Fig. 6.3.1-1 Polystyrene particles being trapped via HOLO 3 over 30 seconds. 1.5 W half aperture.**)**

Figures 6.3.1-1a–d show trapping occurring over a 30 second period. A cluster of particles are just about to enter the top-left trap and a single particle is about to be caught in the bottom-left trap in Fig. 6.3.1-1a. These particles remain trapped while others flow by in the subsequent images. Particles are flowing in a south easterly direction. Particles at different depths can be observed in the solution.

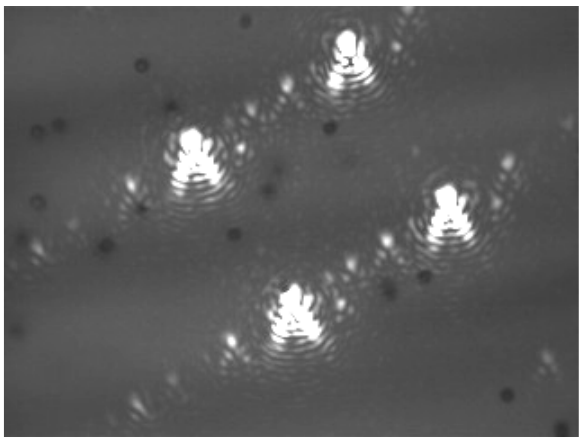

(Fig. 6.3.1-2a)

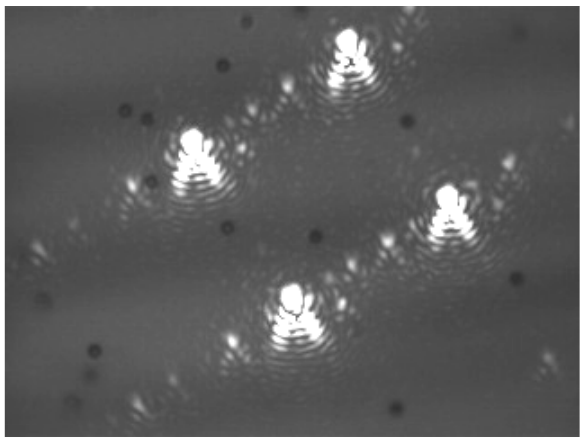

(Fig. 6.3.1-2b)

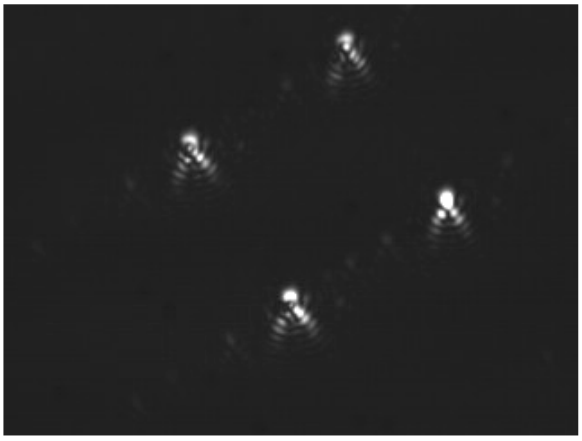

(Fig. 6.3.1-2c)

(**Fig. 6.3.1-2** Polystyrene particles trapped in all 4 traps via HOLO 3 over 30 seconds. 1.5 W half aperture.)

Figures 6.3.1-2a & b show particles captured in all four traps over 30 seconds with the camera exposure reduced to observe particles in Fig. 6.3.1-2c. A particle has subsequently escaped the bottom-right trap in this image. The trapped particles appear to be small bright points with a dark circular fringe around them. They are quite difficult to distinguish in Figs. 6.3.1-2a & b as the large amount of aberration present in the traps tends to swamp the diffraction effects of trapping.

6.3.2) 1.5 W One-Third Aperture

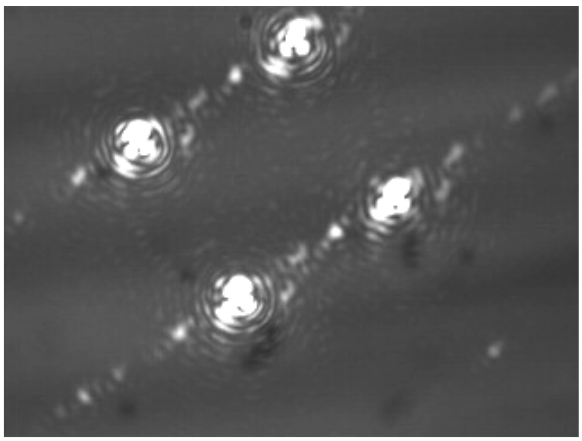

(Fig. 6.3.2-1a)

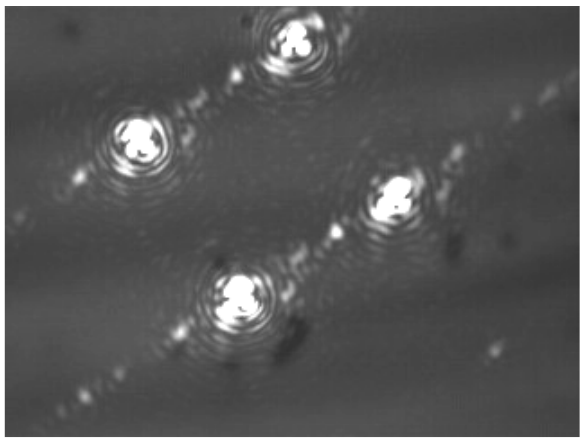

(Fig. 6.3.2-1b)

(Fig. 6.3.2-1 Polystyrene trapping via HOLO 3 over 6 seconds. 1.5 W third aperture.)

These two images show trapping occurring over period of 6 seconds. The decreased aperture reduces the visible aberration effects but at a cost of reduced power in each of the traps.

Nevertheless, three particles are trapped in three of the four traps. The circular diffraction effects are more prominent in the above images.

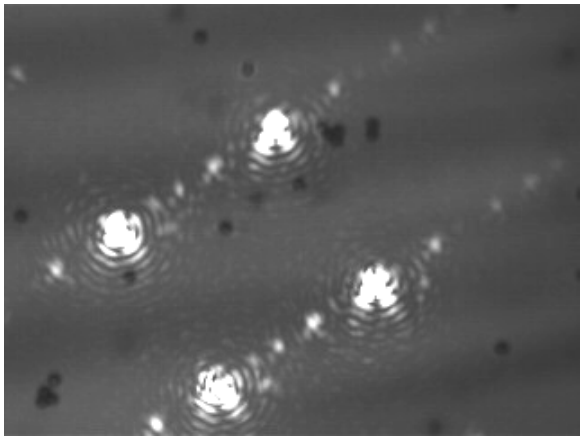

(Fig. 6.3.2-2a)

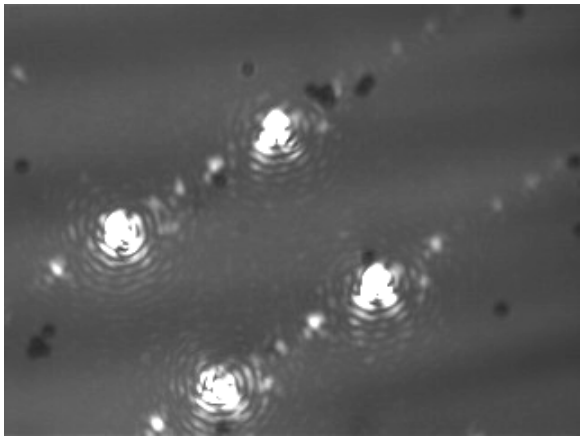

(Fig. 6.3.2-2b)

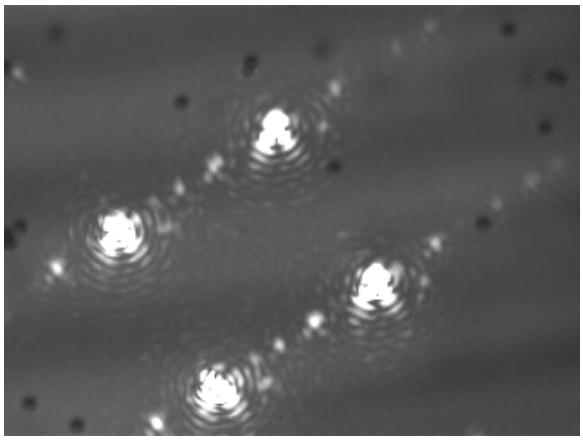

(Fig. 6.3.2-2c)

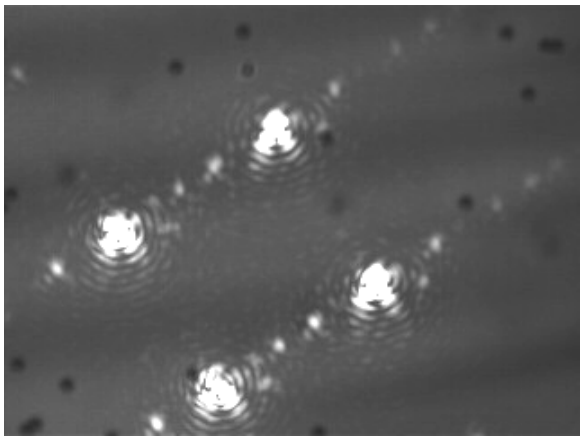

(Fig. 6.3.2-2d)

(Fig. 6.3.2-2 Polystyrene trapping via HOLO 3 over 35 seconds. 1.5 W third aperture.**)**

Figures 6.3.2-2a–d shows multiple trapping occurring over a period of 35 seconds. Trapping has occurred in three of the four traps and particles are flowing in a northerly direction. The top-left trap is empty while the others contain particles. It should be noted that it is difficult to trap with this particular aperture setting since the associated trapping power is low. For successful trapping to occur, particles had to have a slow flow rate and any sudden change in current or slight vibration would be enough to release the particle from the trap.

It was observed that polystyrene particles flowed in two, sometimes three different directions in motion which was dependent on the depth of the solution. For example, particles observed towards the bottom of the glass well (i.e. quite deep in the solution) would flow in an east-

west direction, while particles at middle depth and above would flow in a west-east direction or vice versa. The same is true for particles flowing in a north-south direction. However, specific particle flow cannot be attributed to a particular depth, rather it can be said that different depths result in different flow directions. It is believed that these flows were the result of thermal convection currents in the solvent generated by the laser heating the glass slide and by vibrations. This latter factor may be the cause of unusual behaviour observed with the nature of the particle flow. Particles would be observed to flow in a particular direction, and then they would suddenly change direction. This process was quite dramatic to observe as it was groups of particles reacting to this sudden change at the same time. The power of the optical traps was not strong enough to withstand this sudden change of motion and any trapped particles would be pushed/pulled free.

It was not possible to capture particles with HOLO 5 or HOLO 6 due to the weak powers of the individual point sources. Particles were observed to pass over the light field without being affected by its presence. This was partially expected as results obtained from rudimentary power loss measurements in chapter 5.4 indicated a loss of at least 95% of the initial beam power. Therefore, the individual trapping force is insufficient to overcome the Stokes drag force acting on a particle. The higher efficiency associated with the random phase method offered a greater chance of success of multiple particle trapping.

6.4) Holographic Trapping of Polystyrene Particles with Multiple Light Fields

Trapping was successfully undertaken using HOLO 7. The following images show trapping occurring at a variety of input laser powers. The variable aperture was set to half for all images with a 1.5 ms exposure time for the digital camera (except where noted.). The following images have greater background light intensity due to the fact that the traps in HOLO 7 are less intense than HOLO 3 so the background light from the incandescent lamp is able to be more clearly observed. It is also easier to observe particles at different depths in the solution and these appear as dim, unfocused spheres in following images. Trapping was also attempted on HOLO 16; however the light field was too weak for trapping. The images in this section are all 320×240 in size which corresponds to dimensions of 166 μm ×125 μm.

6.4.1) 1.65 W Half Aperture

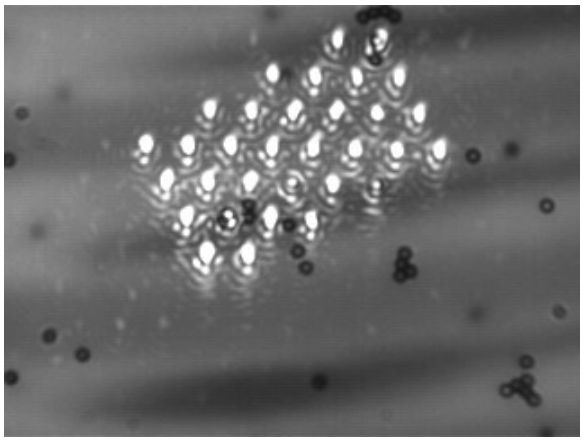

(**Fig 6.4.1-1a**)

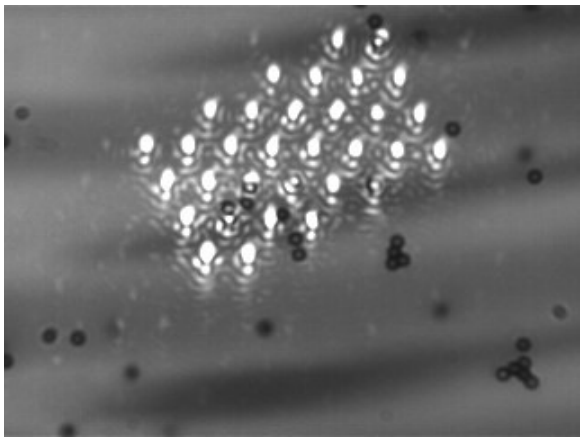

(**Fig. 6.4.1-1b**)

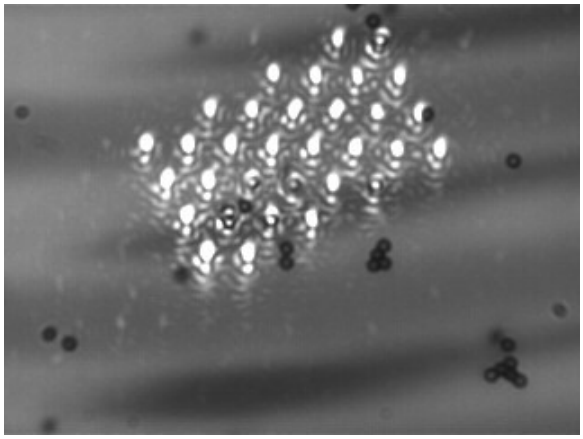

(**Fig. 6.4.1-1c**)

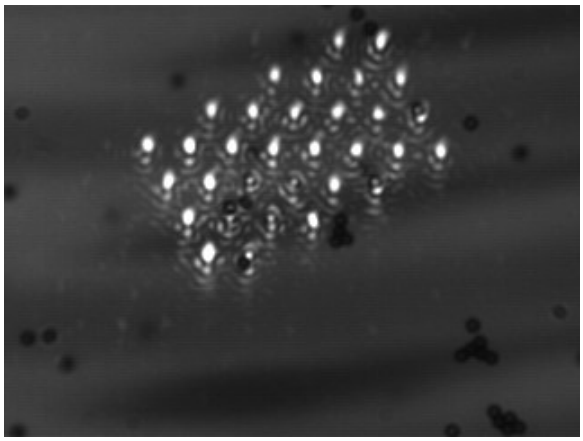

(**Fig. 6.4.1-1d**)

(Fig. 6.4.1-1 Multiple trapping via HOLO 7 over 25 seconds. 1.65 W half aperture.**)**

Figures 6.4.1-1a–c show multiple trapping of particles occurring over 25 seconds with a beam power of 1.65 W. Particles are flowing in a northerly direction. Figure 6.4.1-1a shows at least five particles trapped in various locations with one located in the top right trap, another in the third trap from the left in the bottom row and several trapped in the third row from the bottom. Figures 6.4.1-1b & c are a continuation and they also show new trapping events occurring. Figure 6.4.1-1d is darker due to the exposure setting on the camera being decreased in an attempt to provide contrast between the occupied and unoccupied traps. There are at least seven occupied traps present.

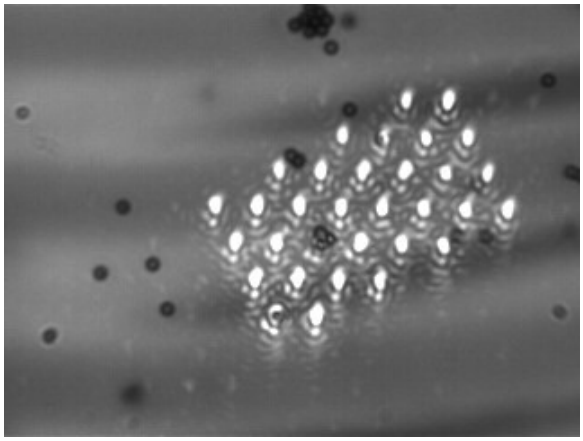

(**Fig. 6.4.1-2a**)

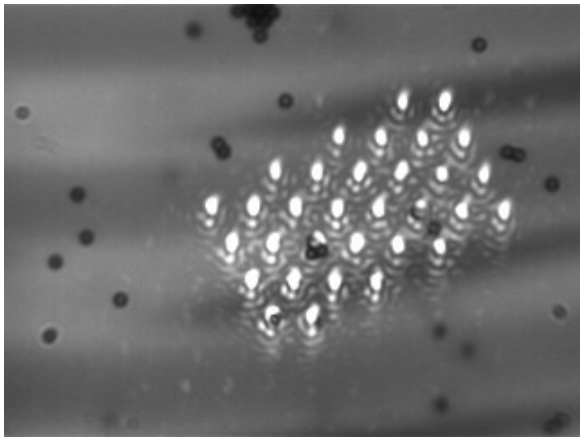

(**Fig. 6.4.1-2b**)

(Fig. 6.4.1-2 Multiple trapping via HOLO 7 over 10 seconds. 1.65 W half aperture.**)**

Figures 6.4.1-2a & b show trapping occurring in several traps over 10 seconds; these being primarily the lower-left trap and a cluster of particles in a middle trap. This sequence shows a particle being ejected from a trap (located in the second row from the top, in the trap second from the right in Fig. 6.4.1-2a). This particle is no longer visible in Fig. 6.4.1-2b, suggesting that it has been pushed out of microscope focus which implies that the trap is not tightly focused. Figure 6.4.1-2b also shows two new trapping events occurring as well. Particles are flowing in the westerly direction.

6.4.2) 1.5 W Half Aperture

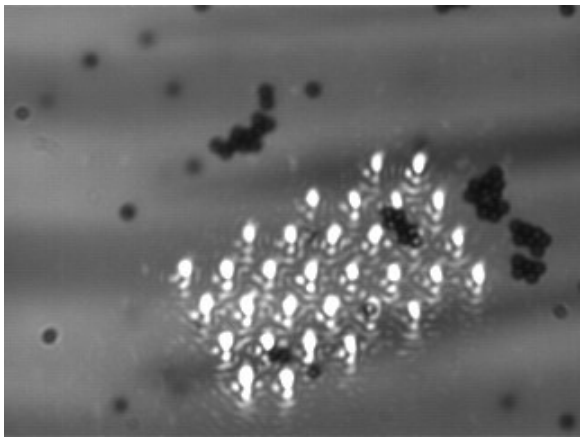

(Fig. 6.4.2-1a)

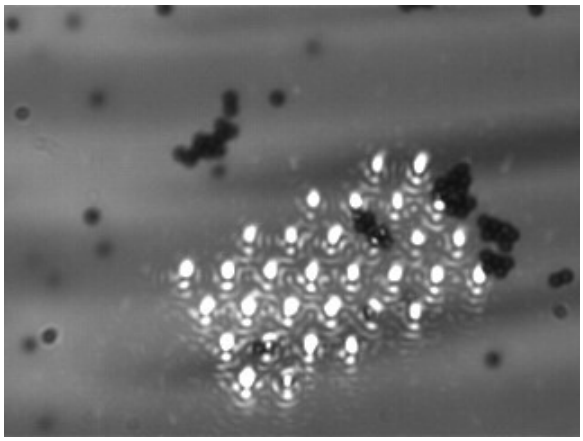

(Fig. 6.4.2-1b)

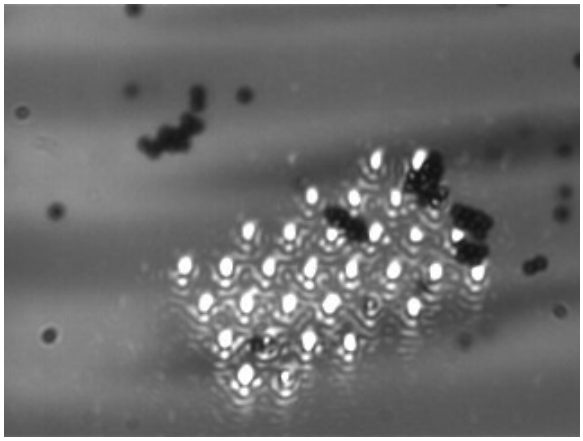

(Fig. 6.4.2-1c)

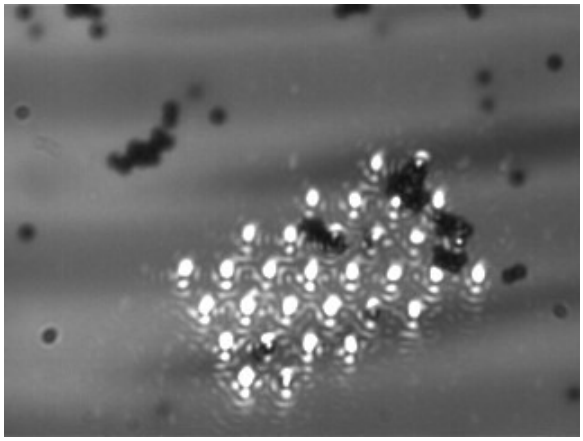

(Fig. 6.4.2-1d)

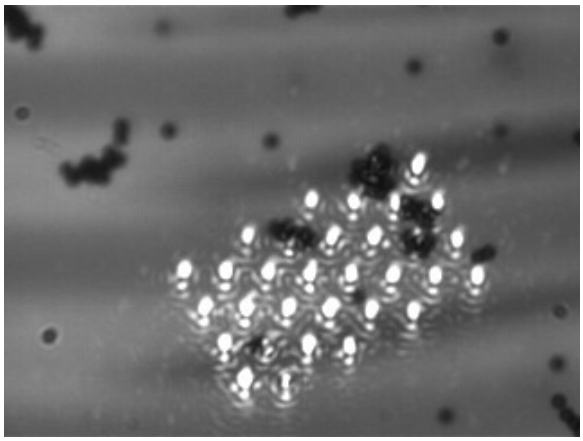

(Fig. 6.4.2-1e)

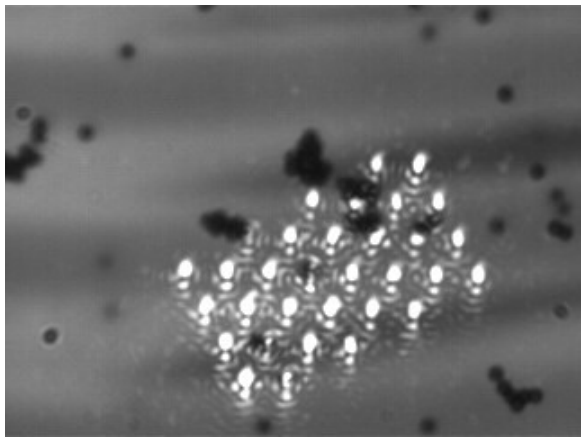

(Fig. 6.4.2-1f)

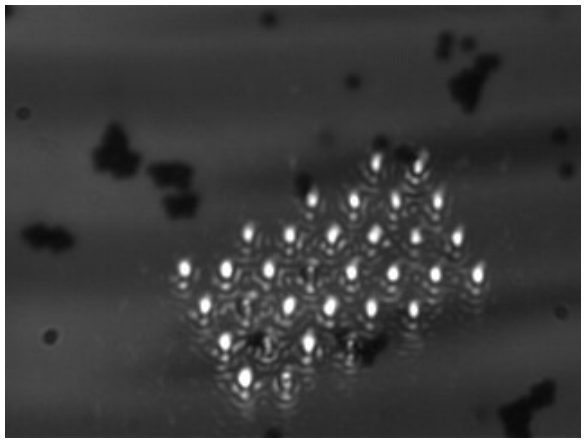

(Fig. 6.4.2-1g)

(Fig. 6.4.2-1 Multiple trapping via HOLO 7 over 65 seconds. 1.5 W half aperture.)

Figures 6.4.2-1a–g show trapping events occurring over 65 second duration. The laser beam power has been reduced to 1.5 W to observe if this reduction in power is still capable of trapping particles. While there are individual trapping events occurring over the duration, two particles have remained trapped (in lower-left traps) for the entire period. In Fig. 6.4.2-1g, the

camera exposure has been decreased to highlight the trapped particles and several trapping events can be seen. It is noted that there is increased clustering of particles compared to previous images, which is typical behaviour of polystyrene particles over time. Particles are moving in a westerly direction.

Although the polystyrene particles can be trapped in a multiple light field with a (relatively) low initial beam power of 1.5 W, it is rather difficult to achieve this consistently. Therefore, beam powers in the order of 1.65 W and above are recommended for this setup. Referring to the power measurements in the previous chapter, the power in each of the traps would only be in the order of hundreds of microwatts and possibly no greater than 0.5 mW.

It was surprising that trapping was successful using the random phase method. From previous results, it appeared that the light field lost its structure as the *d* value decreased. While the spots are not as focused compared to the uniform phase method, they are more intense, allowing for the traps to overcome some of these focal limitations. Still, the random phase method is not appropriate for small *d* values (less than 5 μm) due to the severe aberrations inherent in this method. This is primarily due to the unevenness in the thickness of the film being used, to which the random phase method is more susceptible.

6.4.3) Trapping Movies

Short movies were made in order to show trapping events occurring over a period of time (recorded on CD-ROM, Appendix E). Single frames are shown in Fig. 6.4.3). Since the Mightex camera does not record in movie mode, individual images were captured sequentially (with a time separation of 1 second) and using MS Windows Movie Maker, a short movie was created. The laser power was 1.8 W with a half aperture setting. While the light field was able to trap particles fairly easily at this power, the traps could still escape as evident in Polyvid.1a when convection currents became too strong.

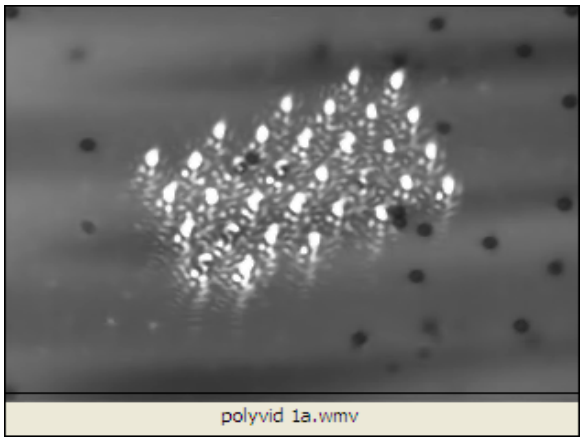

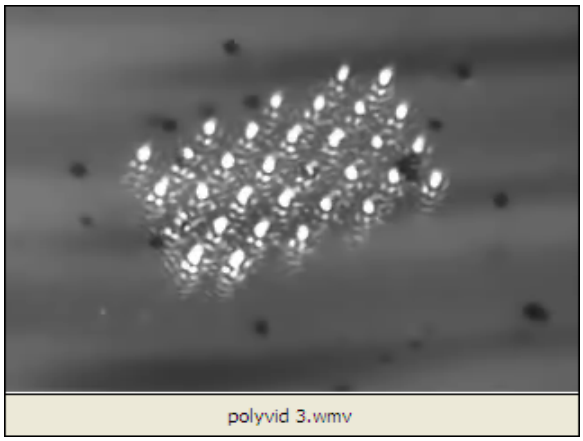

7) Conclusion & Further Work

1. It has been shown that trapping with small sized particles (~2.5 μm) can be achieved with the current trapping arrangement. As mentioned previously, this was the first time that trapping of particles with holographic light fields was achieved at RMIT. The generated light fields are able to trap small PMMA particles in water, however this was difficult and the clusters of PMMA encased in decalin were observed to be easier to trap. The multiple series of images in Figs. 6.2.1-2, 6.2.1-3 and 6.2.4-1 demonstrate trapping of these clusters. While difficult; the trapping of small PMMA particles was achieved as Figs. 6.2.1-4 and 6.2.5-2a demonstrate. Trapping of these particles (via HOLO 3) was accomplished with a relatively low initial beam power of 1.35 W and with a reduced portion of the hologram exposed (third aperture). According to the power measurement results in chapter 5.4, this would correspond to power in each trap being in the order of ~ 0.5 mW, which is a low trapping power compared to 1 mW which is commonly used in other trapping arrangements reported in the literature.

   The polystyrene particles, with their higher refractive index (1.52, compared to 1.49 for PMMA) were less difficult to trap. Ideally, smaller particles (in the order of 1 μm and smaller) are desired for colloidal studies. 1 μm polystyrene particles were investigated but it was found that the light fields could not trap them, meaning that the gradient forces were not strong enough to overcome scattering forces and other factors such as the Stokes drag force and convection currents. This is partially due to the rather broad foci of the traps as particles of this size usually require a high numerical aperture lens to be successfully trapped, along with the relatively low trapping power of each trap. A tightly-focused trap with higher associated power density would overcome this. Larger sized polystyrene particles (2.5 μm) were able to be trapped with trapping arrangement via HOLO 3 and HOLO 7 as evident in the series of images in Figs. 6.3.1-1, 6.3.2-2, 6.4.1-1 and 6.4.2-1.

2. A 50 mm camera lens is capable of being used as the focusing optics for optical tweezers despite its relatively low numerical aperture. This is significant as it shows

that trapping setups are not limited to using high NA microscope-objectives (along with associated shallow working depths) thus opening up the sample volume that can be explored. It is suitable for single beam trapping or it can be combined with CGHs to form multiple tweezers for trapping. However, the low NA of the lens does limit the range of particle sizes that can be successfully trapped. While the system was able to successfully trap and isolate polystyrene particles of 2.5 μm diameter, particles of 1 μm could not be trapped. The estimated power per trap varied between ~1 mW (using HOLO 3) and ~ 0.15 mW (using HOLO 7). Of course, this value will vary when the initial beam power is changed along with the aperture settings. That trapping could occur at these low powers is significant for a low NA lens.

A rudimentary technique for determining and correcting the amount of spherical aberration present in the lens was successfully implemented and holograms generated with the modified lens function to account for this, along with the introduction of index matching, showed an improvement in quality over previous holograms when comparing the images in chapter 5.3.2 to hologram images in previous sections. The main limitation affecting the quality of the traps however; is still the phase nonuniformities in the film.

3. One of the achievements of this thesis was the ability to use Kodalith film for micro-holographic purposes. It is believed that this is the first time that this film has been implemented for optical trapping purposes. The high contrast film is usually used in black and white graphic applications and was not designed for holographic purposes. However, because of its high contrast, the film could be useful for reproducing binary holograms where the patterns are distinctly black and white. The film was able to reproduce the diffraction patterns generated via the random phase method with a lot more ease due to the more uniform contrast of these patterns compared to the ones produced via the uniform phase method due to the high dynamic range associated with uniform phase diffraction patterns. This results in a high degree of tonality which Kodalith cannot accurately reproduce. Therefore, random phase type patterns are recommended for this film but, as demonstrated in Figs. 5.2.4-4b, 5.2.4-6b, 5.3.1b-2b and 5.3.2b-2 in Chapter 5, light fields generated by this method break down at low *d*

values. It is believed that this is caused by the unevenness in the film thickness which adds a phase perturbation to the beam, preventing the light points from focusing properly at their allocated co-ordinates. This effect is magnified when the entire hologram is exposed to light, thus the best results were obtained at half apertures or below. The uniform phase method also suffers from this unevenness in the film, but is more tolerant of variations in phase across the hologram. The downside to this method is the high dynamic range associated with the diffraction patterns which affects the efficiency of the hologram. The overall efficiency of each method is quite low due to the fact that both methods produce amplitude holograms.

4. The point source coding scheme employing first principles was successful in calculating and generating structured light fields for optical trapping experiments. The coding was able to correctly position the point sources in their desired x ,y and z coordinates, and was quite capable of calculating a large number of points in a short time frame (approx. 29 seconds for 32 points). One of the disadvantages of this method was the relatively poor contrast in the principal fringes in the associated diffraction pattern. This was more evident in the uniform phase method and this affected the overall efficiency of this method compared to the random method. Introducing a limited amount of clipping alleviated some these problems but too much clipping gave rise to unwanted 'ghost' images as evident in the images in chapter sections 5.2.1 to 5.2.4.

Overall, the setup and its various contributing factors did allow for multiple optical trapping of particles; however it is felt that this novel setup is quite limited in conducting research associated with optical trapping, such as colloidal crystallisation which was one of the original aims of the project. Still, the setup would be quite useful in demonstrating the principles of HOT, such as in an undergraduate physics laboratory as the components are common, relatively inexpensive and the trapping arrangement can be constructed on standard optical benches.

Further Work

To improve the quality of the holographic light fields, further experimentation is required. Different bleaching techniques with the Kodalith film could be investigated as this has the potential of increasing hologram efficiency thus resulting in greater power per trap. Alternatively, holographic film or holographic plates could be used as a substitute to the Kodalith film, which could eliminate some of the concerns due to the unevenness in optical thickness of the current film although holographic film and plates are not necessarily much better as far as uniformity goes. Also alternatives to the printer/paper combination for the generation of diffraction patterns, such as electron-beam lithography could be implemented. Alternatively, different coding schemes, such as those based on iterative Fourier Transforms (IFTs) could be investigated as a method of improving the quality of the light fields. Modifying the coding scheme to account for refractive index differences (i.e. beam passing from air –glass – solution) in the trapping plane may be able to improve each individual trap's performance. This compensation was not attempted due to time constraints.

With regard to improving the power efficiency in the optical train, the 4x microscope-objective could be replaced with a 2x in the beam expander arrangement as there is some light loss in the current arrangement due to the slight overfilling of the camera lens aperture by the beam. Also, the hologram holder further reduces the amount of beam power available as it blocks a significant portion of the expanded beam. Thus implementing a smaller, initial collimated beam could overcome this; however a beam of lower divergence will have a larger irradiance variation over the face of the hologram which may introduce other errors. The substitution of the open glass well slides with one that has a closed well would be suitable for more stable trapping experiments as interference from air currents and vibrations could be reduced to an extent.

These improvements would lead to a trapping configuration suitable for undergraduate laboratory experiments. For more rigorous trapping experiments, such as colloidal crystallisation and dynamic trapping, a spatial light modulator combined with a high NA objective is recommended, however this will substantially increase the cost associated with the trapping arrangement. Alternatively, an electron-beam etched phase mask on an optically flat substrate could be substituted instead.

Appendix A: Hologram Calculations

This Appendix presents a number of equations relevant to calculations that had to be performed when considering the creation and reconstruction of the holograms. These included calculations needed for applying a spherical phase factor to the hologram, determining the minimum distance of focus of the hologram, the minimum resolvable depth of field, and the minimum and maximum resolvable point source separations.

A.1 Spherical Lens Function

When calculating near-field type holograms, it is useful to apply a spherical phase function, corresponding to a well corrected lens, to control the distance from the hologram at which the image is focused. The equation used to calculate the complex amplitude of each point source; given by:

$$H = A\left(\frac{Z}{r}\right)\exp^{-ikr} \qquad \textbf{Eq.a1}$$

gives a phase variation which becomes more negative away from the centre of the hologram plane. This corresponds to a wave diverging in the $+z$ direction. A collimated reference beam is added to form the hologram. If this hologram is then reilluminated in the reverse direction, it will focus light back to the position of the point source. However, if the distance from hologram to focus is small, then phase varies rapidly across the hologram and the hologram needs to be calculated and recorded at very high spatial resolution to avoid under-sampling and aliasing. Therefore, to focus the points using just the hologram acting as a lens requires the use of large array sizes (see appendix A.2) and high resolution reproduction. This is impractical so in practice, an optical lens can be used to perform most of the focusing function. However, the beam convergence in Eq.a1 needs to be cancelled out for this to occur. The lens function is designed to cancel out most of this variation in phase, leaving just the phase variation between the individual point sources. This means that the lens function has to apply a phase which becomes more positive away from the centre.

The lens phase function is thus:

$$H = \exp^{ikr} \qquad \textbf{Eq.a2}$$

where $r = \sqrt{x^2 + y^2 + f^2}$, f is the focal length of the lens, x and y are the coordinates of the optical axis of the lens and the wave number $k = 2\pi / \lambda$. Hence, the phase at every point in the hologram plane can be calculated.

However, the Asahi Super Takuma 50mm camera lens is not perfect and introduces spherical aberrations in the final image. Therefore, the lens function has to be modified to take this into account with the new lens function being:

$$H_c = \exp^{ikr'} \qquad \textbf{Eq.a3}$$

$$\text{where } r' = r + ar_1^4 + br_1^6 \qquad \textbf{Eq.a4}$$

with $r = \sqrt{x^2 + y^2 + f^2}$ and $r_1 = \sqrt{x^2 + y^2}$ respectively. The aberration coefficients a and b are calculated from phase curvature measurements of the camera lens using an interferometric technique. (See chapter 5.3 and appendix A.6)

A.2 Minimum Distance to Focus and Depth of Field

The phase variation represented by Eq. a1 varies more rapidly across the hologram the further one goes from the axis of the point source. To avoid aliasing, the phase change from one pixel to the next should be less than π radians. This condition will be most critical near the outer edge of the hologram.

The actual physical size of the hologram is given by $M\,dx \times N\,dy$ where M and N are the array dimensions while dx and dy are the pixel width and height. For a square array, these values will be equal to each other. For a point source located on axis but located at a distance z from the hologram plane, the distance to the edge of the hologram is just

$$r = \sqrt{z^2 + \left(\frac{1}{2}Mdx\right)^2} \qquad \textbf{Eq.a5}$$

$$\approx z\left(1 + \frac{1}{2}\left(\frac{1}{2}M\frac{dx}{z}\right)^2\right) \qquad \textbf{Eq.a6}$$

$$= z + \frac{1}{8}M^2\frac{dx^2}{z} \qquad \textbf{Eq.a7}$$

For the closest resolvable z distance, the difference between r at $x = \frac{Mdx}{2}$ and $x = \frac{(M-2)dx}{2}$ must be equal to λ. Due to the Nyquist Sampling criterion, the distance corresponding to one fringe (λ) cannot be smaller than two pixels. Thus the difference is:

$$\lambda = \frac{1}{8}M^2\frac{dx^2}{z} - \frac{1}{8}(M-2)^2\frac{dx^2}{z} \qquad \textbf{Eq.a8}$$

$$\lambda = \frac{1}{8}M^2\frac{dx^2}{z} - \frac{1}{8}(M^2-4M+4)\frac{dx^2}{z} \qquad \textbf{Eq.a9}$$

$$\lambda \approx \frac{1}{2}\frac{Mdx^2}{z} \qquad \textbf{Eq.a10}$$

$$\therefore \quad z = \frac{Mdx^2}{2\lambda}. \qquad \textbf{Eq.a11}$$

Putting in 1024 for M, 0.021 mm for dx (as $\frac{21.5\text{ mm}}{1024} = 0.021\text{ mm}$) and 514.5×10^{-6} mm for λ, gives a minimum z distance of 440 mm. Therefore, an object point must be no closer than 440 mm from the hologram plane. This condition holds if the hologram alone was being used to focus the image. The hologram requirements for focusing at 50 mm become too severe, hence the use of an optical lens to perform most of the focusing, and the extra phase term in the coding procedure to compensate for the use of the lens. A camera lens with a focal length of 50 mm is being used during reconstruction, and the focused points are located close to 50 mm from the hologram plane. This avoids any aliasing problems.

Depth of Field

To resolve a change in the distance of an object from the hologram plane, the corresponding change in phase between the centre and edge of the hologram needs to be at least half a cycle. In general, r is given by $r \approx z + \frac{x^2}{2z}$. The change in r from the centre ($x = 0$) out to distance x is $\frac{x^2}{2z}$. Taking the derivative gives:

$$|dr| = \frac{x^2}{2z^2}dz \qquad \textbf{Eq.a12}$$

$$dz = \frac{2z^2|dr|}{x^2} \qquad \textbf{Eq.a13}$$

Since $x = \frac{Mdx}{2}$ and $dr = \frac{1}{2}\lambda$, dz is now:

$$dz = \frac{4\lambda}{M^2 dx^2} z^2 \qquad \textbf{Eq.a14}$$

For a square sized array (M =1024, dx =0.021 mm), z at 50 mm from the hologram plane has a minimum depth of field of ≈11.5 μm, meaning points have to be separated by this amount for 3D effects to be resolved. At z = 100 mm, the minimum depth of field is increased to ≈ 45 μm. If the change in z between two points is smaller than these distances, their depth separation will not be resolvable. This means suitable care has to be taken when constructing true 3D holograms. It was found that for 3D effects to be clearly noticeable in practice, in the presence of other aberrations, the separation in depth needed to be ≈ 25 μm, approximately double the theoretical calculation, at z = 50 mm.

A.3 Minimum and Maximum Point source Separation

When using the point source methods, care has to be taken in choosing the separation between sources. Two point sources separated by a distance Δx in the x direction will produce interference fringes with a spacing of ΔX in the hologram plane, where

$$\Delta x \Delta X = \lambda z \qquad \textbf{Eq.a15}$$

For the two points to be resolved, ΔX must be no larger than the total width of the hologram $M\,dx$.

i.e. $$\Delta X = \frac{\lambda z}{\Delta x} \le Mdx \qquad \textbf{Eq.a16}$$

$$\therefore \Delta x_{\min} \ge \frac{\lambda z}{Mdx} \qquad \textbf{Eq.a17}$$

In our case, $M\,dx$ = 21.5 mm. At a distance of z = 50 mm, the minimum resolvable separation is Δx_{min} = 1.2 μm. At z = 60 mm, Δx_{min} is now = 1.44 μm.

On the other hand, to satisfy the Nyquist sampling criterion, ΔX must be at least two pixels in the hologram plane:

i.e. $$\Delta X = \frac{\lambda z}{\Delta x} \geq 2dx \qquad \textbf{Eq.a18}$$

$$\therefore \Delta x_{\max} \leq \frac{\lambda z}{2dx} \qquad \textbf{Eq.a19}$$

Again using z = 50 mm gives a maximum allowable point separation of 0.61 mm or an angle independent of distance of:

$$\frac{\Delta x_{\max}}{z} = \frac{\lambda}{2dx} \approx 0.012 \text{ radians} \qquad \textbf{Eq.a20}$$

which is equivalent to 0.76°. This restriction also applies to the separation between the reference beam and any of the points. Therefore, any point source arrays generated at z = 50 mm must not go beyond 0.61 mm from the optical axis in the x and y directions. It is obvious that the maximum separation (Δx_{max}) will therefore increase when z does.

A.4 Reference-less Beam Technique

A 'reference-less' beam method [79] was used in the generation of the holographic diffraction patterns. As the title implies, the method does not make explicit use of a reference beam, but only considers the real part of the complex amplitude with a positive bias added. The reasoning is as follows:

An object wave with a complex amplitude $F(u)$ is added with an on-axis, plane-wave, uniform amplitude reference beam, giving:

$$R + F(u) \qquad \textbf{Eq. a21}$$

where R is a real constant. The resulting power density on re-illumination is proportional to:

$$\left(R + F(u)\right)\left(R + F(u)\right)^* = R^2 + \left|F(u)\right|^2 + R\left(F(u) + F^*(u)\right) \qquad \textbf{Eq.a22}$$

Here $R^2 + \left|F(u)\right|^2$ is the power density in the direct beam and does not contribute to the primary image, leaving:

$$R\left(F(u) + F^*(u)\right) = 2R\,\mathrm{Re}\{F(u)\} \qquad \textbf{Eq.a23}$$

which is just proportional to the real part. To make sure that the power density in the simulated interference pattern remains positive, the following MATLAB code is used

```
t=real(a);
t1=min(min(t));
t2=t-t1;
```

The variable `t` takes the real part of the complex array `a` which is the total complex amplitude of the object and is in an n×n array. `t1` takes the most negative value of the array `t`. This value is then subtracted from `t`, hence biasing it positive, resulting in the final array `t2`. `t2` is the CGH of the object.

The benefits of this method are that it uses less code than other beam methods and it does not shift the object on reconstruction. There is no significant difference in image quality when using this method and thus, this method was used in the coding of the holograms. In fact, this method should result in a cleaner reconstruction because the $|F(u)|^2$ term, which represents noise around the direction of the direct beam, is ignored.

A.5 Numerical Aperture and F-number considerations

It is important to ensure that the microscope objective lens used for viewing holographic reconstructions and trapping experiments has at a minimum the same Numerical Aperture as the 50 mm camera lens in the optical setup. Otherwise loss of resolution in the viewing will occur as not all light passing from the camera lens will be captured by the microscope-objective lens. The Numerical Aperture (*NA)* required can be worked out from the F- number ($F_{\#}$) of the 50 mm lens. $F_{\#}$ is given by: $F_{\#} = \frac{f}{d}$ where f is the focal length of the lens and d is the maximum aperture diameter of the lens, which for the camera lens are 50 mm and 35 mm respectively. Thus $F_{\#} = 1.43$ which would correspond to *f/1.4* in photographic terms.

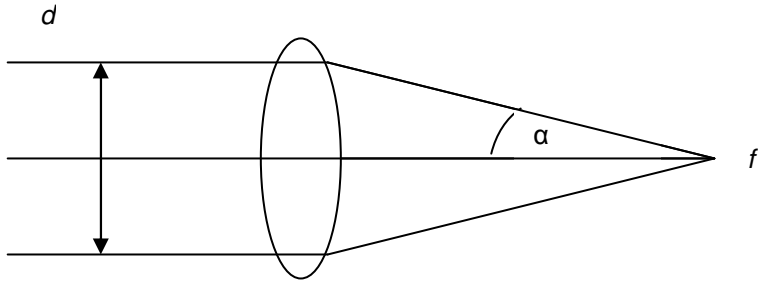

(Fig. A.1)

The numerical aperture of a lens is given by (Fig. A1):

$$NA = n\sin\alpha \qquad \textbf{Eq.a24}$$

where n is the refractive index of the medium (1.00 for air) and sin α is equal to:

$$\sin\alpha = \frac{\frac{d}{2}}{\sqrt{f^2 + \left(\frac{d}{2}\right)^2}} = \frac{1}{\sqrt{4\left(\frac{f^2}{d^2}\right)+1}} \qquad \textbf{Eq.a25}$$

$$\therefore NA = \frac{1}{\sqrt{4F_{\#}^2 + 1}} \qquad \textbf{Eq.a26}$$

This gives a value of NA = 0.33 when substituting in the $F_{\#}$ value of the 50 mm lens. If the numerical aperture of the lens is known, $F_{\#}$ is simply:

$$F_{\#} = \frac{1}{2}\sqrt{\frac{1}{NA^2} - 1} \qquad \textbf{Eq.a27}$$

The numerical aperture of the 40x Zeiss microscope is given as 0.85 so substituting this value into eq.a27 yields an $F_{\#}$ value of 0.31. Therefore the 40x microscope objective lens is able to capture all the light coming from the 50 mm lens without any loss of resolution. However, the 10x objective used in some initial experiments had NA = 0.22, and so it would not be able to fully resolve detail produced by the hologram/camera lens combination.

Appendix B: Spherical Aberration in 50mm Camera Lens

The resultant graphs for both horizontal and vertical fringe measurements are shown in Graphs B1-B6; which are taken from the results in Table 5.3 in chapter 5.3.

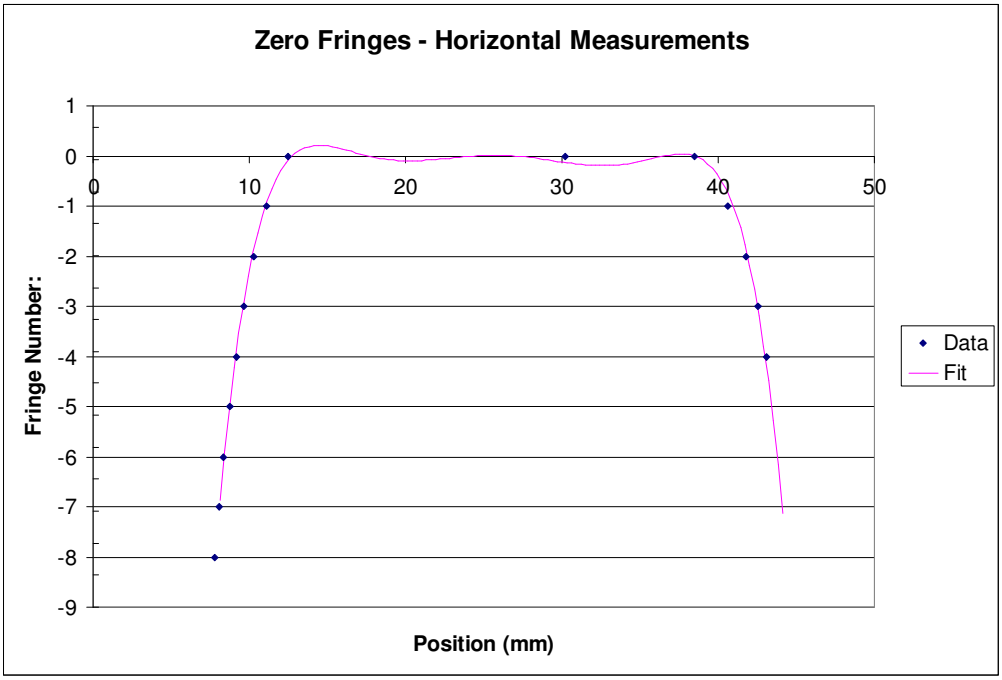

(Fig. B1 Horizontal fringe measurements with central focal point.)

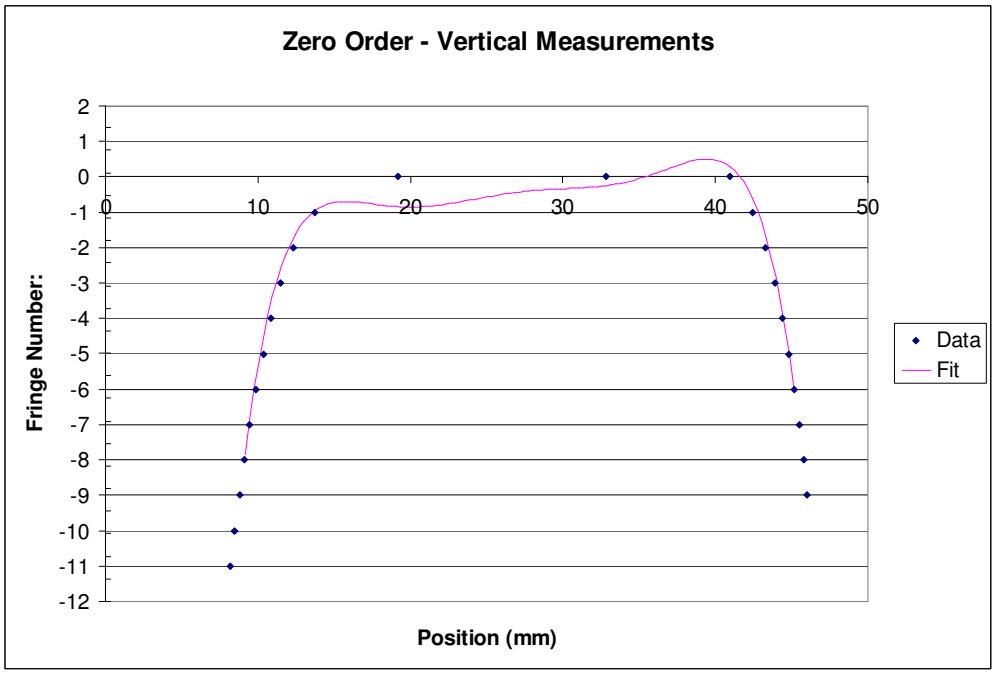

(Fig. B2 Vertical fringe measurements with central focal point.)

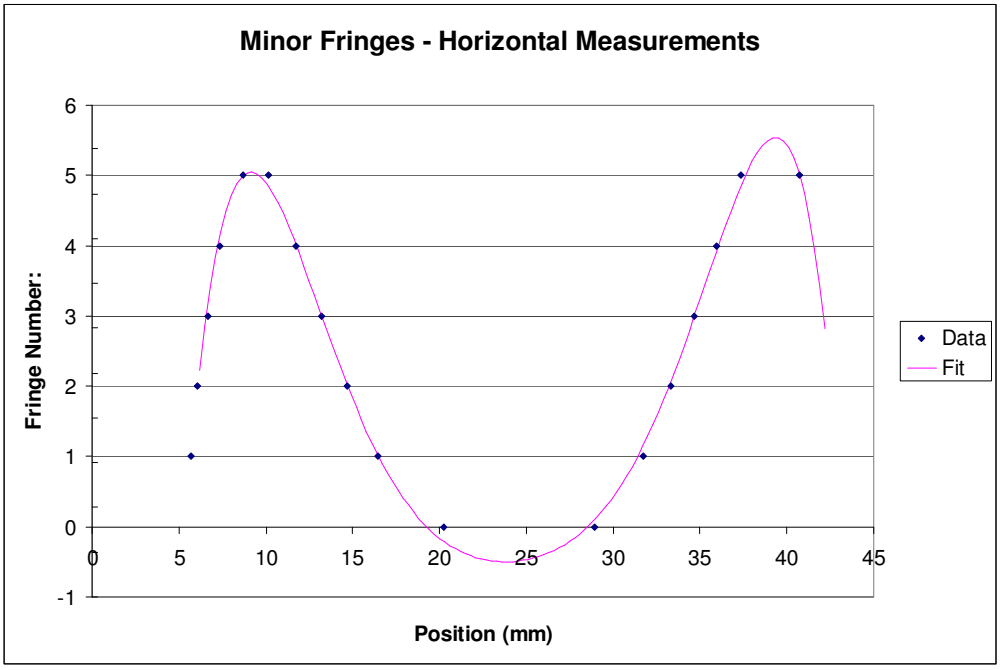

(Fig. B3 Horizontal measurements with 6 fringe defocus.**)**

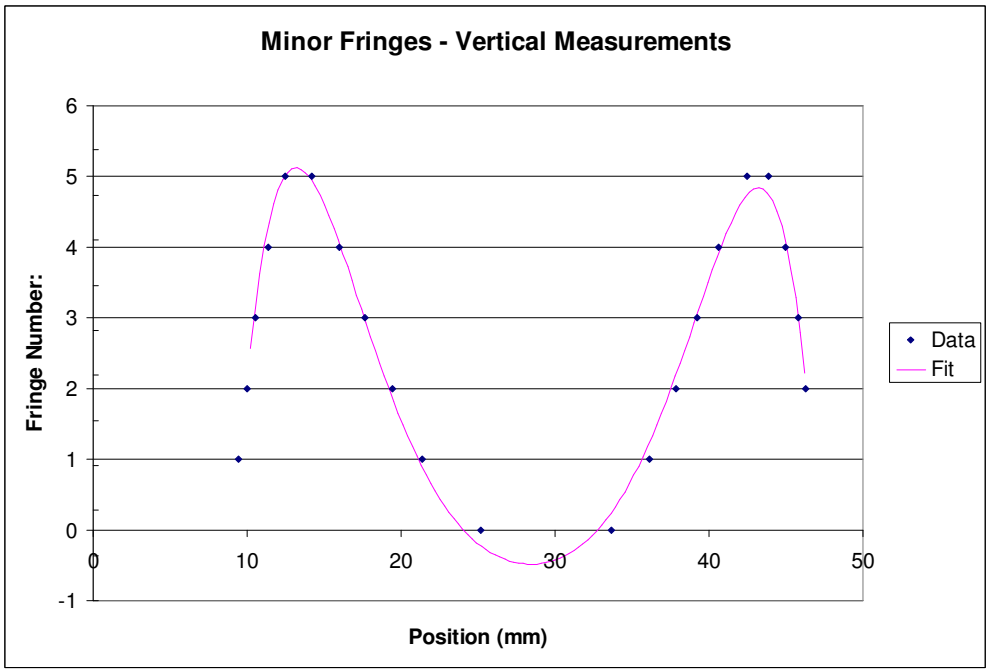

(Fig. B4 Vertical measurements with 6 fringe defocus.**)**

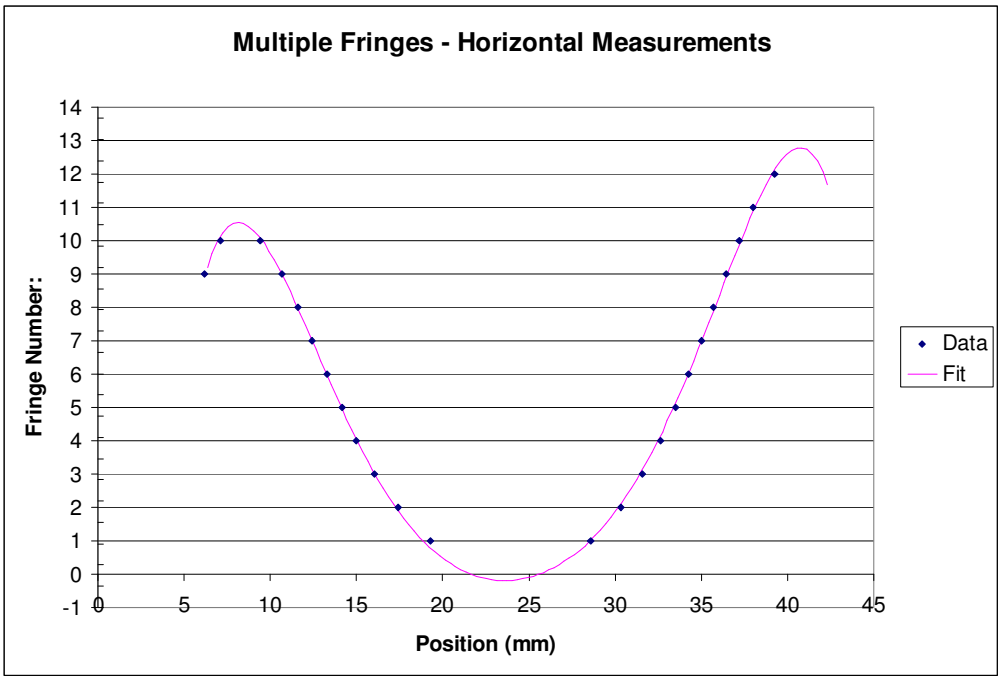

(**Fig. B5** Horizontal measurements with 12 fringe defocus.)

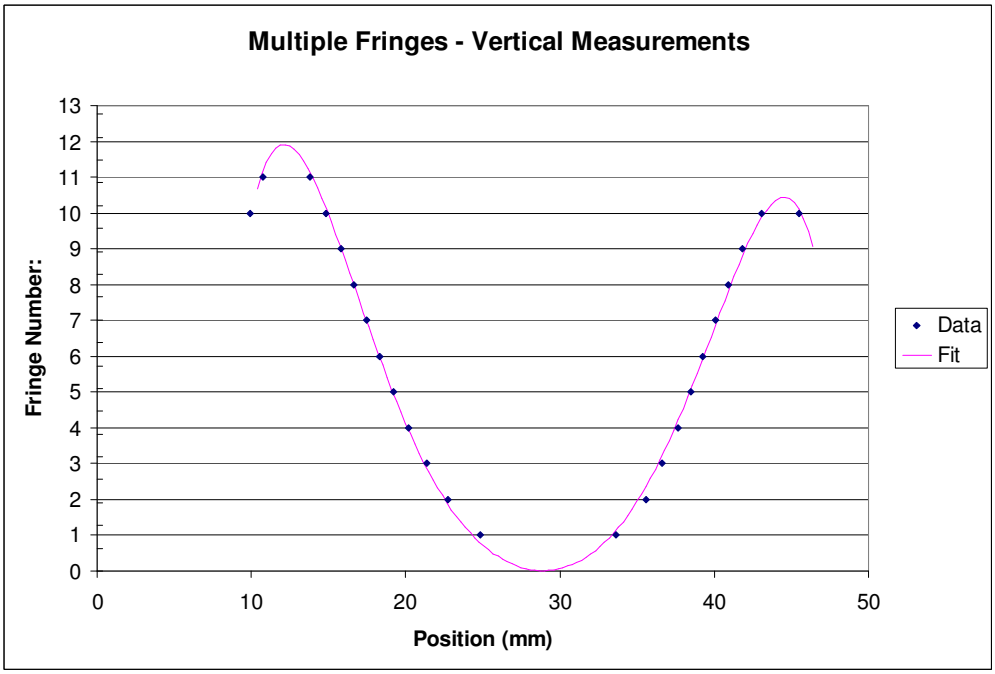

(**Fig. B6** Vertical measurements with 12 fringe defocus.)

Appendix C: Program Source Codes

Many MATLAB programs and functions were created over the course of this project, through trial and error and by exploring alternative ideas. Listed below are the main programs and their associated functions used in generating the diffraction pattern output.

M-File subroutines:

Clip.m

The *clip.m* function clips the values of a particular array. It is used in adjusting the output of the diffraction patterns so that the contrast between light and dark points is relatively even. For it to work successfully, the diffraction pattern must be scaled between zero and one. However too much clipping can be detrimental to the final hologram and can lead to increases in the efficiencies of the higher diffraction orders and increased ghost images.

```
function A = clip(B,minm,maxm);
A = min(B,maxm*ones(size(B)));
        A = max(A,minm*ones(size(A)));
```

Diffract.m

The *diffract.m* performs the 2D Fast Fourier Transform on a particular array *A* and returned a complex array *B*.

```
function B = diffract(A)
% DIFFRACT calculates 2-D Fourier Transform of image
% Returns Discrete Fourier Transform centered on center of matrix

B = fftshift(A);
B = fft2(B);
B = fftshift(B);
```

This function is used when wishing to view the simulated output of the final array *t*. This function is used in the form of:

```
d=diffract(t);
d1=(abs(d).^2);
d1(xpos1:xpos2,ypos1:ypos2)=0;
imagesc(d1);
```

Appendix C

Lensph.m

This function is used to simulate a spherical phase function. When used in conjunction with the Cubeke function, it effectively focuses the image at infinity. This is desired as the focusing of the hologram is too coarse and a 50mm camera lens will be used to focus the image at the desired z distance in the experimental set up. This function doesn't compensate for spherical aberrations present in the camera lens.

```
function H = lensph(Z)
M=1024;
N=1024;
xh=21.5/M;
yh=21.5/N;
x0=-10.75+xh;
y0=-10.75+yh;
wvl=514.5e-6;


% function H = lensph(Z)
% generates spherical phase function corresponding to a well-corrected lens
% Z in mm, > 0 produces converging lens, < 0 diverging optical axis is centred on x = y = 0
% Formula is  H = exp{ikr)
% where r is distance between (0,0,Z) and (x,y,0) in hologram plane and k is the wavenumber

ik = 2*i*pi/wvl;
[x,y] = ndgrid(x0:xh:x0+(M-1)*xh, y0:yh:y0+(N-1)*yh);
r = sqrt(x.^2 + y.^2 + Z.^2);
H = exp(ik*r);
```

Lensphcorr.m

This function is used to simulate a corrected spherical phase function. When used in conjunction with the *Cubeke* function, it effectively focuses the image at infinity. It tries to compensate for the spherical aberration present in the 50mm camera used in the experimental set up. It operates on the same principal as *lensph.*

```
function H = lensphcorr(Z)

M=1024;
N=1024;
xh=21.5/M;
yh=21.5/N;
x0=-10.75+xh;
y0=-10.75+yh;
wvl=514.5e-6;
a = -7.86e-8;
b = 3.046e-10;
```

```
%  function H = lensphcorr(Z)
% generates spherical phase function corresponding to a well-corrected lens
% Z in mm, > 0 produces converging lens, < 0 diverging
% optical axis is centred on x = y = 0
% Formula is  H = exp{ikrr)
% where r is distance between (0,0,Z) and (x,y,0) in hologram plane
%and k is the wavenumber
%introduces r^4 & r^6 coefficients to counter aberrations in lens

ik = 2*i*pi/wvl;
[x,y] = ndgrid(x0:xh:x0+(M-1)*xh, y0:yh:y0+(N-1)*yh);
r = sqrt(x.^2 + y.^2 + Z.^2);
r1 = sqrt(x.^2 + y.^2);
rr = r + a*r1.^4 + b*r1.^6;
H = exp(ik*rr);
```

Spheric.m

This function is an integral component of the main program codes. It calculates the complex amplitude of an isotropic point source. The variables X,Y,Z are passed into the function and relate to the coordinate of the point source being calculated. The variables [x,y] relate to the x,y coordinates on the hologram plane. This is different to the point source coordinates. The other variables; A, wvl, x0, xh, y0, yh, M and N are constants (see *Cubeka* & *CubeNa*).

```
function H = spheric(A,X,Y,Z,wvl,x0,xh,y0,yh,M,N)

%  function H = spheric(A,X,Y,Z)
%  Calculates the complex amplitude on the hologram plane
%  due to a point source of relative strength A at coordinates X,Y,Z (in mm)
%  using exact isotropic spherical wave calculation
%  normalised so that amplitude is A at point (x,y) = (X,Y)
%  A is set to 1
%  Formula is  H = A*(Z/r)*exp{-ikr)
%    where r is distance between (X,Y,Z) and (x,y,0) in hologram plane and k is the wavenumber

ik = 2*i*pi/wvl;
[x,y] = ndgrid(x0:xh:x0+(M-1)*xh, y0:yh:y0+(N-1)*yh);
r = sqrt((x-X).^2 + (y-Y).^2 + Z.^2);
H = A*(Z./r).*exp(-ik*r);
```

Sphericrand.m

This function is essentially the same as the *spheric.m* function; the only difference is that it applies a random phase to the complex amplitude being generated. The random phase factor *exp(-ik*r1)* is applied to the spherical wave calculation. The variable r1 generates a random number thus ensuring a random phase is applied.

```
function H = sphericrand(A,X,Y,Z,wvl,x0,xh,y0,yh,M,N)

%  function H = spheric(A,X,Y,Z)
%  Calculates the complex amplitude on the hologram plane
%  due to a point source of relative strength A at coordinates X,Y,Z (in mm)
%  using exact isotropic spherical wave calculation
%  normalised so that amplitude is A at point (x,y) = (X,Y)
%  A is usually set to 1
%  Formula is  H = A*(Z/r)*exp{-ikr)
%  where r is distance between (X,Y,Z) and (x,y,0) in hologram plane and k is the wavenumber

r1=rand;
ik = 2*i*pi/wvl;
[x,y] = ndgrid(x0:xh:x0+(M-1)*xh, y0:yh:y0+(N-1)*yh);
r = sqrt((x-X).^2 + (y-Y).^2 + Z.^2);
H = A*(Z./r).*exp(-ik*r).*exp(-ik*r1);
```

Hexagonal Close Packed 'A' Plane – uniform phase.

This program is used to generate an array of point sources in a hexagonal structure focused at a specific *z* distance from the hologram plane. The *x,y* starting coordinates, the *d* spacing, the number of points and the *z* distance can be controlled by the user. The program will show the calculated diffraction pattern as an image on the screen.

```
%creating a hexagonal array of points
%xpos, ypos = initial x, y starting positions (in mm)
%d= d spacing between points
%numpoints = number of light sources in a single row.  Total points = (numpoints^2 x2)
%z = z starting position (in mm)
%wvl = wavelength used (in mm)
%M,N = array size used
%xh, yh = actual hologram pixel dimensions (in mm)
%x0, y0 = hologram starting position
%makes use of a modified lens function

function t2 = Cubeke(xpos,ypos,d,n,z)
M=1024;
N=1024;
xh=21.5/M;
yh=21.5/N;
x0=-10.75+xh;
y0=-10.75+yh;
wvl=514.5e-6;
R=0;
R1=0;
R2=0;
xinc=1.73205081.*d;
xpos1=xpos+(0.866025403.*d);
ypos1=ypos-(0.5.*d);
yinc=d;
```

```
 for x = xpos:xinc:xpos+(n-1).*xinc;
    for y = ypos:yinc:ypos+(n-1).*yinc;
        R=R+spheric(1.,x,y,z,wvl,x0,xh,y0,yh,M,N);
   end;
end;
 for x1=xpos1:xinc:xpos1+(n-1).*xinc;
    for y1=ypos1:yinc:ypos1+(n-1).*yinc;
       R1=R1+spheric(1.,x1,y1,z,wvl,x0,xh,y0,yh,M,N);
     end;
  end;
    R2=R+R1;
    R3=R2.*lensphcorr(z);
    t=real(R3);
    t1=min(min(t));
    t2=t-t1;
    imagesc(t2);
    colormap(gray);
    axis square;
```

The single 'A' plane random phase code is nearly identical to the above source code except that the function *spheric* is replaced by *sphericrand*. This function is called *Cubekf.*

Hexagonal Close Packed 'ABC' Plane – uniform phase.

This program is used to generate an array of point sources in an 'A,B,C' hexagonal structure focused at a specific *z* distance from the hologram plane. The *x,y,z* starting coordinates, the *d* spacing, the number of points and the increment in *z* distance between the planes can be controlled by the user. The program will show the calculated diffraction pattern as an image on the screen.

```
% creating a hexagonal array of points
% xpos, ypos = initial x, y starting positions
% d= d spacing between points
% n= number of light sources in a single row.  Total points in a single plane = (numpoints^2 x2)
% z, zo, zo2 = initial z positions for 'A','B','C' planes (in mm)
% zinc = space between planes
% wvl = wavelength used (in mm)
% M,N = array size used
% xh, yh = actual hologram pixel dimensions (in mm)
% x0, y0 = hologram starting position

function R6 = CubeNe(xpos,ypos,d,n,z,zinc)
R=0;
R1=0;
R2=0;
R3=0;
R4=0;
R5=0;
R6=0;
M=1024;
```

```
N=1024;
xh=21.5/M;
yh=21.5/N;
x0=-10.75+xh;
y0=-10.75+yh;
wvl=514.5e-6;
xinc=1.73205081.*d;          %horizontal x-spacing between points
xpos1=xpos+(0.866025403.*d); %shifted horizontal spacing btw points
ypos1=ypos-(0.5.*d);         %shifted vertical spacing btw points
xpos2=xpos+(1.15470054.*d);  %B plane 1st shifted horizontal spacing
xpos3=xpos1-(0.57735027.*d); %B plane 2nd shifted horizontal spacing
xpos4=xpos+(0.5773527.*d);   %C plane 1st shifted horizontal spacing
xpos5=xpos1+(0.5773527.*d);  %C plane 2nd shifted horizontal spacing
zo1=z+zinc;                  %B plane start position
zo2=zo1+zinc;                %C plane start position
yinc=d;                      %vertical spacing btw points
  for x = xpos:xinc:xpos+(n-1).*xinc;
    for y = ypos:yinc:ypos+(n-1).*yinc;
        R=R+spheric(1.,x,y,z,wvl,x0,xh,y0,yh,M,N);
    end;
 end;
  for x1=xpos1:xinc:xpos1+(n-1).*xinc;
    for y1=ypos1:yinc:ypos1+(n-1).*yinc;
        R1=R1+spheric(1.,x1,y1,z,wvl,x0,xh,y0,yh,M,N);
    end;
  end;
    for x2=xpos2:xinc:xpos2+(n-1).*xinc;
      for y2=ypos:yinc:ypos+(n-1).*yinc;
          R2=R2+spheric(1.,x2,y2,zo1,wvl,x0,xh,y0,yh,M,N);
      end;
    end;
    for x3=xpos3:xinc:xpos3+(n-1).*xinc;
      for y3=ypos1:yinc:ypos1+(n-1).*yinc;
        R3=R3+spheric(1.,x3,y3,zo1,wvl,x0,xh,y0,yh,M,N);
      end;
    end;
   for x4=xpos4:xinc:xpos4+(n-1).*xinc;
      for y4=ypos:yinc:ypos+(n-1).*yinc;
        R4=R4+spheric(1.,x4,y4,zo2,wvl,x0,xh,y0,yh,M,N);
      end;
    end;
    for x5=xpos5:xinc:xpos5+(n-1).*xinc;
      for y5=ypos1:yinc:ypos1+(n-1).*yinc;
        R5=R5+spheric(1.,x5,y5,zo2,wvl,x0,xh,y0,yh,M,N);
      end;
    end;

  R6=R+R1+R2+R3+R4+R5;     %The 6 grid arrays are added to form 'A', 'B' and 'C' planes focused in different
z planes.
  R7=R6.*lensphcorr(z);
  t=real(R3);
  t1=min(min(t));
  t2=t-t1;
  imagesc(t2);
  colormap(gray);
  axis square;
```

The ‘A, B, C’ plane random phase code is nearly identical to the above source code except that the function *spheric* is replaced by *sphericrand*. This function is called *CubeNf.*

Testsph.

```
function s2 = Testsph(x,y,xpos,ypos,z)

x1=x+xpos;
x2=x-xpos;
y1=y+ypos;
y2=y-ypos;
r=Point(x,y1,z);    %(initial starting point
r1=r.*lensph(-z);
t=real(r1);
t1=min(min(t));
t2=t-t1;
maxt=max(max(t2));    %makes all values btw 0-1
t3=t2/maxt;
t3(1:386,1:1024)=0;   %This part will give E/W portion of hologram
t3(638:1024,1:1024)=0;
t3(387:637,251:773)=0;


r=Point(x,y,z);    % moves along for centre point
r1=r.*lensph(-z);
t=real(r1);
t1=min(min(t));
t2=t-t1;
maxt=max(max(t2));
t4=t2/maxt;
t4(1:386,1:1024)=0;
t4(638:1024,1:1024)=0;   %This for the centre part of hologram
t4(1:1024,1:386)=0;
t4(1:1024,638:1024)=0;


r=Point(x,y2,z);    % moves along for end point
r1=r.*lensph(-z);
t=real(r1);
t1=min(min(t));
t2=t-t1;
maxt=max(max(t2));
t5=t2/maxt;
t5(251:773,1:1024)=0;
t5(1:250,251:1024)=0;   %This for the NW/SE part of hologram
t5(774:1024,1:773)=0;


r=Point(x1,y,z);    % moves along centr and up one point
r1=r.*lensph(-z);
t=real(r1);
t1=min(min(t));
t2=t-t1;
maxt=max(max(t2));
```

```
t6=t2/maxt;
t6(251:773,1:1024)=0;
t6(1:1024,1:386)=0;   %This for the N/S part of hologram
t6(1:1024,638:1024)=0;


r=Point(x2,y,z);    % moves along centre and down one point
r1=r.*lensph(-z);
t=real(r1);
t1=min(min(t));
t2=t-t1;
maxt=max(max(t2));
t7=t2/maxt;
t7(251:773,1:1024)=0;
t7(1:250,1:773)=0;           %This for the NE/SW part of hologram
t7(774:1024,251:1024)=0;
S=t3+t4+t5+t6+t7;
maxs=max(max(S));
s1=S/maxs;
s2=1-s1;                     %this part inverts the values- background is now white
colormap(gray);
imagesc(s2);
```

This program is used to generate the *Testsph* test pattern. The individual holograms are generated in a 1024x1024 array, and the diffraction patterns are cut down so only two square portions (for example; the northwest and southeast) remain. The rest consists of a white background. These individual diffraction patterns are added together to form a final hologram.

TestPoint.

```
function S = Testb(x,y,xpos,ypos,z)
S=0;
x1=x+xpos;
x2=x+(xpos*2);

y1=y+ypos;
y2=y-ypos;

r=Point(x,y,z);      %(initial starting point
r1=Point(x1,y,z);
r2=Point(x2,y,z);
r3=Point(x1,y1,z);
r4=Point(x1,y2,z);
R=r+r1+r2+r3+r4;
R1=R.*lensph(-z);
t=real(R1);
t1=min(min(t));
S=t-t1;
```

This function is used to generate the *Testpoint* test pattern. This will generate five point sources on a single hologram.

Appendix D: Holographic Diffraction Patterns

The following diffraction patterns are smaller versions of the ones used to generate some of the light fields in this thesis. They only show a 256 × 256 portion of the entire array to show the principle fringe detail clearly. The printout dimensions of the entire pattern were 21 cm×21 cm.

HOLO 3

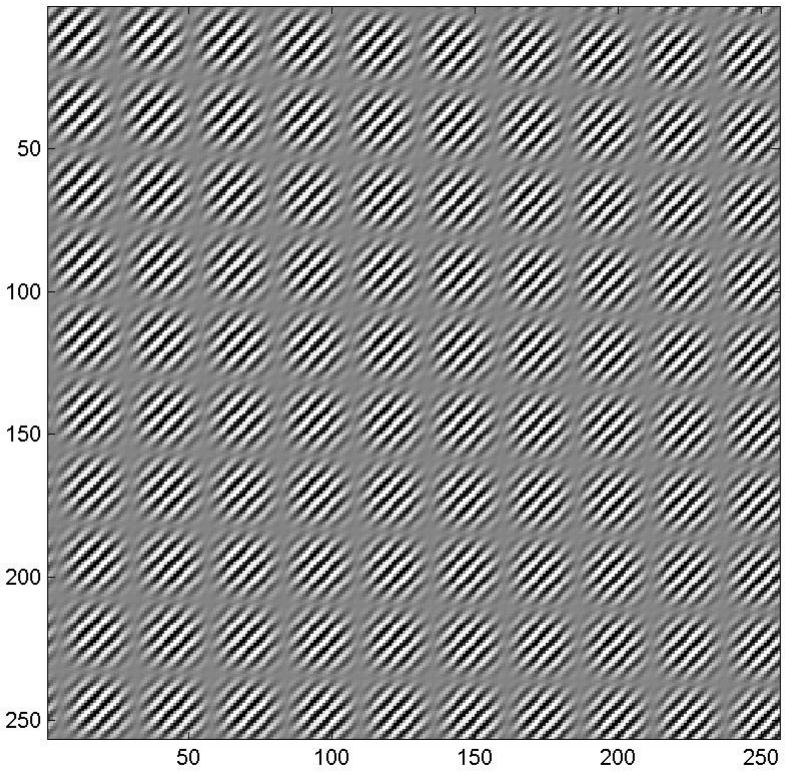

(**Fig. D1** HOLO 3 diffraction pattern.)

HOLO 5

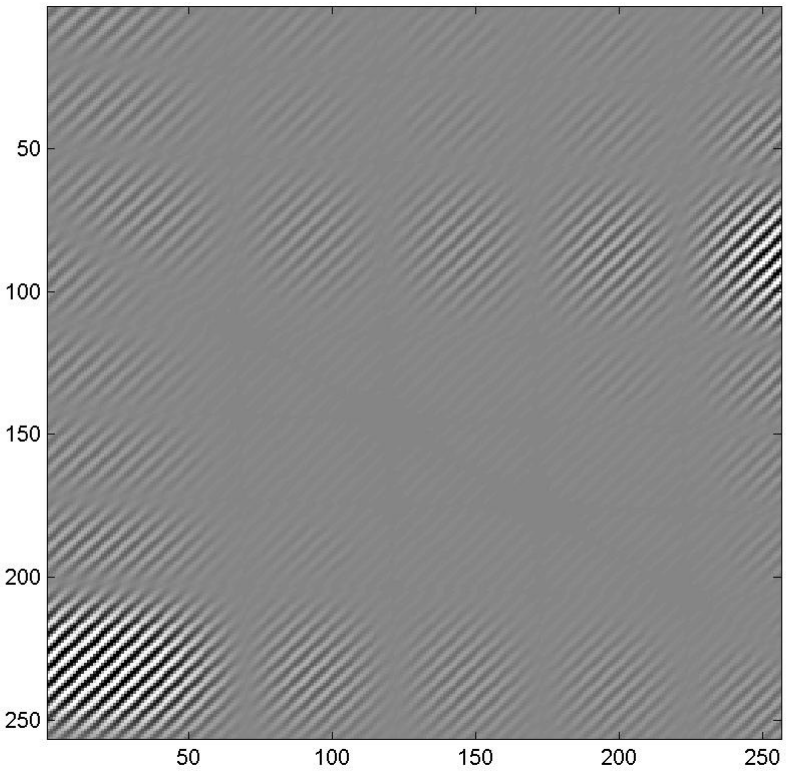

(**Fig. D2** HOLO 5 diffraction pattern.)

HOLO 6

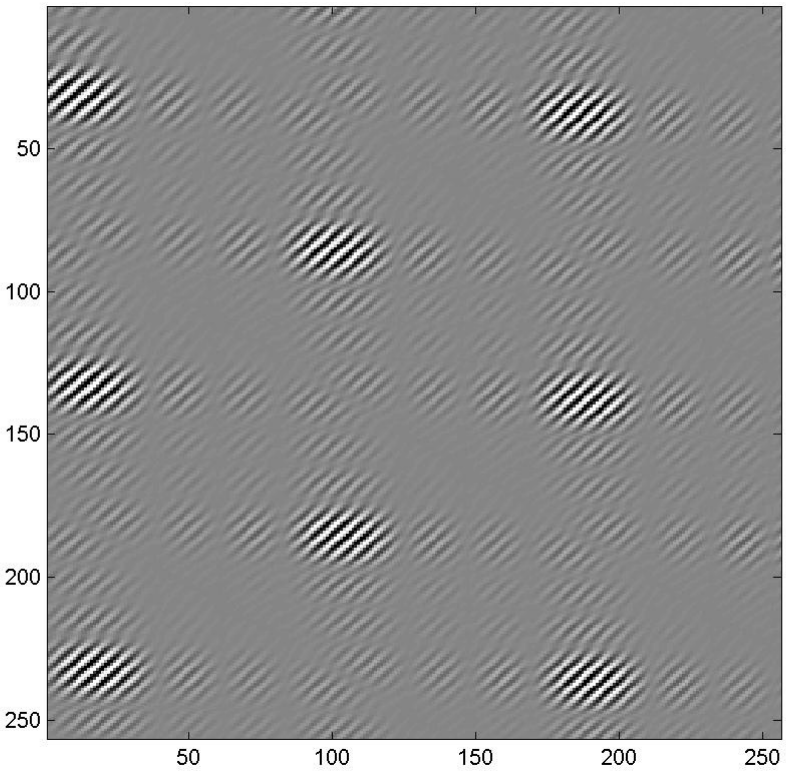

(**Fig. D3** HOLO 6 diffraction pattern.)

HOLO 7

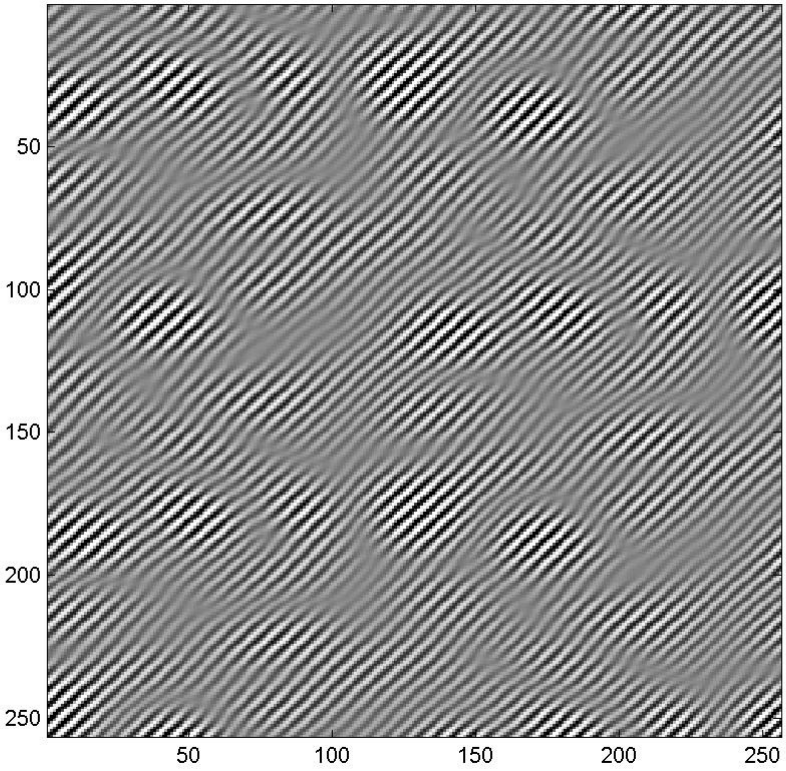

(**Fig. D4** HOLO 7 diffraction pattern.)

HOLO 12

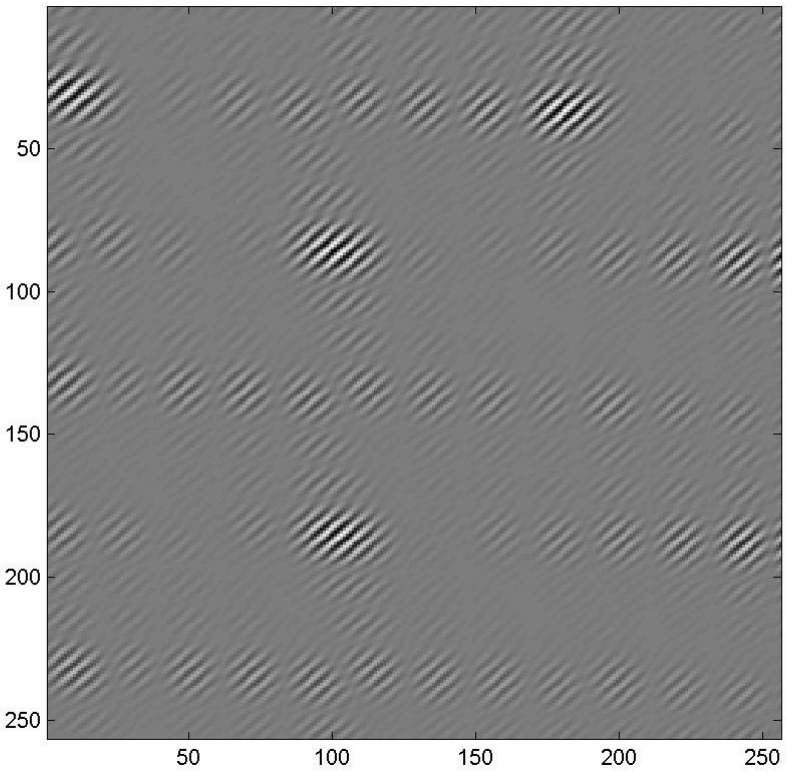

(Fig. D5 HOLO 12 diffraction pattern**.)**

HOLO 15

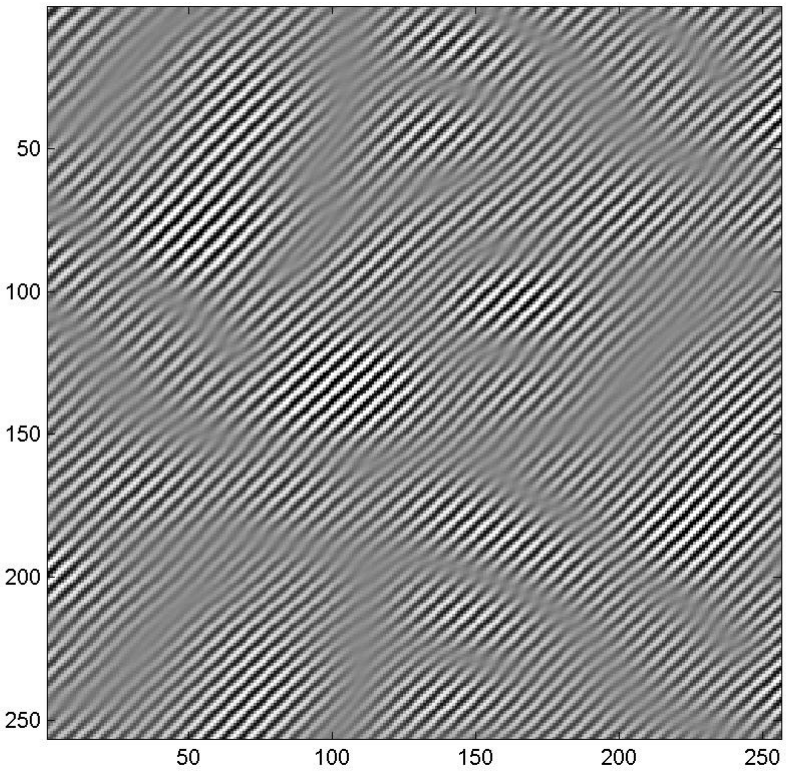

(Fig. D6 HOLO 15 diffraction pattern.)

References

1. Krauss, T.F. and R.M. De La Rue, *Photonic crystals in the optical regime - past present and future.* Progress in Quantum Electronics, 1999. **23**: p. 51-96.
2. Sharp, D.N., et al., *Photonic crystals for the visible spectrum by holographic lithography.* Optical and Quantum Electronics, 2002. **34**: p. 3-12.
3. Ashkin, A., *Optical Trapping and Manipulation of Neutral Particles Using Lasers: A Reprint Volume With Commentaries*. 2006: World Scientific Publishing.
4. Dholakia, K. and P. Reece, *Optical micromanipulation takes hold.* nanotoday, 2006. **1**(1): p. 18-26.
5. Grier, D.G. and Y. Roichmann, *Holographic optical trapping.* Applied Optics, 2005. **45**: p. 880-887.
6. Spalding, G.C., J. Courtial, and R. Di Leonardo, *Holographic optical tweezers*, in *Structured Light and its Applications: An Introduction to Phase-Structured Beams and Nanoscale Optical Forces*, D.L. Andrews, Editor. 2008, Elsevier Press.
7. Sun, B., Y. Roichmann, and D.G. Grier, *Theory of holographic optical trapping.* Optics Express, 2008. **16**: p. 15765-15776.
8. Hariharan, P., *Optical Holography: Principles, Techniques and Applications.* 2 ed. 1996: Cambridge University Press.
9. Frere, C., *Reconstruction in inclined planes of curved computer generated holograms.* Applied Optics, 1990. **29**(32): p. 4761-4765.
10. Nagashima, K., *3D computer generated holograms using 1D Fourier transform operations.* Optics & Laser Technology, 1998. **30**: p. 361-366.
11. Nagashima, K., *Improvement of reconstruction in 3D computer-generated holograms using 1D Fourier transform operations.* Optics & Laser Technology, 2001. **31**: p. 329-334.
12. Nagashima, K., *Improvement of 1D off-axis computer-generated holograms.* Optics & Laser Technology, 2002. **35**: p. 181-186.
13. Frere, C., D. Leseberg, and O. Bryngdahl, *Computer generated holograms of three dimensional objects composed of line segments.* Journal of the Optical Society of America A, 1986. **3**(5): p. 726-730.

14. Muffoletto, R.P., J.M. Tyler, and J.E. Tohline, *Shifted Fresnel diffraction for computational holography.* Optics Express, 2007. **15**(9): p. 5631-5640.
15. Morucci, S., P. Noirard, and J.C. Grossetie, *Improvements of Fresnel computer-generated holograms.* Optics Communications, 1997. **134**: p. 25-30.
16. Frere, C. and D. Leseberg, *Large objects reconstructed from computer generated holograms.* Applied Optics, 1989. **28**(12): p. 2422-2425.
17. Leseberg, D., *Sizable Fresnel-type hologram generated by computer.* Journal of the Optical Society of America A, 1989. **16**(2): p. 229-233.
18. Wyrowski, F. and O. Bryngdahl, *Iterative Fourier-transform algorithm applied to computer holography.* Journal of the Optical Society of America A, 1988. **5**(7): p. 1058-1065.
19. Gerchberg, R.W. and W.O. Saxton, *A practical algorithm for the determination of the phase from image and diffraction plane pictures.* Optik, 1972. **35**: p. 237-246.
20. Walsh, J., *Creating 3D Computer Generated Holograms Using MATLAB*, in *Applied Physics*. 2003, RMIT University: Melbourne. p. 58.
21. Jordan Jr, J.A., et al., *Kinoform Lenses.* Applied Optics, 1970. **9**(8): p. 1883-1887.
22. Brown, B.R. and A.W. Lohmann, *Computer-generated Binary Holograms.* Optical Science and Technology, 1969. **13**(2).
23. Matsushima, K. and M. Takai, *Recurrence formulas for fast creation of synthetic three-dimensional holograms.* Applied Optics, 2000. **39**(35): p. 6587-6594.
24. Haist, T., M. Schonleber, and H.J. Tiziani, *Computer-generated holograms from 3D-objects written on twisted-nematic liquid crystal displays.* Optics Communications, 1997. **140**: p. 299-308.
25. Gao, F., et al., *Electron-beam lithography to improve quality of computer-generated hologram.* Microelectronic Engineering, 2002(61-62): p. 363-369.
26. Bryngdahl, O. and F. Wyrowski, *Digital holography/Computer generated holograms.*, in *Progress in Optics*, E.Wolf, Editor. 1990: Amsterdam.
27. Lee, W.H., *Computer Generated Holograms*, in *Progress in Optics*, E. Wolf, Editor. 1978: Amsterdam. p. 121-232.
28. Tricoles, G., *Computer generated holograms: an historical review.* Applied Optics, 1987. **26**(20): p. 4351-4360.

29. *New Directions in Holography and Speckle*, ed. H.J. Caulfield and C.S. Vikram. 2008, Los Angeles: American Scientific Publishers.
30. Ashkin, A., *Acceleration and trapping of particles by radiation pressure.* Physical Review Letters, 1970. **26**(4): p. 156-159.
31. Ashkin, A. and J.M. Dziedic, *Optical levitation by Radiation Pressure* Applied Physics Letters, 1971. **19**(8): p. 283-285.
32. Ashkin, A. and J.M. Dziedic, *Optical leviation of liquid drops by radiation pressure.* Science (Wash. DC), 1975(187): p. 1073-1075.
33. Roosen, G. and C. Imbert, *Optical levitation by means of 2 horizontal laser beams-theoretical and experimental study.* Physics Letters A., 1976. **59**: p. 6-8.
34. Ashkin, A., *Trapping of atoms by resonance radiation pressure.* Physics Review A, 1978. **40**: p. 729-732.
35. Gordon, J.P. and A. Ashkin, *Motion of atoms in a radiation trap.* Physics Review A, 1980. **21**: p. 1606-1617.
36. Chu, S., et al., *Three-Dimensional viscous confinement and cooling of atoms by resonance radiation pressure.* Physical Review Letters, 1985. **55**(1): p. 48-51.
37. Chu, S., et al., *Experimental observation of optically trapped atoms.* Physical Review Letters, 1986. **57**(3): p. 314-317.
38. Ashkin, A., J.M. Dziedic, and J.E. Bjorkholm, *Observations of a single beam gradient force optical trap for dielectric particles.* Optics Letters, 1986. **11**: p. 288-290.
39. Chu, S., *The manipulation of neutral particles*, in *Nobel Lectures, Physics 1996-2000*, G. Eskspong, Editor. 2002, World Scientific Publishing: Sinapore.
40. Ashkin, A., *Optical trapping and manipulation of neutral particles using lasers.* Proceedings of the National Academy of Sciences, 1997. **94**: p. 4853-4860.
41. Ashkin, A., *Forces of a single-beam gradient laser trap on a dieletric sphere in the ray optics regime.* Biophysical Journal, 1992. **61**: p. 569-582.
42. *The Single-Beam Gradient Force Optical Trap UCSD Modern Physics Lab.* [cited 02/11/2008]; Available from: http://www-physics.ucsd.edu/neurophysics/courses/physics_173_273/optical_trap_guide.pdf.
43. Kawauchi, H., et al., *Calculation of optical trapping forces on a dielectric sphere in the ray optics regime produced by a radially polarised laser beam.* Optics Letters, 2007. **32**(13): p. 1839-1841.

44. Mao, F.L.X., Q.R., K. Wang, and L.Y. Lang, *Calculation of axial optical forces exerted on medium sized particles by optical trap.* Optics & Laser Technology, 2005. **39**: p. 34-39.
45. Neuman, K.C. and S.M. Block, *Optical trapping.* Review of Scientific Instruments, 2004. **75**(9): p. 2786-2809.
46. Bartlett, P. and S. Henderson, *Three-dimensional force calibration of a single-beam optical gradient.* Journal of Physics - Condensed Matter, 2002. **14**(33): p. 7757-7768.
47. Stilgoe, A.B., et al., *The effect of Mie resonances on trapping in optical tweezers.* Optics Express, 2008. **16**(19): p. 15039-15051.
48. Sun, B. and D.G. Grier, *Comment: The effect of Mie resonances on trapping in optical tweezers.* Optics Express, 2009. **17**: p. 2658-2660.
49. Grier, D.G., *Optical tweezers in colloid and interface science.* Current Opinion in Colloid & Interface Science, 1997. **2**: p. 264-270.
50. Zhang, J., et al., *Optical trapping carbon nanotubes.* Colloids and Surfaces A: Physicochem. Eng. Aspects 2006. **284-285**: p. 369-372.
51. Bechinger, C., *Colloidal suspensions in confined geometries.* Current Opinion in Colloid & Interface Science, 2002(7): p. 204-209.
52. Helseth, L.E., *Mesoscopic orbitals in strongly focused light.* Optics Communications, 2003. **224**: p. 255-261.
53. Fallman, E., et al., *Optical tweezers based force measurement system for quantitating binding interactions: system design and application for the study of bacterial adhesion.* Biosensors and Bioelectronics, 2004. **19**: p. 1429-1437.
54. Zhou, M., et al., *Manipulation on human red blood cells with femtosecond optical tweezers.* Chinese Optics Letters, 2008. **6**(12): p. 919-921.
55. Guillion, M., K. Dholakia, and D. McGloin, *Optical trapping and spectral analysis of aerosols with a supercontinum laser source.* Optics Express, 2008. **16**(11): p. 7655-7664.
56. Henderson, S., S. Mitchell, and P. Bartlett, *Propagation of hydrodynamic interactions in colloidal suspensions.* Physical Review Letters, 2002. **88**(8). Article number 088302.
57. Henderson, S., S. Mitchell, and P. Bartlett, *Direct measurements of colloidal friction coefficients.* Physical Review E, 2001. **64**(6). Article number 061403.

58. Li, M. and J. Arlt, *Trapping multiple particles in single optical tweezers.* Optics Communications, 2008. **281**: p. 135-140.

59. Dharmadhikari, J.A., et al., *Multiple optical traps with a single laser beam using a simple and inexpensive mechanical element.* Current Science, 2007. **93**(19): p. 1265-1270.

60. Sun, Y.Y., et al., *Simultaneous optical trapping of microparticles in multiple planes by a modified self-imaging effect on a chip.* Applied Physics Letters, 2007. **91**. Article number 051101.

61. He, H., N.R. Heckenberg, and H. Rubinsztein-Dunlop, *Optical particle trapping with higher-order doughnut beams produced using high efficiency computer generated holograms.* Journal of Modern Optics, 1995. **42**(1): p. 217-223.

62. Dufresne, E.R. and D.G. Grier, *Optical tweezer arrays and optical substrates created with diffractive optical elements.* Review of Scientific Instruments, 1998. **69**: p. 1974-1977.

63. Dufresne, E.R., et al., *Computer generated holographic optical tweezer arrays.* Review of Scientific Instruments, 2001. **72**: p. 1810-1816.

64. Korda, P.T., G.C. Spalding, and D. Grier, *Evolution of a colloidal critcial state in an optical pinning potential landscape.* Physical Review B, 2002(66). Article number 024504.

65. Prentice, P.A., et al., *Manipulation and filtration of low index particles with holographic Laguerre-Gaussian optical trap arrays.* Optics Express, 2004. **12**(4): p. 593-600.

66. Polin, M., et al., *Optimised holographic optical traps.* Optics Express, 2005. **13**: p. 5831-5845.

67. Liesener, J., et al., *Multi-function optical tweezers using computer-generated holograms.* Optics Communications, 2000. **185**: p. 77-82.

68. Curtis, J.E., B.A. Koss, and D.G. Grier, *Dynamic holographic optical tweezers.* Optics Communications, 2002(207): p. 169-175.

69. Hossack, W.J., E. Theofanidou, and J. Crain, *High-speed holographic optical tweezers using a ferroelectric liquid crystal microdisplay.* Optics Express, 2003. **11**(17): p. 2053-2059.

70. Leach, J., et al., *3D manipulation of particles into crystal structures using holographic optical tweezers.* Optics Express, 2004. **12**(1): p. 220-226.

71. Eriksen, R.L., et al., *Computer controlled orientation of multiple optically trapped particles.* Microelectronic Engineering, 2003(67-68): p. 872-878.

72. Sinclair, G., et al., *Interactive application in holographic optical tweezers of a multi-plane Gerchberg-Saxton algorithm for three-dimensional light shaping.* Optics Express, 2004. **12**(8): p. 1665-1670.

73. Sinclair, G., et al., *Assembly of 3-dimensional structures using programmable holographic optical tweezers.* Optics Express, 2004. **12**(22): p. 5475-5480.

74. Chapin, S.C., V. Germain, and E.R. Dufresne, *Automated trapping, assembly and sorting with holographic optical tweezers.* Optics Express, 2006. **14**(26): p. 13095-13100.

75. Jesacher, A., et al., *Holographic optical tweezeers for object manipulations at an air-liquid surface.* Optics Express, 2006. **14**(13): p. 6342-6352.

76. Roichmann, Y., I. Cholis, and D.G. Grier, *Volumetric imaging of holographic optical traps.* Optics Express, 2006. **14**: p. 10907-10912.

77. Roichmann, Y., V. Wong, and D.G. Grier, *Colloidal transport through optical tweezer arrays.* Physical Review B, 2007. **75**. Article number 011407.

78. Lee, S. and D.G. Grier, *Holographic microscopy of holographically trapped three-dimensional structures.* Optics Express, 2007. **15**: p. 1505-1512.

79. Ferri, L.C., *Visualisation of 3D information with digital holography using laser printers.* Computers & Graphics, 2001. **25**: p. 309-321.

80. Hennessy, L., *Optical Trapping of Colloidal Particles Using Computer Generated Holography*, in *Applied Physics Final Year Project Report*. 2008, RMIT: Melbourne. p. 24.

81. Marks, S., *Optical Trapping*, in *Applied Physics Final Year Project Report*. 2007, RMIT university: Melbourne. p. 14.

82. Filosa, J., *Single beam optical trap*, in *Applied Physics Final Year Project Report*. 2007, RMIT University: Melbourne. p. 15.

83. Roichmann, Y., et al., *Performance of optical traps with geometric aberrations.* Applied Optics, 2005. **45**: p. 3425-3429.

Bibliography

Barret, H.H & Myers, K.J. “Foundations of Image Science.” John Wiley & sons, Hoboken, New Jersey, 2004

Brigham, E. “The Fast Fourier Transform.” Prentice-Hall Inc, 1974.

McGlynn, P “Computer Generated Holograms.” PH 306 report, RMIT, 2002.

Poon, T.-C., “Optical Scanning Holography with MATLAB.”: Springer Science+Business Media, New York, 2007.

Schnars, U. and W. Jueptner, “Digital Holography.” Springer-Verlag, Heidelberg, 2005.

Wilksch, P.A “Holography- Lecture notes.” PHYS 1173 lecture notes, RMIT, 2002.

.

Wilksch, P.A “Lasers – Lecture notes.” PH988 Lecture notes, RMIT, 2000.

Wilksch, P.A “Fields, Waves & Light- Vol. 2: Light.” PH 257 lecture notes, RMIT, 2000.